

---

# Transient source detection and performance studies of eROSITA

---

Masterarbeit aus der Physik

Vorgelegt von  
Tobias Hain  
1. Februar 2017

Dr.-Karl-Remeis-Sternwarte Bamberg & ECAP  
Friedrich-Alexander-Universität Erlangen-Nürnberg



Betreuer: Prof. Dr. Jörn Wilms



# Abstract

In this thesis, the feasibility of a source detection for transient sources in the data collected by *eROSITA* during its four year survey phase is investigated. The main focus is set on the development of an economical algorithm which only needs the measured detector count rate and is therefore fast enough to act as trigger for follow up observations of transient sources.

In order to simulate an all-sky survey with transient sources, a source catalog of Gamma-Ray Burst (GRB) afterglows was created. The source distribution and population is chosen to reflect GRB statistics measured by *BATSE* and *Swift*. I used *Swift* lightcurves to model the time variable behavior of the afterglows. To create a realistic observation, the RASS catalog is included to model diffusive X-ray background as well as bright foreground sources. I used the simulator *SIXTE* to obtain data from several half year all-sky surveys including both source catalogs.

I present a detection algorithm based on a bayesian block analysis of the lightcurve data. The bayesian block algorithm finds change points in the event data, these are points at which the countrate changes significantly. Those change points can be associated with sources entering and leaving the FOV. Two methods to filter transient from persistent sources are presented, both require a reference catalog of known sources. The first method is based on discarding all photons from known sources, the second method models the expected lightcurve and looks for deviations from the measured data caused by transient sources. The position of the sources is found by using the sky projected photon coordinates or the attitude of the telescope.

I tested the detection algorithm on the data from the simulated all-sky surveys. As employed the algorithm is sensitive to fluxes above  $3 \times 10^{-12} \text{ erg cm}^{-2} \text{ s}^{-1}$  in 0.5–10 keV. Above the threshold the detection works reliably without omitting transients sources due to spurious filtering. A GRB afterglow detection rate of 2 afterglows per year was determined.

Simulations were used to investigate the pile up and bright source performance of *eROSITA*. A critical pile up limit of 1% is reached at source fluxes of 5 mCrab for on axis slew observations. Scientifically relevant data gathered in a single slew (50 counts or more) for on axis observations can be expected at a source flux higher than 0.1 mCrab.



# Zusammenfassung

In dieser Arbeit wurde die Realisierbarkeit eines Quelldetektionsalgorithmus für transiente Quellen in der vierjährigen Durchmusterungsphase von *eROSITA* untersucht. Der Hauptteil war hierbei die Entwicklung eines performanten Algorithmus, der lediglich die Detektorzählrate zur Quelldetektion benötigt und schnell genug ist, um follow-up Beobachtungen von transienten Quellen auszulösen.

Ein Gamma-Ray Bursts (GRB) afterglow Quellkatalog wurde erstellt, der die von *BATSE* und *Swift* gemessene Verteilung und Population von echten GRBs möglichst originalgetreu reproduziert. Die zeitlich variable Helligkeit der afterglows wurden mit Hilfe von *Swift* Lichtkurven modelliert. Um eine möglichst realistische Beobachtung zu modellieren wurde der RASS Quellkatalog der *ROSAT* Mission verwendet um weitere helle, konstante Quellen sowie einen diffusen Hintergrund in die Simulation einzufügen. Schließlich wurde der Simulator *SIXTE* verwendet, um mehrere Beobachtungen des kompletten, durch die beiden Quellkataloge modellierten, Himmels zu simulieren.

Ich stelle einen Quelldetektionsalgorithmus vor, der im wesentlichen mit dem bayesischen Blöcke Algorithmus arbeitet. Dieser analysiert die Detektorlichtkurve, indem er nach Wechsellpunkten sucht. Das sind Punkte, an welchen sich die Detektorzählrate wesentlich ändert. Diese Punkte können dann mit Quellen identifiziert werden, die das Gesichtsfeld des Teleskops betreten und verlassen. Die transienten Quellen müssen von den permanenten, hellen Quellen des RASS Katalogs unterschieden werden können, hierfür stelle ich zwei verschiedene Methoden vor. Beide benötigen einen Referenzkatalog, der alle bekannten Quelle enthält, in diesem Fall ist dies der RASS Katalog. Die erste Methode funktioniert, indem alle Photonen, die von bekannten Quellen abgestrahlt wurden im Detektionsprozess weggelassen werden. Die zweite Methode berechnet aus dem Referenzkatalog eine zu erwartende Lichtkurve der Beobachtung. Diese wird dann mit der tatsächlich beobachteten Lichtkurve verglichen um von transienten Quellen verursachte Abweichungen zu finden.

Diesen Detektionsalgorithmus habe ich anhand der simulierten Daten der Himmelsdurchmusterung getestet. Ich habe eine Grenzhelligkeit von  $3 \times 10^{-12} \text{ erg cm}^{-2} \text{ s}^{-1}$  im Energieband von 0.5–10 keV berechnet. Quellen, die dunkler als diese Grenzhelligkeit sind können von dem vorgestellten Algorithmus nicht detektiert werden. Der Algorithmus funktioniert zuverlässig und filtert alle transienten Quellen aus den bekannten RASS Quellen heraus, ohne fälschlicherweise eine transiente Quelle zu verwerfen.

Schließlich habe ich das pile up Verhalten von *eROSITA* untersucht. Hierfür habe ich Beobachtungen verschieden heller Quellen für verschiedene Entfernungen von der optischen Achse simuliert. Ein Anteil von 1% Events mit pile up zu allen gültigen Events wird als kritisch betrachtet. Diesen Wert erreichen Quellen ab einer Helligkeit von 5 mCrab. Statistisch verlässliche Daten, das heißt mindestens 50 gemessene Photonen in einer Quellüberstreifung, können ab einer Quellhelligkeit von mindestens 0.1 mCrab erwartet werden.



# Contents

<b>Abstract</b>	<b>i</b>
<b>Zusammenfassung</b>	<b>iii</b>
<b>Contents</b>	<b>v</b>
<b>List of Figures</b>	<b>vii</b>
<b>List of Tables</b>	<b>ix</b>
<b>Acronyms</b>	<b>xi</b>
<b>1 Introduction</b>	<b>1</b>
1.1 Gamma-ray bursts . . . . .	2
1.1.1 History of $\gamma$ -ray burst astronomy . . . . .	2
1.1.2 The fireball model of GRBs . . . . .	3
<b>2 eROSITA on SRG</b>	<b>5</b>
2.0.1 The Instrument . . . . .	5
2.0.2 Observation strategy . . . . .	6
<b>3 Simulations</b>	<b>9</b>
3.1 SIXTE . . . . .	9
3.1.1 SIMPUT . . . . .	10
3.1.2 Instrument calibration data . . . . .	10
3.1.3 The simulation pipeline . . . . .	15
3.2 Transient source catalog with GRB afterglows . . . . .	20
3.2.1 The <i>Swift</i> Mission . . . . .	22
3.2.2 Source Modeling . . . . .	23
3.2.3 Modeling the X-ray background: RASS catalog . . . . .	27
3.3 All-sky surveys and simulation runs . . . . .	30
<b>4 Pile up</b>	<b>33</b>
4.1 Simulation setup . . . . .	33
4.2 Pile Up fraction . . . . .	34
4.3 Count rates . . . . .	36
4.4 Conclusion . . . . .	38
4.5 Conclusion . . . . .	38

<b>5</b>	<b>Source Detection</b>	<b>41</b>
5.1	Bayesian block analysis . . . . .	43
5.1.1	The piecewise constant model . . . . .	43
5.1.2	Finding the optimal segmentation . . . . .	44
5.1.3	Sensitivity of the algorithm . . . . .	45
5.2	Source detection and lower detection limit . . . . .	46
5.2.1	Basic source detection principle . . . . .	47
5.2.2	Filter sources from background radiation . . . . .	49
5.2.3	Background analysis . . . . .	50
5.2.4	Detection Limit . . . . .	54
5.3	Detection of transient sources in all-sky survey . . . . .	56
5.3.1	Transients only . . . . .	56
5.3.2	Transient sources with RASS catalog . . . . .	61
5.3.3	Source filtering . . . . .	63
5.3.4	Results and GRB detection rate . . . . .	71
<b>6</b>	<b>Conclusion and Outlook</b>	<b>75</b>

# List of Figures

1.1	Swift lightcurve of prompt GRB emission and X-ray afterglow . . . . .	3
2.1	Schematic view of <i>eROSITA</i> . . . . .	6
2.2	Position of $L_2$ Lagrange point . . . . .	7
2.3	Exposure map of <i>eROSITA</i> 's all-sky survey . . . . .	8
2.4	Schematic view of <i>eROSITA</i> 's survey strategy . . . . .	8
3.1	Sketch of Wolter-I optics . . . . .	11
3.2	PSF of <i>eROSITA</i> . . . . .	12
3.3	ARF of <i>eROSITA</i> . . . . .	13
3.4	Vignetting function of <i>eROSITA</i> . . . . .	14
3.5	Schematic view of SIXTE's simulation pipeline . . . . .	15
3.6	Theoretic impact positions of photons on the detector . . . . .	18
3.7	Valid multiple pixel patterns . . . . .	20
3.8	Sky projected source images . . . . .	21
3.9	The <i>Swift</i> spacecraft . . . . .	22
3.10	Exemplary lightcurves of GRB afterglows . . . . .	23
3.11	Processed afterglow lightcurves . . . . .	24
3.12	Flux distribution of GRB afterglows . . . . .	25
3.13	GRB temporal distribution . . . . .	26
3.14	Simple absorbed power law spectrum . . . . .	27
3.15	Sky projection of GRB positions . . . . .	28
3.16	Source and Flux distribution of RASS sources . . . . .	29
3.17	Rass source distribution . . . . .	29
4.1	Pile up effects on observations . . . . .	34
4.2	Exposure time as a function of off-axis angle in survey mode. . . . .	34
4.3	Pile up fractions in pointed and survey observations. . . . .	35
4.4	Counts detected in one slew as a function of off-axis angle . . . . .	36
4.5	Counts detected during one slew for sources with 1% and 2% pile up fraction. . .	37
4.6	Single telescope count rates as a function of off axis angle and flux. . . . .	37
4.7	Count rate contributions of valid and piled up events for pointed observations . .	38
4.8	Critical fluxes as a function of the off axis angle for 1% and 2% pile up fraction .	38
4.9	Counts at critical fluxes for survey (left) and pointed (right) observations . . . .	39
5.1	Example of piecewise constant model . . . . .	43
5.2	Bayesian block sensitivity . . . . .	46
5.3	Exemplary bayesian Block analysis . . . . .	47
5.4	Bayesian block background analysis . . . . .	51
5.5	Lightcurve background analysis . . . . .	52

5.6	LogN-logS plot all-sky survey simulations . . . . .	54
5.7	Detection probability as function as flux . . . . .	55
5.8	A source with a flux of $8.92 \times 10^{-13}$ erg cm <sup>-2</sup> s <sup>-1</sup> in 0.5–10 keV. It is too faint to be detected by the bayesian block algorithm, however, a cluster of bright pixels is visible. Image based detection algorithm may detect this source. . . . .	56
5.9	Exemplary lightcurves of all-sky survey . . . . .	57
5.10	Sky image of all-sky survey . . . . .	57
5.11	Length distribution of bayesian Blocks . . . . .	58
5.12	Vignetting effects on bayesian blocks . . . . .	59
5.13	Sky image of all-sky survey . . . . .	62
5.14	Exemplary lightcurves of all-survey . . . . .	62
5.15	Point source images . . . . .	65
5.16	Radial distribution function of survey PSF . . . . .	66
5.17	Spurious source filtering . . . . .	67
5.18	Source radius through survey PSF . . . . .	67
5.19	Correct source filtering . . . . .	68
5.20	Lightcurve source templates . . . . .	70
5.21	Template fit to simulated data . . . . .	70
5.22	Template fit and subtraction to all-sky lightcurves . . . . .	72

# List of Tables

- 2.1 Mirror resolution of *eROSITA* . . . . . 6
- 2.2 Energy resolution of *eROSITA* . . . . . 7
- 2.3 *eROSITA* technical specifications . . . . . 7
  
- 5.1 Expected background count rates . . . . . 53
- 5.2 GRB afterglow detection rate . . . . . 72



# Acronyms

**GRB** Gamma-Ray Burst

**FOV** Field Of View

**HEW** Half Energy Width

**PSF** Point Spread Function

**RMF** Redistribution Matrix File

**XML** Extensible Markup Language

**FITS** Flexible Image Transport System

**ARF** Ancillary Response File

**ULX** Ultra Luminous X-ray source

**TDE** Tidal Disruption Event



# Chapter 1

## Introduction

Evidences of humans observing the night sky can be dated back to 2000 BC. in the Near East, making astronomy the oldest recorded natural science. Since then many civilizations, like the Greeks and Babylonians, pursued the study of planets and stars (Percy, 2007). Perhaps this long tradition is a reason why astronomy had a great impact on society and every day live, e.g., think of the heliocentric versus geocentric model or celestial navigation, just to mention a few.

In the course of time the instruments and techniques to observe the sky improved, making more detailed observations and deeper insights possible. Beside the classical optical astronomy, new branches of astronomy developed, like radio and X-ray astronomy.

Compared to the optical observations, X-ray astronomy is a young field. Since the earth atmosphere absorbs X-rays, balloons or rockets are needed to perform observations of astronomical sources in the X-ray band. The first extra galactic X-ray source was found by Giacconi et al. (1962) by launching a rocket with Geiger counters to a maximum height of 225 km. Since then the instruments of course improved significantly. An important step was surely the ROSAT mission (Trümper, 1985, 1990) which performed the first all-sky survey in the soft X-ray band (0.5–2 keV). It discovered over 18000 bright sources, collected in the ROSAT Bright Source Catalog (Voges et al., 1999). Successor missions were planned, however failed or were abandoned due to technical difficulties. Since 2007, however, *eROSITA*, a X-ray observatory, is under development and construction and at the time ready for the final integration as a successor of *ROSAT*. Main part of the mission will be a four year all-sky survey, creating a more detailed catalog than *ROSAT* did. *eROSITA* will orbit the sun at the  $L_2$  Lagrange point, rotating about the axis pointing towards the sun. The telescope will therefore scan great circles which due to the orbit around the sun will rotate on the sky. It takes therefore half a year to scan the entire sky once. During the 4 year survey phase, the entire sky will therefore be scanned eight times.

To scan one great circle, *eROSITA* will take four hours, one rotation of the great circle plane takes one year. Therefore two consecutive great circles have a significant overlap. A single point in the sky is therefore scanned up to six times with the periodicity of 4 *h*.

As a result this survey strategy allows for the observation of short scaled time variabilities  $\sim 4 h$  as well as long scaled features  $\sim 0.5 - 4 y$  of sources, making *eROSITA* a great observatory to investigate transient source phenomena and detecting new transient sources (Merloni et al., 2012).

This thesis will concentrate on discussing *eROSITA*'s performance of discovering new transient sources during the survey phase. Since I used GRB afterglows as an exemplary transient source throughout this work, I will give a brief introduction on GRBs and their afterglows.

## 1.1 Gamma-ray bursts

At the moment, Gamma-ray bursts (GRB) are the brightest events known, making them an interesting phenomenon to study. GRBs are short, but very intense flashes of  $\gamma$ -rays, lasting between  $\sim 1$ – $100$  s. During the flash, they emit a total energy of  $10^{53}\Omega/4\pi$  erg, where  $\Omega$  is the solid angle, in which the energy is emitted. Due to their transient nature a clear identification of this phenomenon was difficult. Only with new observatories, it was possible to begin to understand this phenomenon.

Due to their immense luminosity, GRBs are observable at very high red shifts up to  $\sim 20$ . Therefore they are an important probe of galaxy evolution in the early universe. The afterglow of such bursts therefore can yield information about the ISM in evolving galaxies.

Since their origin is associated with massive star formation, the studying of GRBs could yield information of the final stage of massive stars and is also an important part of future multi-messenger observations including gravitational waves.

### 1.1.1 History of $\gamma$ -ray burst astronomy

The first detections of Gamma Ray Bursts (GRB) are reported by Klebesadel et al. (1973). American surveillance satellites, checking for recently banned nuclear weapons tests, detected bursts of  $\gamma$ -radiation lasting between 0.1 s to 100 s. Following this prompt emission is an afterglow emission in the X-ray and optical band.

The determined position of these bursts was very imprecise (up to  $2\pi$  sterad), an identification of a source object therefore was not possible. First models suggested accretion phenomena on neutron stars, based on the brightness and measured absorption lines (Schneider, 2006; Longair, 2011).

Further progress in the field was possible with the the BATSE (Burst and Transient Source Experiment) experiment in 1990 (Fishman et al., 1985). This observatory was specifically designed to detect GRBs and did this quite successfully. With over 2700 detected GRBs first general properties of this phenomenon could be established (Longair, 2011):

- Their positions are uniformly distributed over the sky
- The bursts can be split into two groups: long burst, with durations  $> 2$  s and short bursts  $< 2$  s

The uniform distribution proved the neutron star model wrong, since these are not distributed uniformly but concentrated towards the galactic disc (Schneider, 2006). This distribution meant that GRBs has to be of extra galactic origin, therefore high red shifts are expected.

Theoretical considerations believed that due to the high energy output in the  $\gamma$ -band, there has to be a relativistic shock causing the radiation. In this shock electrons are accelerated, emitting synchrotron radiation in the X-ray, optical, infrared and radio wavebands Longair (2011).

The first X-ray afterglow of an GRB was detected by in 1997 with BeppoSAX (Piro, 1997) by Costa et al. (1997). The X-ray afterglow were measured within 8 hours of the initial burst. The more precise positioning enabled follow-up observations in other wavelengths, which enabled the first distance measurements and a association of the GRB with a faint galaxy.

The further understanding of GRBs rose significantly with the SWIFT mission launched in 2005 (Gehrels et al., 2004), which was able to perform follow up observations of the afterglow in the X-ray and UV band.

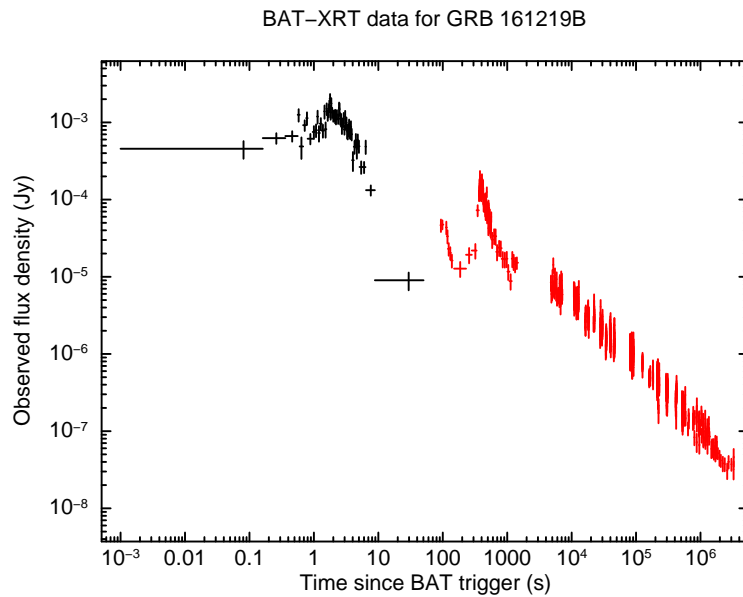


Figure 1.1: A lightcurve of an GRB and its afterglow detected by *Swift*. Black data points is the prompt emission, consisting of high energy  $\gamma$ -rays, red points is the afterglow in the X-ray regime.

### 1.1.2 The fireball model of GRBs

All presented information in this section is taken from Gehrels et al. (2009) if not indicated otherwise.

The measured optical thin, non-thermal spectra expanding to energies over the pair-production threshold at 1 MeV hint to a relativistic expanding shock in which the radiation is emitted (Gehrels et al., 2009).

This spectral shape leads to the standard model explaining the origin of GRBs, the fireball model (Meszaros et al., 1993; Mészáros, 1995; Cavallo & Rees, 1978). This model comprises a 'fireball' consisting of photons and ionized plasma which is fed by a central engine. This active region is expanding relativistically. The observed power-law radiation spectrum of  $\gamma$ -rays is emitted by synchrotron radiation of electrons in turbulent magnetic fields behind the shock. While expanding, the velocity of the expansion of this fireball decreases, softening the spectrum of the emitted radiation to X-rays and lower wavelengths, explaining the afterglow (Gehrels et al., 2009). According to this model, observing the afterglow can yield direct information about the processes of the GRB.

*Swift* lightcurves of the prompt  $\gamma$ -ray and X-ray afterglow emission show a smooth fading of the radiation from the prompt emission to the afterglow, as seen in Fig. 1.1. Margutti et al. (2013) showed that all X-ray afterglow lightcurves can be described by broken power laws and found that afterglows of short GRBs decay faster.

The difference between short and long GRBs is stressed by the fact that the origin of short GRBs is found in regions with low star formation, while long GRBs are located in regions with high star formation. The exact progenitors of GRBs remain unknown, however accretion processes onto black holes or neutron stars are promising (Gehrels et al., 2009).



## Chapter 2

# eROSITA on SRG

*eROSITA* (extended ROentgen Survey with an Imaging Telescope Array) is a German X-ray telescope (Predehl et al., 2006, 2007, 2010; Predehl et al., 2016), developed and built by the Max-Planck Institute for extraterrestrial Physics (MPE) as a successor to the failed ABRIXAS (Predehl, 1999) and canceled ROSITA mission (Predehl et al., 2003). It is scheduled to be launched on board the Russian *Spektrum-Roentgen-Gamma* satellite (Pavlinsky et al., 2008) in march 2018 and will travel to the  $L_2$  Lagrange point at an orbit around the sun. Its main task will be to perform a four year all-sky survey in the energy band between 0.5–10 keV (Merloni et al., 2012). While it is more than 20–30 times more sensitive in the soft X-ray band (0.5–2 keV) than its predecessor *ROSAT*, *eROSITA* will perform the first all-sky survey in the hard X-ray band (2–10 keV). After the survey, at least 3.5 y of pointed observations are planned.

The main goal of the survey phase is to detect a large sample ( $\sim 10^5$ ) of galaxy clusters with red shifts up to  $z = 1.3$ . These clusters are used as probes of the large scale structure of the universe, providing information about the formation and development of the latter. With this information, different cosmological theories can be tested, including dark energy, and new constraints on the cosmological constant can be derived. The investigation of dark energy is a central scientific driver of the mission (Merloni et al., 2012; Predehl et al., 2010).

Further scientific aims are to find new constraints on cosmological parameters with 1–2 orders of magnitude better statistics, but also investigating transient sources and time variable phenomenons.

### 2.0.1 The Instrument

*eROSITA*'s core components are seven individual, co aligned telescopes. Each telescope consists of a baffle, a Wolter-I mirror module (Wolter, 1952a) and a CCD camera in the focal plane of the optics. Beside providing a seven fold redundancy, utilizing seven smaller telescopes yields a lower background and pile up rate than a single, large telescope would.

The mirror design is described in Friedrich et al. (2008, 2012) and Burwitz et al. (2014). Each mirror consists of a baffle to shield the detector from stray-light photons and 54 concentric mirror shells made of gold-coated Nickel with an outer diameter of 358 mm. The focal length of each telescope is 1.6 m. The resolution of the optics is the ability to image a point source to a point in the focal plane. Since all optics are not ideal, photons are scattered around the ideal impact position. The Half Energy Width (HEW) is the radius of a circle around the ideal image, which contains half of the detected counts of the points source. The angular resolution of the single mirror modules FM1–7 is listed in Tab. 2.1.

*eROSITA* employs a pn-CCD chip as camera (Meidinger et al., 2007, 2009, 2011, 2013), which is an improved version of the camera utilized successfully on *XMM-Newton*. The energy resolution of *eROSITA*'s CCD can be found in Tab. 2.2. Each camera has a frame store area,

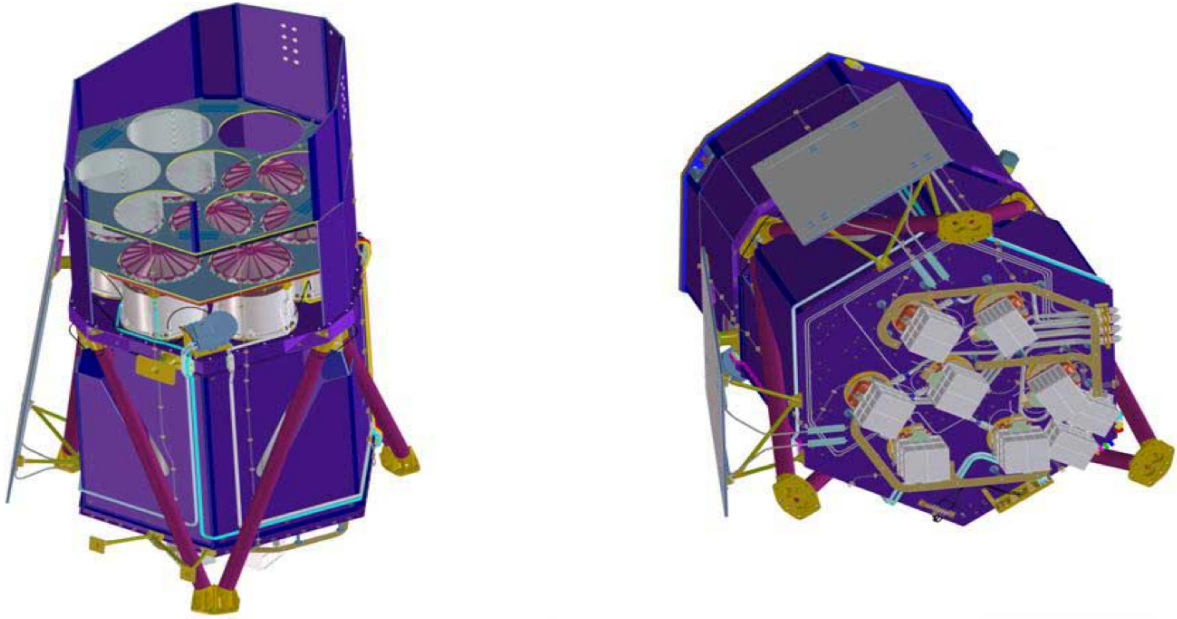


Figure 2.1: The *eROSITA* X-ray telescope. The seven individual, co aligned telescopes and cameras are visible. Taken from (Merloni et al., 2012)

Table 2.1: The resolution of the optics [arcsec] on *eROSITA*. Provided by Predehl (2016)

	FM1	FM2	FM3	FM4	FM5	FM6	FM7
HEW AL-K $\alpha$ 1.49 keV	17.0	16.0	15.5	15.9	16.5	16.1	15.6
HEW Cu-K $\alpha$ 8.04 keV	14.7	14.5	15.1	16.3	15.6	15.1	16.2

which is heavily shielded against radiation. After the frame length of 50 ms, all collected charges in the chip are moved in the frame store area, where they are read out without being contaminated by further photons. Each pn-CCD chip consists of  $384 \times 384$  quadratic pixels, each pixel with a size of  $75 \times 75 \mu\text{m}^2$ , which equals approximately 9.7 arcsec. The total area of the chip is therefore  $28.8 \text{ mm} \times 28.8 \text{ mm}$ . Combined with the optics, the resulting Field of View (FOV) has an diameter of  $1.02^\circ$ .

All technical specifications are shown in Tab. 2.3.

## 2.0.2 Observation strategy

*eROSITA*'s main task is to perform a four year long all-sky survey. The satellite will be positioned at the  $L_2$  Lagrange point, where the gravitational forces of the earth and sun are balanced by the centrifugal force, see Fig. 2.2. *eROSITA* will therefore orbit around the sun in one year. An advantage of orbiting at  $L_2$  compared to an earth orbit is that periodical heating and cooling caused by passing the earth shadow is avoided. Furthermore, the earth does not disturb the survey by passing the FOV, therefore a continuous scanning of the sky is possible.

To scan the entire sky, *eROSITA* will rotate around the axis pointing towards the sun in about 4 h, scanning a great circle of the sky with the width of the FOV. Due to the motion of the satellite around the sun in one year, the plane containing the next great circle will be rotated by

Table 2.2: The energy resolution of the pn-CCD camera [eV] on *eROSITA*. Provided by Predehl (2016)

	FM1	FM2	FM3	FM4	FM5	FM6	FM7
C-L $\alpha$ 0.277 keV	49	58	58	58	50	59	58
O-K $\alpha$ 0.525 keV	56	65	64	64	57	69	66
Cu-L 0.93 keV	68	74	70	70	68	71	72
Al-K $\alpha$ 1.49 keV	77	82	77	77	75	77	72
Ti-K $\alpha$ 4.51 keV	117	125	118	118	116	120	122
Fe-K $\alpha$ 6.40 keV	136	145	138	138	135	141	142
Cu-K $\alpha$ 8.04 keV	156	167	158	158	155	159	163
Ge-K $\alpha$ 0.90 keV	175	204	178	173	170	180	182

Table 2.3: *eROSITA* technical specifications

<b>Optics</b>	
Nested mirror shells per telescope	54
Outer mirror diameter	358 mm
Resolution	16''(on axis) to $\sim 28''$ (survey) at 1 keV
Focal length	1600 mm
FOV diameter	1.02°
<b>Detector</b>	
Detector Type	frame store pn-CCD
Number of pixels	384 $\times$ 384
Pixel size	75 $\mu\text{m}$ $\times$ 75 $\mu\text{m}$
Detector size	28.8 mm $\times$ 28.8 mm
Energy range	0.5–10 keV
frame duration	50 ms

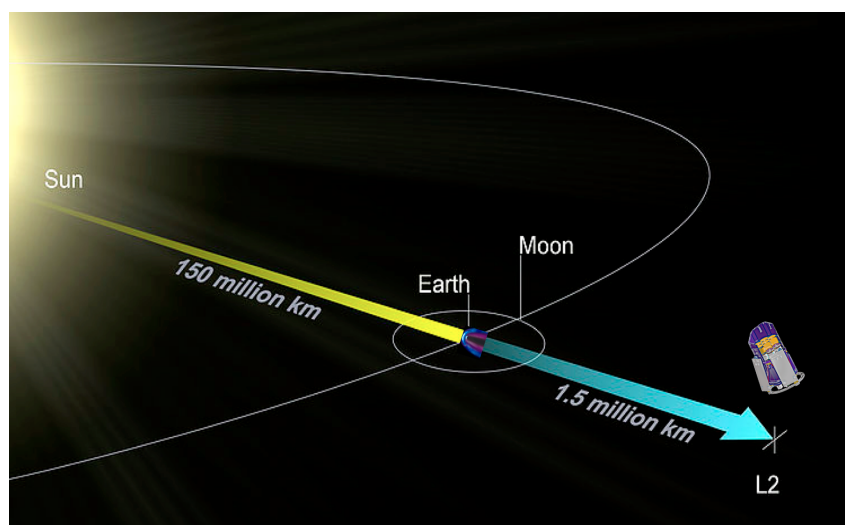


Figure 2.2: Schematic view of the  $L_2$  Lagrange point. The Lagrange points are places, where the gravitational forces of the sun and earth are balanced by the centrifugal force.

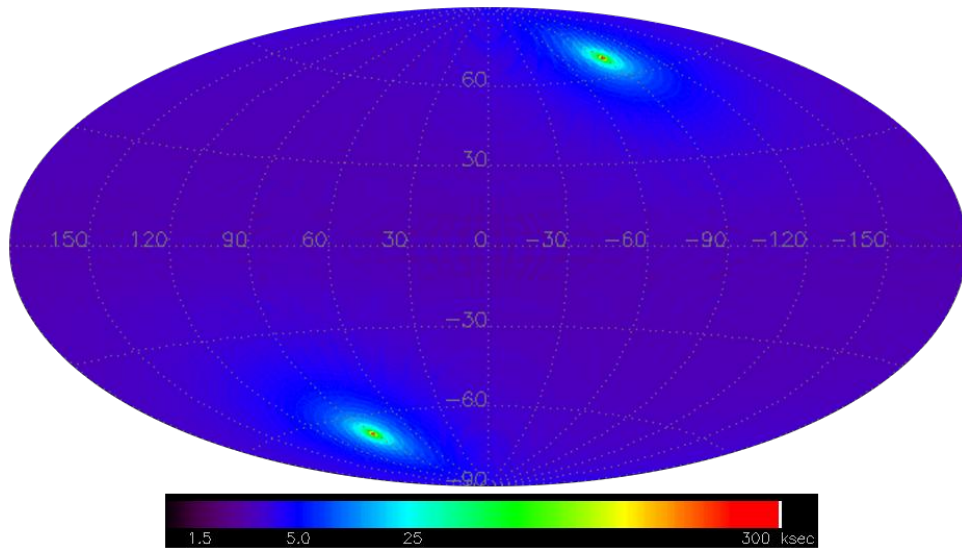


Figure 2.3: Exposure map of a simulated half year all-sky survey of *eROSITA*. The brightness of the pixels indicate the amount of exposure time. The bright spots are the ecliptic poles of the survey. Adapted from <http://www.mpe.mpg.de/455799/instrument>

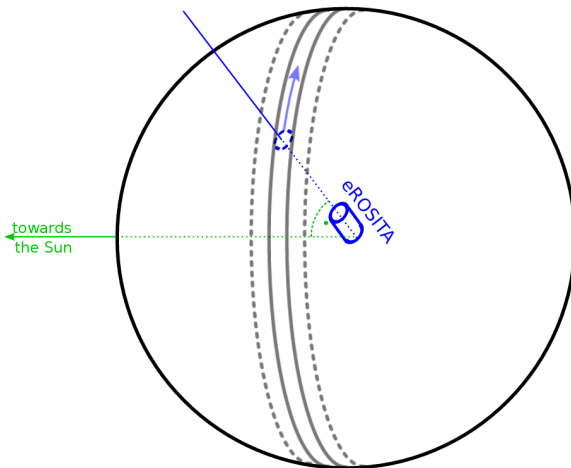


Figure 2.4: *eROSITA*'S survey strategy. By rotating around the axis towards the sun, the telescope scans great circles of the sky. Due to the orbit around the sun, the plane described by the great circle rotates. As a result the entire sky will be scanned once in half a year. Taken from Schmid (2012)

about  $0.164^\circ$ , see Fig. 2.4. Two following scans of great circles therefore have approximately  $\frac{5}{6}$  overlap. As a result, a source will appear in at least six consecutive scans of great circles per full all-sky survey (6 months). Since the ecliptic poles are scanned in every rotation, they receive much more exposure time than the rest of the sky.

With this survey strategy, the entire sky is scanned in half a year. The four year survey phase will therefore yield eight scans of the entire sky, resulting in an average exposure time of 2548 s (Merloni et al., 2012).

Since each point is scanned six consecutive times with a temporal distance of 4 h once per half-year survey, *eROSITA* survey strategy provides the capabilities to monitor time variable phenomenons and transients sources during the survey phase.

## Chapter 3

# Simulations

### 3.1 SIXTE

Simulation of X-ray Telescopes (**SIXTE**) is a software package for performing Monte Carlo simulations of X-ray observations (Schmid, 2012). Further information can be found in the **SIXTE** manual<sup>1</sup>. It provides a framework to model each step of the observation process by modifying the properties of incoming photons according to the influences of each component of the instrument, like the optics, the detector or the readout electronics. The main effort of this software is to provide realistic and accurate data while taking a reasonable amount of time to calculate. A half year survey observation of the entire sky comprising more than  $10^5$  sources takes only a few hours to perform. Furthermore, a strong focus was set on a generic instrument description, therefore minimizing the effort which is needed to simulate different instruments.

Instead of modeling each physical process in detail, e.g., by employing ray-tracing techniques for the mirrors or solid-state simulations for the detector, **SIXTE** makes use of pre-calculated models of the instruments modules. A randomizing point-spread function (PSF) is used to simulate the the optics instead of calculating each reflection of a photon. While all solid-state processes like the conversion of the photon into charges is stored in the so called Redistribution Matrix File (RMF, George et al. (2007)), the readout of the chip is modeled in detail. This approach enables **SIXTE** to simulate important features like pile up in a very realistic way.

The calibration data needed for the models can be obtained by either measurement or simulations. While reducing the needed resources, this approach also provides the desired flexibility, since all relevant information about the behavior of the instrument are coded in these models and can be exchanged easily. Human readable XML (Extensible Markup Language <sup>2</sup>) files are used to define an instrument. These XML files hold all information which define the behavior of the instrument, e.g., which RMF and PSF will be used, the size of the FOV or information about the readout process.

The concept of **SIXTE** is based on a Monte Carlo approach of randomly generating single photons emitted by sources which are then processed by a pipeline of different tools, each representing a task or a component of the instrument. The single steps of this pipeline are shown in Fig. 3.5 and essentially comprise photon generation, photon imaging through the optics and photon detection. The final output of **SIXTE** is an event list of all detected photons with their basic properties like origin, energy and arrival time. Since *eROSITA* consists of seven telescope modules, **SIXTE** will create a dedicated event file for each telescope.

The source description is provided in form of a **SIMPUT** file, a standardized format for source descriptions as simulation input (Schmid et al., 2013). In this section the most important

---

<sup>1</sup>[http://www.sternwarte.uni-erlangen.de/research/sixte/data/simulator\\_manual\\_v1.1.pdf](http://www.sternwarte.uni-erlangen.de/research/sixte/data/simulator_manual_v1.1.pdf)

<sup>2</sup><https://www.w3.org/TR/REC-xml/>

instrument calibration data, the simulation pipeline and the `SIMPUT` file format will be described.

### 3.1.1 SIMPUT

`Simulation inPUT (SIMPUT)` (Schmid et al., 2013) is a file format specification based on the `FITS` standard (Hanisch et al., 2001; Pence et al., 2010). It is designed to describe X-ray sources for simulations so it can be used easily by different software packages. Each `SIMPUT`-file can contain one or more sources. It consists of its main extension, the source catalog called `src.main`. This is a table containing the parameters, which describe the source. The physically most important are

`RA,DEC` the coordinates of the source in the sky, given in the equatorial coordinate system

`FLUX` the total flux emitted by the source in the specified energy band

`Emin, Emax` gives the boundaries of the energy band the given flux is emitted

`SPECTRUM` gives a link to the spectrum of the source.

`TIMING` gives a link to a lightcurve, if the flux varies with time

`IMAGE` gives a link to an image, if the source is extended

A spectrum has to be provided for each source. The spectrum can be given either as a photon list or as the flux density on a fine energy grid. The normalization of the spectrum is irrelevant since it is scaled to match the `FLUX` value given in the catalog.

The timing extension is optional but necessary if time variable sources are to be modeled. The extension contains a set of pairs with time and relative flux values, which describe the brightness of the source over time. The flux is interpolated between the given times. The total flux of the source is given by multiplying the reference flux value in the main catalog with the flux given in the lightcurve.

The `IMAGE` parameter has to be provided only if an extended source is described. The parameter is a link to an extension of an image in the `FITS` format. In the simulation it is handled as a probability distribution from which position the photons are emitted. Since throughout this thesis only point sources are modeled, I will not go into further detail.

More detailed information about the `SIMPUT` file format can be found on the web<sup>3</sup>, in the format definition document<sup>4</sup> and the `SIXTE` simulator manual<sup>5</sup>.

### 3.1.2 Instrument calibration data

In `SIXTE` each instrument is modeled by a set of precalculated data which describe the physical behavior of the components. Therefore the physical processes do not have to be simulated every time for each simulation and therefore saves computational time. Each data set describing one component is stored in a single file. A change of instruments is easily done by just exchanging the data files. The files can be obtained by either running detailed simulations or by measuring data of existing components. In this section I will list and present the data files used by `SIXTE`.

<sup>3</sup><http://www.sternwarte.uni-erlangen.de/research/sixte/simput.php>

<sup>4</sup><http://hea-www.harvard.edu/heasarc/formats/simput-1.1.0.pdf>

<sup>5</sup>[http://www.sternwarte.uni-erlangen.de/research/sixte/data/simulator\\_manual\\_v1.1.pdf](http://www.sternwarte.uni-erlangen.de/research/sixte/data/simulator_manual_v1.1.pdf)

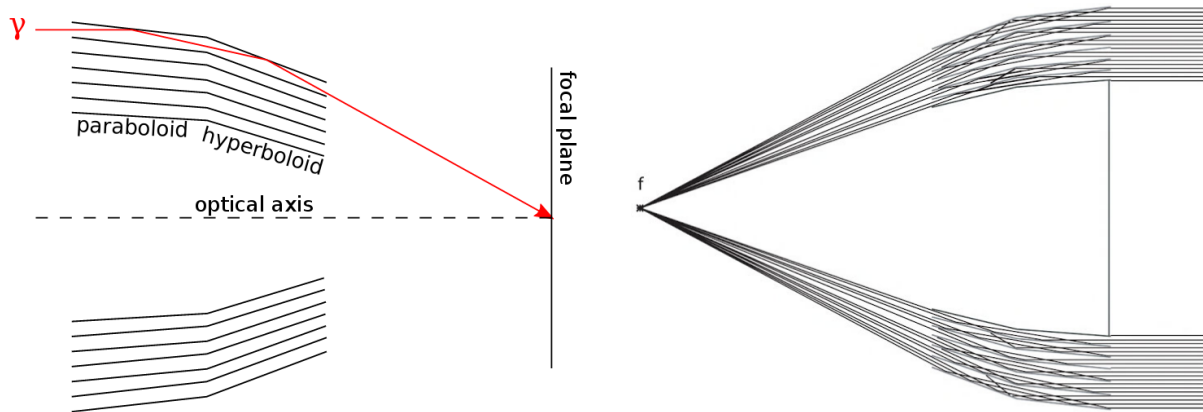


Figure 3.1: *Left*: A schematic representation of Wolter X-ray optics. X-ray optics makes use of grazing incident reflection to focus X-rays. For a shorter focal length and better imaging properties two co aligned mirrors are used. *Right*: Many mirror shells are nested into each other to maximize the effective area

## PSF

The point spread function (PSF) characterizes the optics of the telescope. For a better understanding of this concept I will give a brief overview of the employed optics on *eROSITA*, the Wolter optics.

**Wolter optics** The traditional way of focusing optical rays using reflection at mirrors at high incident angles can not be employed for X-rays, since the index of refraction is close to unity for most materials at these energies. However, X-rays are reflected at very low incident angles, called grazing incident reflection (Aschenbach, 1985; Trümper & Hasinger, 2008). Wolter (1952a) therefore proposed using areas of parabolic mirrors far away from the focal point as mirrors. Although this setting would image every point on the axis correctly, all objects observed off axis would get blurred to a circle.

Abbe's sine condition states, that only mirrors with a spherical principal surface can image an object on axis and close to the axis correctly. A parabolic mirror fulfills this condition only close to its focal point, however, this area can not be used due to the high incident angle. To fix this problem, Wolter (1952a) suggested to add a second, hyperbolic mirror, which focal point coincides with the one of the parabolic mirror. A sketch of this setting is shown in Fig. 3.1 in the left panel. Wolter showed that this mirror configuration fulfills Abbe's condition approximately.

An important advantage of this configuration is that mirror shells can be nested into each other, see right panel in Fig. 3.1. Since only small areas of the mirrors provide an incident angle low enough, the area of a single shell is very small. By nesting several shells into each other, the mirror area can be increased significantly (Trümper & Hasinger, 2008).

Since the presented configuration only approximately fulfills Abbe's condition, objects observed off axis get blurred due to coma effects. This effect is proportional to the distance of the axis, which means, object observed far away from the optical axis are more blurred (Wolter, 1952a). Although an improved mirror geometry was presented by Wolter (1952b), a substantial improvement of the image quality could not be achieved.

**PSF** As mentioned, an ideal telescope optic would image a point source, observed on and off axis, as a point on the focal plane, where the detector is placed. As seen, however, real optics do not show this behavior. The ideal image of a point is smeared to an extended image. The

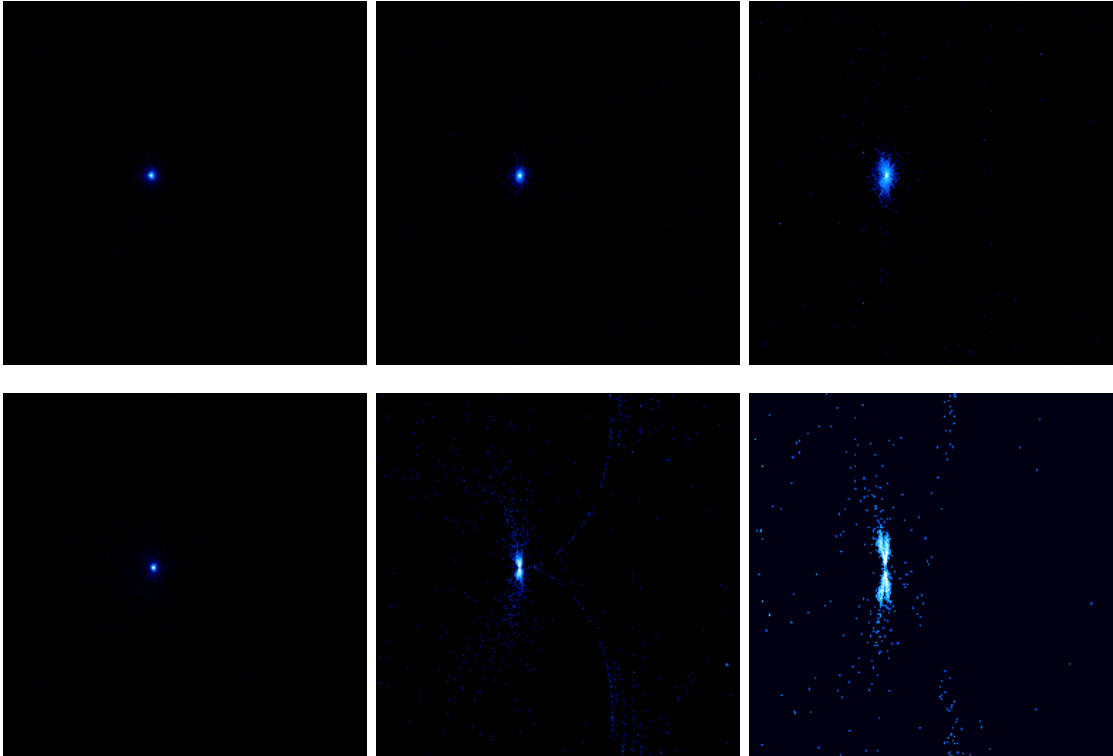


Figure 3.2: Point spread functions for two different energies (top: 0.3 keV, bottom: 8 keV) and different off axis angles, small to large from left to right, as used in this thesis (`erosita_psf_v3.1.fits`). It becomes smeared with increasing energy and off axis angle due to aberration effects of the X-ray optics. The PSF gives is the resulting image of a point source imaged by the optics.

Point Spread Function (PSF) describes this behavior of the optics quantitatively. It is defined as the response function of the optics to a point source. Graphically speaking, the point spread function is the picture which is seen, if a point source is observed with the given optics. The PSF can be obtained by either doing exact ray-tracing simulations or by direct measurement. The PSF mainly is dependent on the off axis angle and the energy of the incident photons. It is provided as an image, which is interpreted as probability density distribution, therefore gives the probability for each pixel that an incident photon will be reflected to (Schmid, 2012).

The main reason to use the randomization approach is to save save computational time since no extensive ray-tracing simulations are needed. However, with an accurately measured PSF, no accuracy is lost.

Figure 3.2 shows example PSFs from *eROSITA* (`erosita_psf_v3.1.fits`) for different energies and off axis angles. As can be seen, the area of the PSF gets not only larger with increasing energy and off axis angles but asymmetric due to the aberration effects described above.

## ARF

The effective area of the optics of a telescope is of course a very important characteristic, since it codes the telescopes ability to collect photons. The effective area of the optics is obtained by multiplying the projected area of the mirror shells as seen from the front with their reflectivity (Schmid, 2012).

The sensitivity of X-ray detectors of measuring photons depends on the energy of the arriving photons. These originate from the energy dependence of the optics and the detector, as well as

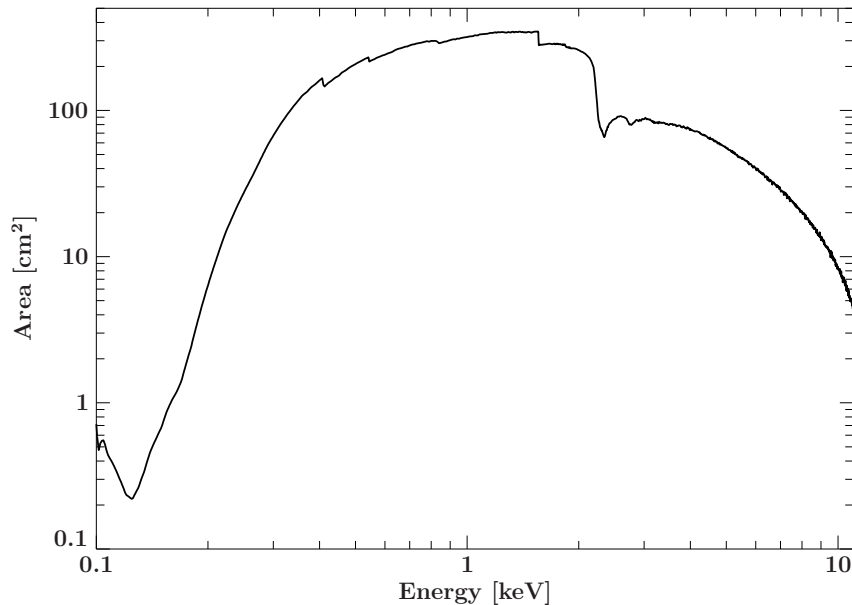


Figure 3.3: The ARF of *eROSITA* as used in this thesis for one mirror module for on axis observations as provided in the file `rosita_iv_1telonaxis_ff.arf`. The ARF describes the efficiency of the instrument in dependence of the energy and is often specified as an effective area.

its quantum efficiency (George et al., 2007). A photon with a very high energy is more likely to pass through the detector without interacting with it, therefore the photon is not measured. This energy dependence is taken into account with an energy dependent effective area. A larger area of course can collect more photons. If a detector is especially sensitive to a specific photon energy for example, its effective area for this energy is high.

The Ancillary Response File (ARF) contains the effective area of the instrument, therefore information about the physical area of the optics combined with energy dependent effects of other components.

The ARF used in this thesis (`erosita_iv_1telonaxis_ff.arf`) is shown in Fig. 3.3. The effective area peaks around 1.5 keV and decreases rapidly with higher or lower energies.

## RMF

A CCD detector, as will be used on *eROSITA*, basically works as followed: a photon hits the detector and creates electrons via the photoelectric effect and secondary interactions. These electrons carry charge, which is stored in the detector until the exposure time passed. Afterwards the charge is read out. The amount of charge is then converted to a pulse height which is assigned to a certain channel in the readout electronics. The amount of charge depends on the energy of the incident photon. Therefore the assigned channel contains the information of the energy of the detected event (Bradt, 2004). Therefore each photon with energy  $E$  should be assigned to the same channel. In real detectors, however, noise in the electronics or variabilities in the photon to charge conversion can affect the measurement. This effect depends on the detector. How the detector behaves is stored in the Redistribution Matrix File (RMF) (George et al., 2007). This file contains the detector response  $R(I, E)$ , which is the probability that a photon with energy  $E$  is assigned the channel  $I$ . To be stored in a file, this needs to be discretized to the response matrix  $R_D$ :

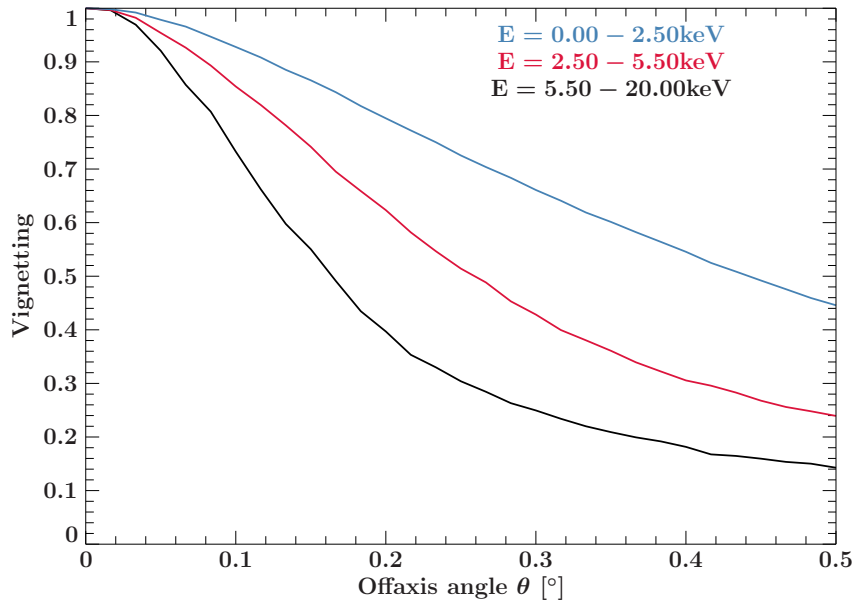


Figure 3.4: The vignetting function of *eROSITA* (`erosita_vignetting_v2.1.fits`) for three different energy bands as function of the off axis angle  $\theta$ . Vignetting functions are the probability that an arriving photon will be correctly deflected by the optics and incident on the detector. With increasing energy and off axis angle the efficiency decreases. Sources observed at high off axis angles appears darker than on axis.

$$R_D(I, J) = \frac{1}{E_j - E_{j-1}} \int_{E_{j-1}}^{E_j} R(I, E) dE \quad (3.1)$$

Using the introduced RMF and ARF, the number of counts  $C$  in a channel  $I$  after an observation can be calculated using

$$C(I) = T_{\text{exp}} \int \text{RMF}(I, E) \text{ARF}(E) P(E) dE \quad (3.2)$$

where,  $T_{\text{exp}}$  is the exposure time,  $P(E)$  the spectrum of the observed source and RMF and ARF the introduced function describing the instrument (Schmid, 2012).

### Vignetting

The vignetting function describes the relative probability for photons from off axis sources to reach the focal plane compared to on axis observations (Schmid, 2012). It depends on the energy, the azimuth angle and the off axis angle of the incident photon. Similar effects are already described in the ARF, however the latter does not contain the angular dependency. When analyzing data, the Vignetting function is already included in the ARF (George et al., 2007).

Figure 3.4 shows the vignetting function of *eROSITA* as used for the simulations in this thesis (`erosita_vignetting_v2.1.fits`), for different energy bands as function of the off axis angle. It is normalized to 1 for on axis observations. The fraction of photons being reflected decreases with the off axis angle  $\theta$ , as is typical for most telescopes with Wolter-I optics. This means sources which are observed with high off axis angles will appear darker than they actually are.

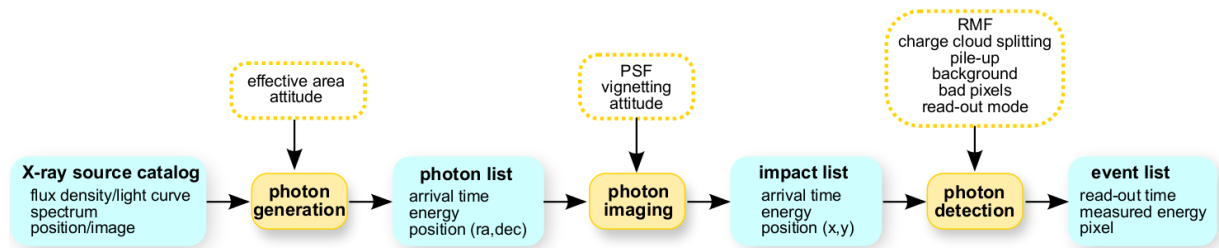


Figure 3.5: The SIXTE pipeline used to generate an event list from simple source descriptions. Graphic from Schmid (2012)

### 3.1.3 The simulation pipeline

As all models of the components have been introduced, I will now explain the single steps of the pipeline in detail, following closely Schmid (2012).

At first, a set of photons emitted by sources in the FOV of the telescope has to be created. Since only the photons hitting the optics are created, this step already has to include energy dependence effects, therefore makes use of the ARF. This set of photons has to describe the spectral and temporal features of the sources observed. After the photon creation, the imaging process is simulated, taking into account the propagation of the photons through the optics, therefore making use of the Vignetting and PSF. This step creates a list of photons, which actually hit the detector. The last step in the pipeline is the detection process, which converts the incident photons into detector signals and finally creates the event list, the output of the simulation. How these steps work in detail will be presented in this section.

#### Source selection

The first step in the pipeline is to generate a set of photons, which are emitted by the sources described in the SIMPUT catalog. This sample of photons should represent the physical properties of the sources like brightness, spectrum, and position as close as possible. Since the FOV of most telescopes cover only a small fraction of the sky, a lot of computation time can be saved by neglecting all sources which are not in the FOV. Since most detectors are shielded against radiation coming from other directions than the telescope axis it is sufficient to generate only photons which directly hit the optics of the telescope (Schmid, 2012).

As the pointing of the telescope changes during survey observations, the simulation interval is cut into smaller pieces of about 1 s. Then for each interval all sources which are in the FOV plus a margin of 20% at the given time are selected. The additional margin is needed, since new sources can enter the FOV during the interval of 1 s. As the SIMPUT catalogs can contain thousands of sources the source selection can be a costly operation, an efficient sorting algorithm is needed. SIMPUT implements the source catalog as a  $k$ -d tree (Press et al., 2007), which allows for fast sorting and searching for nearby sources.

#### Photon energy

For each generated photon, its energy is randomly drawn from the given spectral distribution of the source. SIXTE implements this using the inversion method (Gould et al., 2006). The following method of obtaining photon energies from a flux density distribution is taken from Schmid (2012).

The SIMPUT file provides the spectra of the sources as an energy flux density  $P(E_j)$  in the units of  $\text{erg cm}^{-2} \text{s}^{-1}$  evaluated on a discrete grid of energy bins  $E'_{j,\text{low}}$  to  $E'_{j,\text{high}}$ . For the inversion method a normalized, integrated energy distribution  $p'_k$  is needed.

To account for different sensitivities of the detector for photon energies, the energy flux density is multiplied by the ARF. The energy spectrum  $P(E_j)$  is then obtained by

$$p(E_j) = P(E_j) \cdot \text{ARF}(E_j) \quad (3.3)$$

where interpolation between different energy grids of the energy flux density and the ARF may be necessary. The normalized integrated energy distribution is calculated by

$$p'_k = \frac{1}{\sum_{j=0}^{N-1} p(E'_{j,\text{low}} \text{ to } E'_{j,\text{high}})} \sum_{j=0}^k p(E'_{j,\text{low}} \text{ to } E'_{j,\text{high}}) \quad (3.4)$$

This means  $p'_k$  is the fraction of the total amount of energy emitted by the source in the energy band of  $E'_0$  to  $E'_{k,\text{high}}$ . Because  $p'_l$  is normalized, only the shape but not the magnitude of the original energy flux density does influence the energy determination. In order to choose a photon energy a uniformly distributed random number  $l$  is picked from the interval  $[0, 1)$ . The corresponding energy value then is found by

$$l = \min\{k | p'_k > r\} \quad (3.5)$$

Picking all photon energies this way will create a photon sample with energies describing the source spectrum.

### Arrival Time

Aside from the shape of the spectrum, another important property of a source is its brightness. This corresponds to the number of generated photons per time interval. This number depends on the flux  $F_X$  assigned to the source in the SIMPUT file, but also the ARF and the spectrum. The photon rate  $R$  is calculated according to

$$R = \frac{F_X}{\int_{E_{\min}}^{E_{\max}} P(E) \cdot E dE} \cdot \int_0^{\infty} P(E) \cdot \text{ARF}(E) dE \quad (3.6)$$

where  $P(E)$  is the photon flux density,  $E$  the energy and  $F_X$  the total energy flux of the source in the reference energy band between  $E_{\min}$  and  $E_{\max}$ . Since the formula normalizes the spectrum, the actual magnitude of the spectrum does not affect the number of generated photons (Schmid, 2012).

Photons are emitted by the source independently that means the arrival of one photon does not influence the timing of the following photon. In this case, the total number of photons is given by the Poisson statistics

$$P_{\lambda}(N) = \frac{\lambda^N}{N!} e^{-\lambda} \quad (3.7)$$

where  $\lambda$  is the expected value of the total number of photons given by  $\lambda = R \cdot T$ . More important than the total number of photons is in our case the arrival times of the photons. Therefore the time between the single events is needed. The distribution of time intervals between two photons can be derived from the Poisson statistic by demanding that no photon is arriving in a time interval  $\Delta t$ , then one photon is arriving in the time interval  $dt$  after  $\Delta t$ . This yields an exponential distribution of times between the arrival of photons  $\Delta t$  given by

$$K(\Delta t) = 1 - e^{-R\Delta t} \quad (3.8)$$

Employing the inversion method again, the time to the next photon can be determined by

$$(\Delta T)_i = -\frac{1}{R} \ln(u_i) \quad (3.9)$$

where  $u_i$  is a uniformly distributed random number in the interval  $[0, 1)$ . Generating photons by dicing the time between the events for the entire exposure time yields the sample of photon arrival times.

This approach assume constant energy flux densities. However there are many sources of interest with time variable fluxes, like pulsars or GRB afterglows. **SIMPUT** therefore allows to provide a lightcurve  $l(t_i)$ , which provides the flux of the source for several dates. The time dependent mean photon rate  $r(t)$  is then obtained by

$$r(t_i) = R_i \cdot l(t_i) \quad (3.10)$$

Equation (3.9) then needs to be adapted to the variable photon rate. An algorithm was developed by Klein & Roberts (1984), but I will skip the details and refer to Klein & Roberts (1984).

### Origin coordinates

The last missing information to describe the photon sample completely are the coordinates, where the photons were emitted from. Although **SIXTE** provides functionality for extended sources such as nebulae, I only used point sources throughout this thesis. This makes the source coordinate assignment easy, since simply the source coordinates of the emitting source are used. With this information, the photon list is complete.

### Photon imaging

The next step in the pipeline after photon generation is the photon imaging. The imaging simulates the influence of the telescope's optics on the arriving photons. The purpose of the optics is to focus the incident photons on the detector plane. All information in this section is taken from (Schmid, 2012) is not stated otherwise.

**Vignetting** The first step in the imaging simulation process is to apply the vignetting function. Since the vignetting is provided as a probability, it can be simply applied by just picking a uniformly distributed random number in the interval  $[0, 1)$ . The photon is discarded if the random number is higher than the vignetting function, otherwise it is accepted. Photons arriving from high off axis angles therefore are discarded more likely than photons arriving on axis.

**Impact position** This step calculates the impact position of each photon. As can be seen in Fig. 3.6, in theory each photon has a fixed impact position on the focal plane on the detector, determined by the source position and the focal length  $f$  of the telescope.

Added to this impact position is an offset to account for the non ideal optics. These are provided by the PSF. To obtain the impact position, at first the ideal impact position based on the geometry seen in Fig. 3.6 is calculated. Then, the center of the PSF is set to this impact position and the offset is randomly calculated, based on the probability function provided by the PSF image. This offset added to the ideal impact position yields the final impact coordinates on the detector plane.

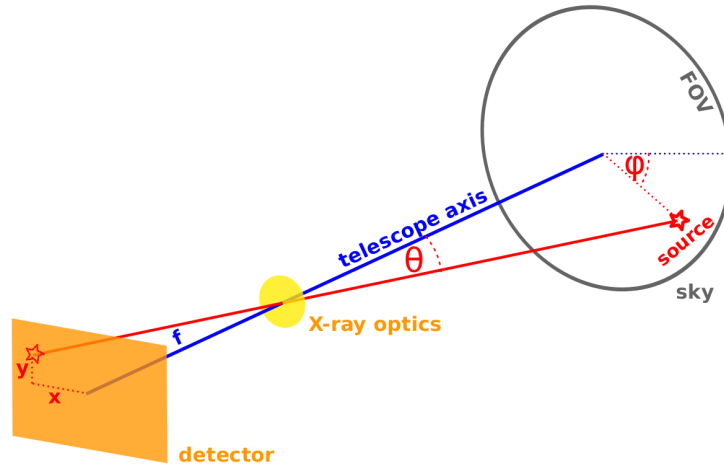


Figure 3.6: Schematic view of the imaging process of the telescope.  $\theta$  is the off axis angle,  $x, y$  are detector coordinates. Taken from (Schmid, 2012)

### Photon detection

The final step in the pipeline is the detection of the photons. There are different types of detectors, *eROSITA* employs a pn-CCD chip (Merloni et al., 2012).

A CCD (charged coupled device) is a semiconductor designed to measure radiation. It mainly consists of a silicon substrate doped with impurities to create potential wells, which can trap electrons (Bradt, 2004). CCDs are constructed as an array of pixels with each pixel containing a potential well. An incident X-ray photon will deposit its energy in the substrate via the photoelectric effect. Secondary processes then will create a number of ionization electrons from the silicon atoms. These electrons are collected in the potential wells of the pixels. The higher the primary photon energy is, the more electrons will be created. Therefore the amount of created charge is a measurement for the energy of the photon (Bradt, 2004). To create an ionization electron in silicon, an energy of 3.65 eV is needed. Therefore an incident X-ray photon with energy  $E$  creates

$$N = \frac{E}{3.65 \text{ eV}} \quad (3.11)$$

electrons (Schmid, 2012).

The created electrons are not concentrated on one point but form a charge cloud. This expands over a certain area, often on the order of  $10 \mu\text{m}$ . If a photon hits a pixel at its border, the charge cloud can spread over several pixels, therefore placing charges in multiple pixels although only one photon arrived. This behavior is determined by the charge cloud model (Schmid, 2012).

After determining the impact pixel  $(x_i, y_i)$  of the incident photon, the charge cloud is calculated and the charges distributed over the affected pixels. The general approach is to use a Gaussian charge cloud model, however, a *eROSITA* specific model is provided by K. Dennerl (priv. comm.). The amount of charge  $c^*$  in a pixel  $(k, l)$  is given by

$$c_{k,l}^* = \exp \left[ - \left( \frac{r_{k,l}}{0.355} \right)^2 \right] \quad (3.12)$$

with

$$r_{k,l} = \sqrt{\left( x_i - x_k - \frac{d_x}{2} \right)^2 + \left( y_i - y_l - \frac{d_y}{2} \right)^2} \quad (3.13)$$

$c_{k,l}^*$  needs to be normalized:

$$c_{k,l}^* = \frac{c_{k,l}^*}{\sum_{i=n}^{n+1} \sum_{j=m}^{m+1} c_{k,l}^*} \quad (3.14)$$

All equations are taken from (Schmid, 2012). For *eROSITA* the typical charge cloud size is very small compared (for a Gaussian charge cloud  $\sigma \approx 10\mu\text{m}$ ) to the size of a pixel ( $d \approx 75\mu\text{m} \times 75\mu\text{m}$ ), therefore only pixels adjacent to the impact pixel needs to be taken into account. The fractional amount of charge deposited in each pixel can be determined with the given formulas. The size of the charge cloud has to be provided in the configuration XML file. The RMF is then used to convert the signal in each pixel to the corresponding energy channel, modeling the detector noise.

One photon can therefore cause so-called single, double, triple or quadruple events, meaning that respectively one, two, three or four pixels are affected by this photon.

After the desired exposure time, the electrons collected in the wells need to be measured (Schmid, 2012): A voltage is applied to the chip that moves the potential wells containing the electron towards one direction, moving the electrons from one pixel to the next adjacent pixel step by step. At the edge of the CCD, readout electronics will measure the charges of each pixel and converts this to a pulse height. Each pulse height is then assigned a channel. Each channel number corresponds to a certain photon energy. Because the charge deposition and readout is affected by perturbations such as noise, not all photons with the same energy get assigned the same channel. The exact behavior of each detector is modeled in its RMF.

SIXTE models this detection and readout process with a generic detector model, although the implementation of specific models is possible. For *eROSITA* a rectangular array of  $384 \times 384$  pixels is employed. The readout is exactly modeled as described above (Schmid, 2012). The frame duration of *eROSITA* is 50 ms. That means every 50 ms the mentioned process is performed. During the readout process new photons can hit the detector and place charges in pixels. Since these pixels, however, contain the charge of photons with other impact positions, this can influence the measurement heavily. To eliminate this effect, a pattern recombination is performed after each readout. This effect is addressed in the next section.

For each detected photon a new event in the output file is created. It is assigned the detector coordinates of the affected pixel, the reconstructed photon energy, the time stamp at the moment of readout, the reconstructed origin coordinates in the equatorial coordinate system, how much pixels were hit and if the event was piled up.

### Pattern recombination

In this section I want to give a brief overview of the effects of charge cloud splitting and the resulting activation of several pixels by one photon. All information were taken from (Schmid, 2012). As already mentioned, one photon can deposit charges in multiple pixels, if it hits a pixel close to its border. All affected pixels together are called a pattern. For *eROSITA* the typical charge cloud size is very small compared to the size of a pixel (Schmid, 2012). Therefore a single photon can only create certain pattern shapes, which are shown in Fig. 3.7. All other patterns are considered to be caused by multiple photons and are discarded as invalid since no reliable energy determination can be achieved. The process of analyzing pattern shapes, discarding invalid ones and merging pixels from valid patterns to a single event is called pattern recombination. SIXTE performs this step after each readout of a frame.

Another important step closely related to pattern recombination is pile up. This is an effect distorting the measurement and occurs if the detector is suspected to high count rates. A detailed discussion of this phenomenon will be presented in Chapter 4.

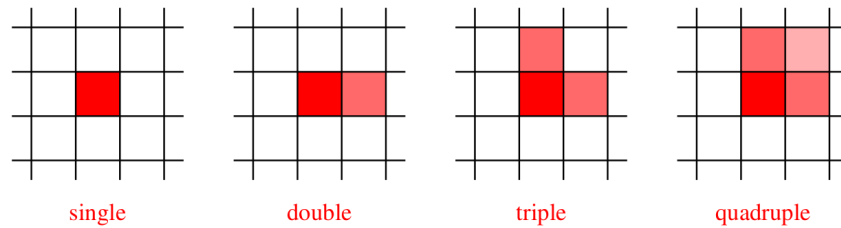


Figure 3.7: Valid patterns for *eROSITA* caused by charge cloud splitting over several pixels. The darkened pixel contains the majority of the charge. All patterns can be rotated and stay valid. Taken from (Schmid, 2012)

### Sky projection

All detected photons can be spatially resolved, since the impact position on the detector is known. For a fixed pointing of the telescope, the CCD then directly images a picture of the sky in the FOV. By inverting the calculations in Sec. 3.1.3 the origin position of the photons can be found.

In survey mode, however, the pointing of the telescope is constantly moving. This means all sources are moving through the FOV and the detector image does not show a direct picture of the sky but blurred lines of all sources (Schmid, 2012).

Figure 3.8 shows this effect. The image top left shows the image as seen by the detector. Only a blurred line is visible, since the source moves through the FOV. During the movement, all photons are projected to different pixels, leaving this line. The effect of the broadening of the PSF can be seen, as the line gets broader at the edges of the FOV.

To get an image of the actual sky, the source position of each photon needs to be calculated, taking the attitude information determining the pointing of the telescope into account (Schmid, 2012). The result of these calculations are the source coordinates of the photons in the equatorial coordinate system. As can be seen in Fig. 3.8, the blurred line converts into an image of the original point source. Since the photons are diverted from their original position by the PSF, the projected coordinate in the sky differs slightly from the source position, therefore blurring the source image.

To obtain the origin coordinates of the photons in pointed observations, the same process is performed, however no moving pointing needs to be considered.

## 3.2 Transient source catalog with GRB afterglows

The aim of this thesis is to investigate the performance of *eROSITA* at the detection of transient sources. The first step therefore is to obtain data on which basis an analysis of the performance can be made. Since I am interested in transient sources during the survey phase of *eROSITA*, I therefore performed several simulations of a half year all-sky survey of *eROSITA* comprising a catalog of transient sources. This catalog is a core feature of the simulation, since it models the sky, which *eROSITA* will observe. In this chapter I will explain how I created this source catalog and present the general simulation setup for the all-sky surveys. Furthermore, I will present the RASS catalog which I used to model bright foreground and faint background sources. These sources are included to provide a realistic observation setting.

There are several kinds of transient sources, like X-ray binaries, ultra-luminous X-ray sources (ULX), tidal disruption events (TDE) or Gamma-Ray Burst (GRB) afterglows. This study should not specialize on one type of transient sources, therefore GRB afterglows were chosen only as an example representative source type. An important reason to choose Gamma-Ray

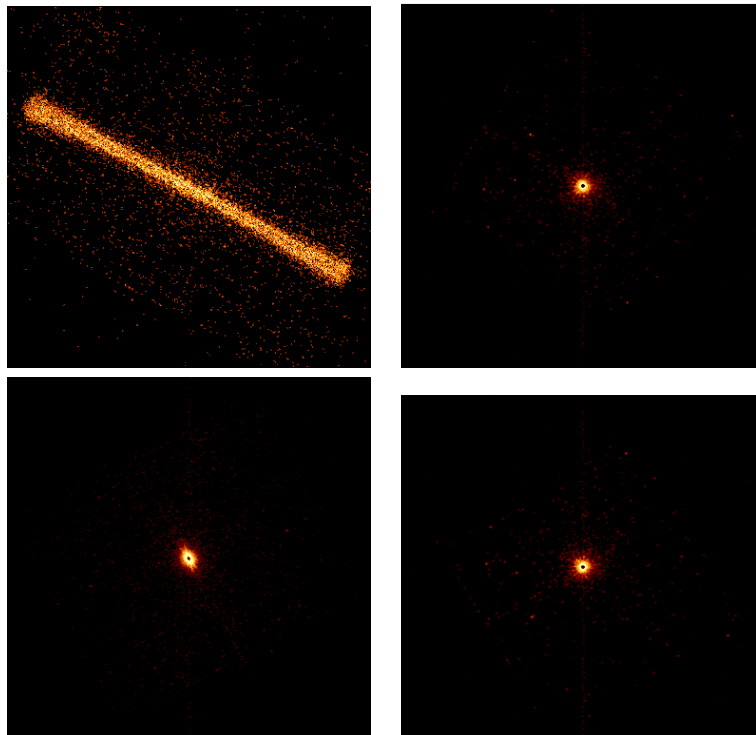


Figure 3.8: Left side shows the observation of a source in survey mode, right side for a pointed observation. Top pictures show the detector image, bottom ones the sky projected image of the FOV. Since the telescope pointing moves during survey mode the photons are detected at different positions on the detector, leaving a trace. Sky projections takes this into account and calculates back their correct origin. This problem does not affect pointed observations, here the detector images directly the sky.

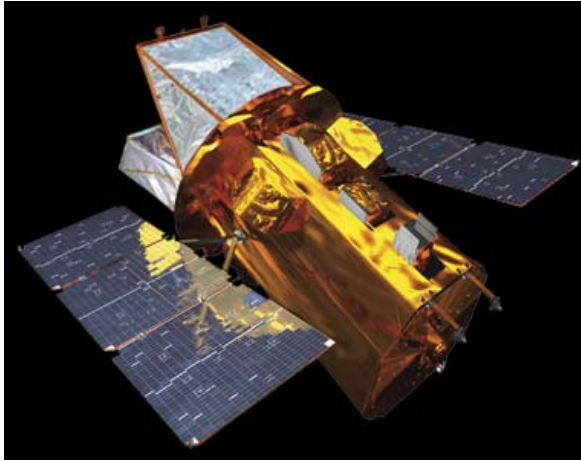


Figure 3.9: The *Swift* spacecraft. Taken from [http://space.skyrocket.de/doc\\_sdat/explorer\\_swift.htm](http://space.skyrocket.de/doc_sdat/explorer_swift.htm)

bursts is that because of the *Swift* mission good data is available.

The focus of the catalog creation is set on reproducing the properties and conditions of real GRBs as close as possible. Therefore real data is used where ever possible. As mentioned in the SIMPUT section, each source needs to be assigned a flux, a position and a spectrum. A special focus is set to modeling of the time variability, since the latter is the most important feature of a transient source.

The general process to create the transient catalog starts with the processing of the raw *Swift* lightcurves. In this step it is ensured that each lightcurve from the *Swift* sample fulfills our needs. More details are given later. To model a transient source, it is assigned a lightcurve randomly picked from the prepared *Swift* sample. This lightcurve contains information about the flux as function of time and when the GRB is triggered. To complete each source, a spectrum and a position has to be assigned. All sources are modeled to match the properties of the measured sample of GRB afterglows as close as possible to keep the simulations as realistic as possible.

Another important information for the catalog in general is the total number of sources contained. This can vary depending on the simulation time, source type and other factors. The mentioned steps are explained in detail below, at first, however, I will give a very short summary of the *Swift*-mission, since our source catalog heavily depends on data from this mission.

### 3.2.1 The *Swift* Mission

*Swift* is a multiwavelength observation satellite launched in 2004 by NASA (Gehrels et al., 2004; Wells et al., 2004; Swift Science Center, 2016). It has three instruments on board to observe  $\gamma$ -rays, X-ray and ultraviolet/optical radiation. Its primary instrument is the Burst Alert Telescope (BAT). It uses a coded-mask aperture, is sensitive in the energy band between 15 – 150 keV and its FOV covers 1.4sr, which is about  $1/9$  of the entire sky. Its purpose is to detect and locate Gamma-Ray bursts. The X-Ray Telescope (XRT) is a Wolter-I telescope sensitive between 0.2 – 10 keV and is designed to perform follow up observations of the GRB afterglow and take their lightcurves and spectra and measure their fluxes.

If BAT detects a GRB, its on board electronics locate it down to 1 – 3 arcmin within 20s. After about 10s it begins to move the pointing of the XRT instrument on to the GRB to perform follow up observations. With a peak slew speed of about  $1^\circ$  per second it takes *Swift* typically about 90s to reach the final observation position. This means that most lightcurves taken by *Swift* begin about 90s after the initial GRB. A special remark is set to the quick availability of the measured data and position of the GRB, making further follow up observations possible.

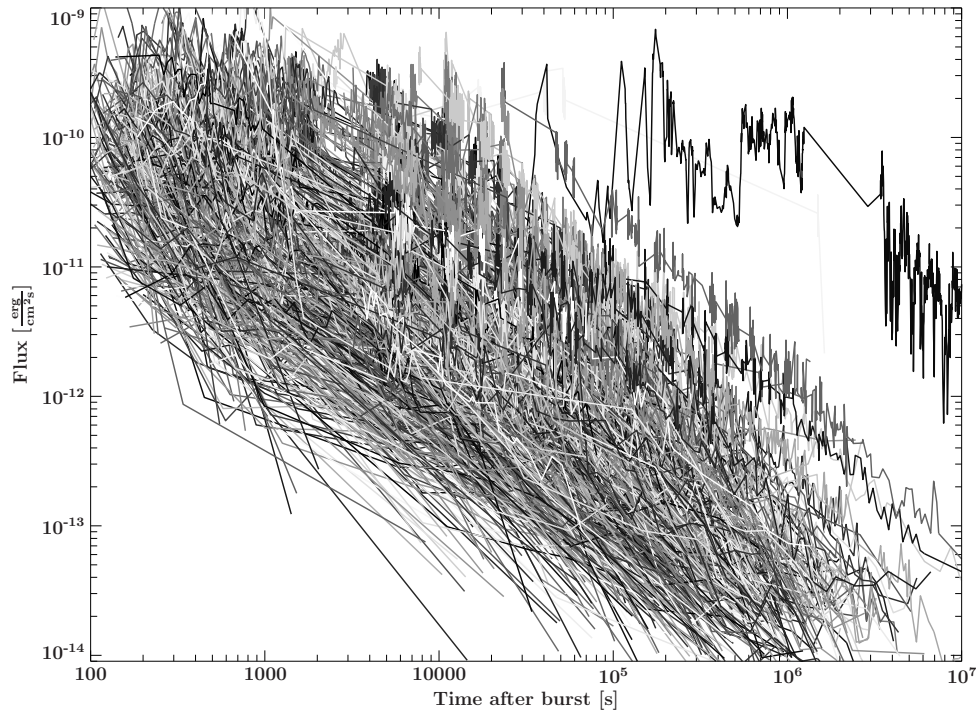


Figure 3.10: A sample of 946 lightcurves of the X-ray afterglow of GRBs taken by *Swift* until 2015 September 31 in the energy band 0.3 – 10 keV. The presented lightcurves from the *Swift* sample follow a power law with a long term index of  $\Gamma \approx -1.2$ .

All *Swift* data are publicly available on the web<sup>6</sup>.

### 3.2.2 Source Modeling

#### Timing feature

As mentioned above, each source in the SIMPUT catalog needs a spectrum, lightcurve and a position. To describe the timing feature of the GRB afterglows, I used lightcurves of GRB afterglows captured by *Swift*, following the approach of Brand et al. (2016) for simulations of *Athena* observations of GRB afterglows. These are available at the Swift Data Center<sup>7</sup>. A total sample of 946 lightcurves was used, measured in the energy band of 0.3 – 10 keV until 2015 September 31. The entire lightcurve sample is shown in Fig. 3.10. The plot shows that almost all lightcurve are described roughly by a power law. It shows an example of three lightcurve with a fitted power law in olive with good agreement. Most lightcurves cover the time interval between 100 to  $10^5$  s with their fluxes between  $5 \times 10^{-10}$  and  $1 \times 10^{-13}$  erg cm<sup>-2</sup> s<sup>-1</sup>. Margutti et al. (2013) found for the long term decay > 4 ks of the afterglows, a power index of  $\Gamma = -1.2$  applies.

However the time span of the lightcurves in the sample as well as the number of data points in each lightcurve varies. To get a more homogeneous sample, I follow the approach of Margutti et al. (2013) and only use *complete* lightcurves. That means each lightcurve needs to start at  $t \leq 90$  s and needs to last until at least  $t = 1 \cdot 10^6$  s. Lightcurves not fulfilling this standard are extrapolated to the demanded length as follows. A power law function  $F(t) = N \cdot t^{-\Gamma}$  is fitted to the data and used to add points in front of and behind the measured data until the demanded

<sup>6</sup><http://swift.gsfc.nasa.gov/sdc/>

<sup>7</sup><http://www.swift.ac.uk/index.php>

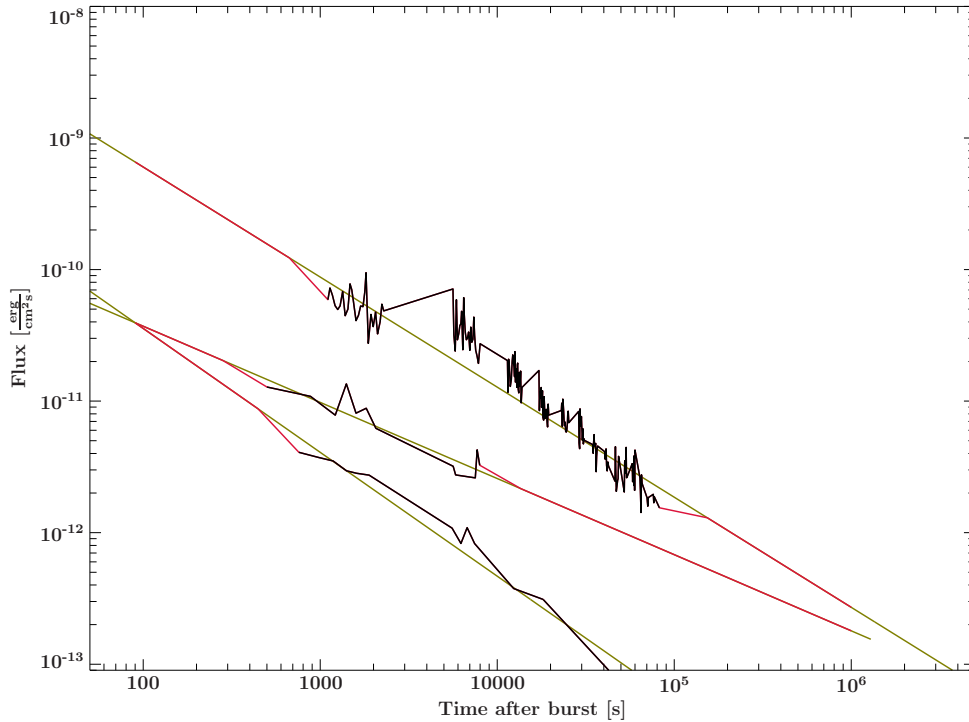


Figure 3.11: Three lightcurves picked from the sample. The black line shows the measured data by *Swift*, the red line is extrapolated data. All lightcurves are extrapolated by fitting a power law to last the time interval between 90 and  $10^6$  s. The olive line shows the fitted power law. Extrapolation is performed to create a more homogeneous sample. Fluxes can reach higher magnitudes than originally measured and drop at least below  $1 \times 10^{-12}$   $\text{erg cm}^{-2} \text{s}^{-1}$ .

length is reached. Lightcurves containing three or less data points are discarded, since they are not reliable. Figure 3.11 shows three extrapolated lightcurves. The black line are data points taken by *Swift*, the red ones are the extrapolated data.

The start time of  $t = 90$  s was chosen, since this is the earliest time the XRT instrument on board of *Swift* can take data. Due to the exponential decay most photons are emitted in the time short after the flash. Therefore cutting the first seconds of the GRB afterglow means that many photons are neglected. Therefore all lightcurves are extrapolated to the earliest point for which measured data is available. Although extrapolating closer to the GRB than 90 s would yield more photons, no *Swift* data are available to confirm the power law behavior of the lightcurves before  $t = 90$  s.

As described later in Sec. 5.2, the detection algorithm presented in this thesis is, in best conditions, sensitive for sources with fluxes above approximately  $3 \times 10^{-12}$   $\text{erg cm}^{-2} \text{s}^{-1}$ . This means, all lightcurves should last long enough to drop below this limit value. The main reason to extrapolate the data to last a certain time is that if the lightcurves stop earlier, it may happen that the source is visible in the FOV, but is already “off”. This would cause a non physical bias, reducing the detection rate. Figure 3.12 illustrates this subject. Shown is a histogram of the minimal and maximal flux of each lightcurves, therefore the flux at the start and at the end of the afterglow. The figure clearly shows that, after extrapolating, all fluxes drop at least to the required flux limit value of  $3 \times 10^{-12}$   $\text{erg cm}^{-2} \text{s}^{-1}$ .

The absolute brightness of the GRB afterglows is not a value which was artificially chosen, but is determined by the lightcurve sample, since the absolute flux values provided are directly adopted. However, the extrapolation can yield higher fluxes than originally measured by *Swift*.

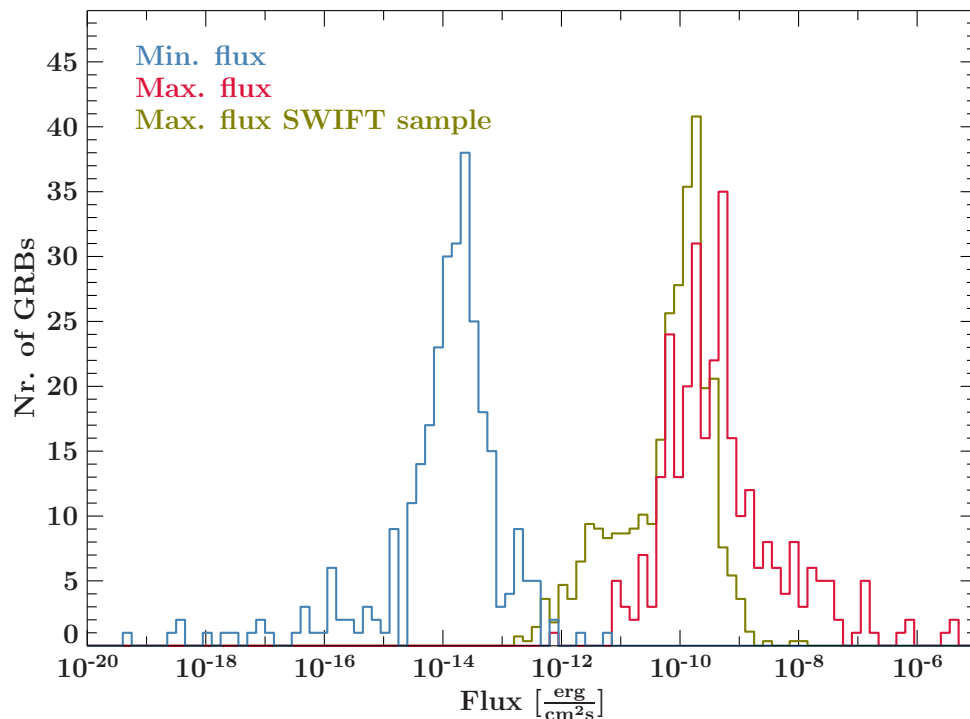


Figure 3.12: The distribution of maximum fluxes of the original *Swift* lightcurve sample in olive and after processing in red. All lightcurves are extrapolated to start at  $t = 90$  s. This can result in higher fluxes than the original data shows. This causes a bias towards higher fluxes for the processed lightcurves. However for both cases the majority of the brightness are accumulated in the peak around  $5 \times 10^{-9} \text{ erg cm}^{-2} \text{ s}^{-1}$ . The blue data shows the minimal fluxes of the lightcurves, i.e. the last brightness of the afterglow before the source is put “off”. All lightcurves drop below the visibility limit of  $1 \times 10^{-12} \text{ erg cm}^{-2} \text{ s}^{-1}$ .

Figure 3.11 shows in red the distribution of maximum fluxes of a sample of 400 processed lightcurves, the total number of sources which will be contained in the transient source catalog, more details on his number will follow. The distribution of the maximum fluxes from the original *Swift* lightcurves normalized to 400 lightcurves is shown in olive for comparison. The histogram shows that the peaks of the brightness distributions of the original and processed lightcurves match quite well and are positioned around  $5 \times 10^{-9} \text{ erg cm}^{-2} \text{ s}^{-1}$ . This means that the gross part of the lightcurve brightness are not affected by the extrapolation. However, the distribution of fluxes outside the peak for the processed sampled is shifted towards higher fluxes compared to the original sample. This results of course from the extrapolation. The entire sample contains lightcurves starting after  $t = 90$  s which means that their maximum brightness is not measured, as can be seen in Fig. 3.12. Therefore the brightness distribution is biased towards lower fluxes. By extrapolation higher fluxes are reached and the sample distribution as shown is observed.

The last step is to distribute all GRBs over the time of the all-sky survey. Since GRBs are uniformly distributed on the sky (Meegan et al., 1992; Horack, 1993) the temporal occurrences of GRBs has to be uniformly distributed, too. The presented source catalog is tailored to a half year all-sky survey, therefore the GRBs are distributed over half a year. The resulting distribution of the start times is shown in Fig. 3.13. Before these times, the flux of the lightcurve is set to zero, i.e. the source does not emit any radiation, until the start time, then the flux rises to its maximum value and then decays exponentially. After the last data point or  $t = 10^6$  s, the flux is set to zero again.

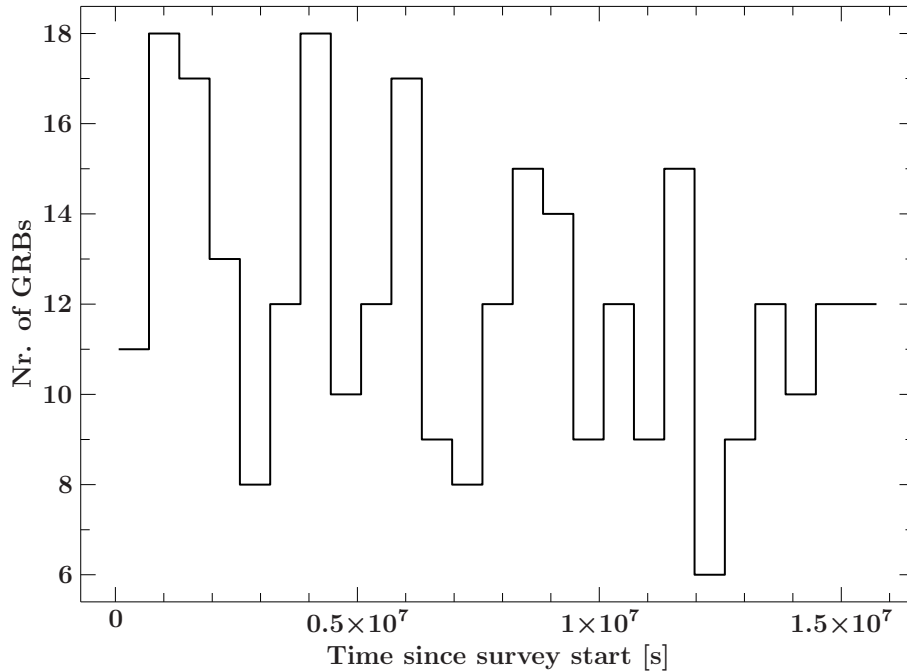


Figure 3.13: The distribution of start times  $t_0$  of the *Swift* afterglows. The start time is the time at which the brightness of the afterglows jumps from zero, meaning the source is “off”, to its maximum value. All start times are uniformly distributed over the simulation time of half a year, as can be seen in this figure.

### Spectral shape

Beside the timing features of a source, the spectrum is probably one of the most important property of a source. In this thesis, however, only the detection of the sources is studied and all presented detection algorithms are based on counting photons. Their energy is not relevant, as long it is detectable by *eROSITA*. Since *SIXTE* calculates the number of photons and therefore the emission rate of the source only with the total flux parameter, the shape of the spectrum will not change the number of detected photons, therefore the shape of the spectrum is irrelevant for our purposes. Furthermore, the number of counts accumulated in a single slew over a source is in general so low that no reliable spectral information can be determined from the data. Therefore each GRB afterglow can be assigned the same spectrum without losing accuracy of the simulation.

I chose a simple, absorbed power law for all GRBs. I used a simple absorbed power law spectrum (`"tbabs(1)*powerlaw(1)"`) with a low foreground absorption of  $N_{\text{H}} = 1 \times 10^{20} \text{ cm}^{-2}$  and a photon index of  $\Gamma = 2$  (Margutti et al., 2013). Figure 3.14 shows the used spectrum.

### Source count and positioning

The number of samples in one GRB afterglow catalog was calculated by the number of measured GRBs by *Swift*. The FOV of the BAT instrument, which discovers the GRBs first and then orders the positioning of the follow up instruments is 1.4 sr (Barthelmy, 2000). Which means it covers about 1/9 of the entire sky. At the time, *Swift* detects about 90 GRBs a year (Swift Science Center, 2016). Assuming that the GRBs are distributed uniformly over the sky, the detection rate can be extrapolated for the entire sky to 810 GRB occurring each year. Since

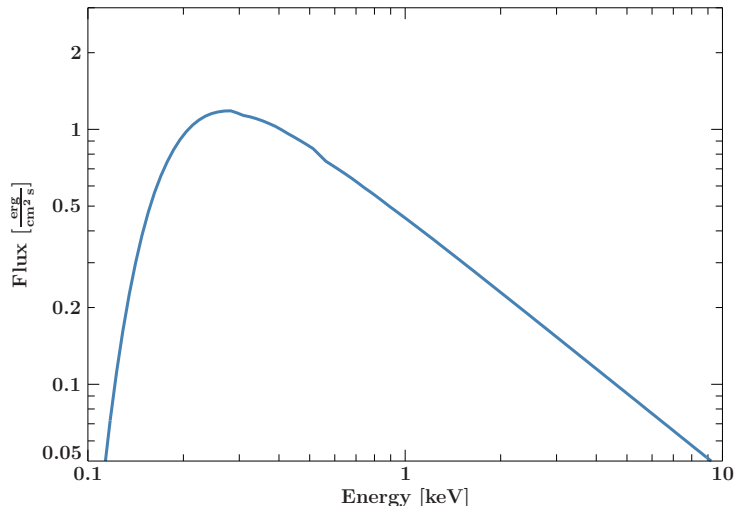


Figure 3.14: A simple absorbed power law spectrum used for all GRB afterglows. The model "tbabs(1)\*powerlaw(2)" with the parameters  $nH=10^{-2}$ ,  $\Gamma = 2$  was used.

*eROSITA* will take half a year to complete a full all-sky survey, our sample for one simulation run will contain around 400 GRB afterglows. These are picked by randomly picking sources from the pool.

The last important property to assign is the source position. The position of the GRBs are provided in the equatorial coordinate system with the right ascension  $\alpha$  and the declination  $\delta$ . As before, the distribution of the samples in the SIMPUT catalog should map the reality as close as possible. Figure 3.15 shows the distribution of 1061 GRBs detected by *Swift* since its launch. It illustrates the uniform distribution of GRBs on the sky (Horack, 1993; Meegan et al., 1992; Gehrels et al., 2009). The same distribution will be applied to the sources in the SIMPUT catalog.

The uniform distribution of source positions over the sky is achieved by drawing three uniformly distributed random numbers for the position  $(x, y, z)$  of the source in Cartesian coordinates. If this position is on the unity sphere, i.e. the length of the vector is close to 1, this position is accepted, otherwise it is discarded. If the numbers are accepted, the coordinates are transformed to spherical coordinates and converted in the equatorial coordinate system, yielding  $\alpha, \delta$ .

With increasing declination, the area of a strip with the width of  $\Delta\delta$  decrease steadily. If the values of  $\alpha, \delta$  were drawn directly as random numbers this would lead to an overpopulation of the poles, since the decreasing area is not taken into account. Therefore the mentioned, more complicated procedure is done.

The population of GRBs is with  $31.83 \frac{1}{sr} = 9.7 \cdot 10^{-3} \frac{1}{\square^\circ}$  not very dense, as can be seen in Fig. 3.15. The FOV of *eROSITA* is circular with a radius of  $0.51^\circ$ , which yields a solid angle of  $\Omega = 2.489 \cdot 10^{-4} sr$ . This means, on average, *eROSITA* has  $8 \times 10^{-3}$  GRB afterglows in its FOV, assuming they are always emitting radiation. However, the afterglows are at maximum 6% of the exposure time "on". Taking the uniform distribution over the exposure time into account, only  $4.8 \times 10^{-4}$  GRB afterglows are visible in the FOV on average. It will therefore be very unlikely that more than one GRB afterglow will be in its FOV at the same time.

### 3.2.3 Modeling the X-ray background: RASS catalog

Up to now, a source catalog of transient sources has been created. However, this catalog does not provide a realistic scenario for the observed data, since no cosmic X-ray background or

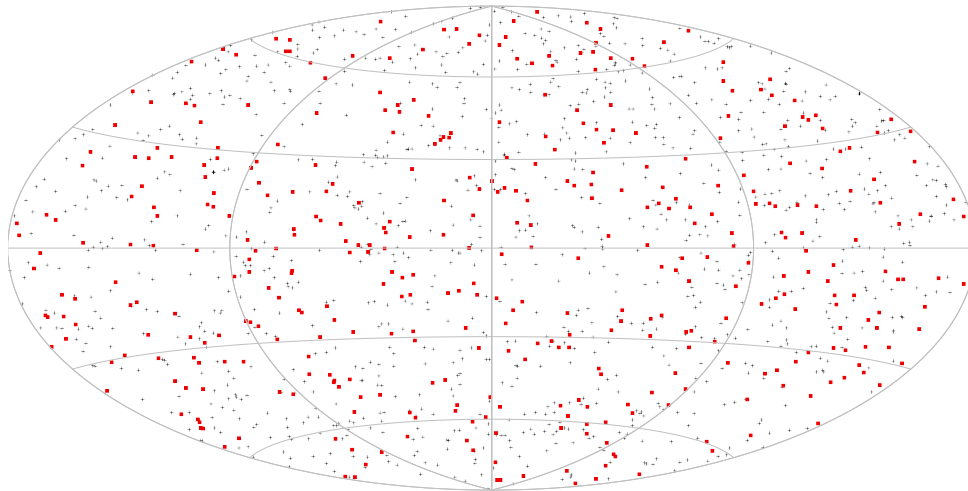


Figure 3.15: Positions of over 1061 GRBs from the *Swift* sample (black crosses) and the 400 GRBs contained in the created SIMPUT catalog (red squares) in Aitoff projection. The figure illustrates that the GRB population in both sets is uniformly distributed over the sky.

bright foreground sources are included yet. A simulation without this background or bright foreground sources would not allow reliable predictions about *eROSITA*'s performance, since the source detection is heavily dependent on the background. The cosmic X-ray background consists mostly of discrete point like sources, which need to be included in the simulation. Instead of modeling this background from scratch, I will use real data again, to keep the simulation as realistic as possible.

The most comprehensive catalog of X-ray sources up to now is the ROSAT all-sky survey (Voges et al., 1999). It was conducted in 1990-1991 by *ROSAT* (Trümper, 1990). *ROSAT*, short for Röntgensatellit, is a mission conducted by Germany, the United Kingdom and the United States and is the predecessor of *eROSITA*. Its primary aim was to perform the first all-sky survey in the X-ray band between 0.1 – 2.4 keV by scanning the sky in great circles. In 1999, the data was processed and the ROSAT all-sky source catalog (RASS) was published. The discovered sources are divided into two catalogs, the bright source catalog (RASS-BSC, (Voges et al., 1999)) and the faint source catalog (RASS-FSC). The RASS-BSC contains the positions and count rates of 18,811 sources, the RASS-FSC contains 105,924 sources<sup>8</sup>. the catalogs can be accessed via the web<sup>9 10</sup>.

A SIMPUT file is provided by the Remeis Observatory<sup>11</sup> containing all the sources from the faint and bright source catalog. The positions are directly taken from the catalog. The catalog only provides the measured count rates of the sources, SIMPUT, however, requires the the brightness given as a flux density distribution. The catalog provides conversion factors between count rate and flux for a power law spectrum. Therefore each source is assigned a power law spectrum with a photon index of  $\Gamma = 2$ . Then the count rate is converted to the corresponding flux. Although some sources show variable fluxes over time, all sources are assumed to have constant flux, therefore no lightcurve was assigned in the SIMPUT file.

The left panel of Fig. 3.16 shows the brightness distribution of the RASS catalog. The majority of sources are located in the peak between  $5 \times 10^{-14} \text{ erg cm}^{-2} \text{ s}^{-1}$  and  $2 \times 10^{-13} \text{ erg cm}^{-2} \text{ s}^{-1}$ .

<sup>8</sup><http://www.xray.mpe.mpg.de/rosat/survey/rass-fsc/>

<sup>9</sup><ftp://ftp.xray.mpe.mpg.de/rosat/catalogues/rass-fsc/>

<sup>10</sup><ftp://ftp.xray.mpe.mpg.de/rosat/catalogues/rass-bsc>

<sup>11</sup><http://www.sternwarte.uni-erlangen.de/research/sixte/simput/rass.simput.tgz>

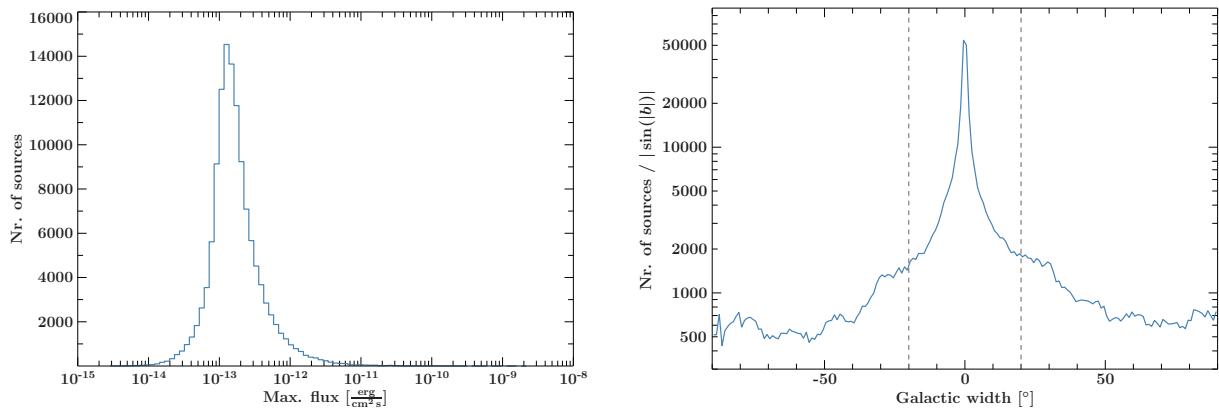


Figure 3.16: *Left:* The distribution of the fluxes in the entire RASS. The distribution peaks around  $1 - 2 \times 10^{-13} \text{ erg cm}^{-2} \text{ s}^{-1}$ , only 1053 sources are brighter than  $3 \times 10^{-12} \text{ erg cm}^{-2} \text{ s}^{-1}$ , which is the flux limit to be detectable by *eROSITA* with the presented detection algorithms. This means the gross of the sources will contribute to a seemingly diffuse background. *Right:* The distribution of sources as function of the galactic width  $b$ . The dashed line marks the area of the galactic plane with  $|b| < 20^\circ$ . A high concentration of sources in the galactic plane can be seen, as found by Voges et al. (1999).

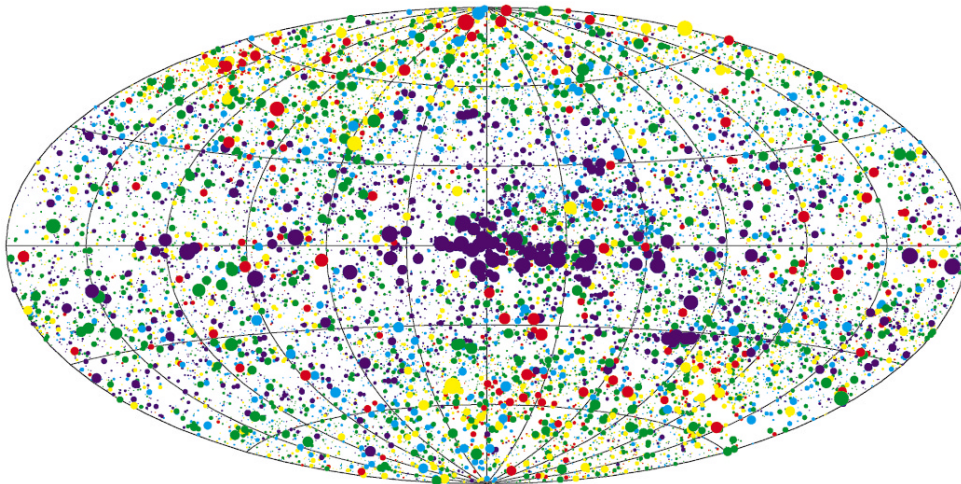


Figure 3.17: The distribution of the bright source catalog in Aitoff projection in galactic coordinates, taken from Voges et al. (1999). The galactic center shows a high density of bright sources with count rates  $> 1.3 \text{ ct s}^{-1}$ . Fainter sources are distributed uniformly. The color indicates the hardness ratio of the sources.

The peak is cut off for low fluxes, since the sensitivity limit of ROSAT is reached, therefore no darker sources can be detected.

Voges et al. (1999) and Fig. 3.17 show that bright sources with count rates  $> 1.3 \text{ counts s}^{-1}$  are clustered around the galactic center, which is between  $|b| < 20^\circ$ , where  $b$  is the galactic latitude. Assuming a power law spectrum with an index of  $\Gamma = 2$ , this count rate corresponds to a flux of  $7.28 \times 10^{-12} \text{ erg cm}^{-2} \text{ s}^{-1}$ . Fainter sources are distributed more uniformly over the sky. The right panel of Fig. 3.16 shows the distribution of sources as function of  $b$ . The distribution is divided by the sine of the galactic width to compensate the decreasing area closer to the poles. In good agreement, the distribution shows a high concentration of sources in the galactic disc and a uniform distribution outside the disc.

Assuming a uniform distribution, the average source density is  $8.36 \cdot 10^3 \frac{1}{\text{sr}}$ . This means, theoretically *eROSITA* has approximately 2.46 sources in its FOV at every time. However, as seen above, most of them are too faint to be resolved by the presented techniques, which means most sources will just be recognized as background.

The detection of sources is limited by the ability to distinguish them from the background. If the source is too faint, it will just fade into the background and can not be detected. In Sec. 5.2.4 I determine a flux limit of  $3 \times 10^{-12} \text{ erg cm}^{-2} \text{ s}^{-1}$  in 0.5–10 keV for sources to be detected by *eROSITA* with the presented source detection algorithm, taking only the cosmic ray particle background, see Sec. 5.2.3, into account. Therefore all sources fainter than that limit will not be resolved and recognized as sources, however, they still emit radiation. Sources fainter than the detection limit therefore are spuriously thought of background.

The RASS catalog contains 1053 sources brighter than  $3 \times 10^{-12} \text{ erg cm}^{-2} \text{ s}^{-1}$  in 0.5–10 keV which will act as bright foreground sources, the remaining sources are too weak to be resolved by my detection algorithm and will, in my case, contribute to an diffusive background. The RASS catalog is therefore appropriate to model the X-ray background for the all-sky survey simulations.

### 3.3 All-sky surveys and simulation runs

In the previous sections, I presented all components needed for the simulation of the all-sky survey: the simulator SIXTE, the instrument model of *eROSITA*, the creation of the SIMPUT file containing the transient sources as well as a SIMPUT file of all RASS sources modeling the cosmic X-ray background.

In this section I will describe how the single components were used to simulate the all-sky survey.

To perform the all-survey I used SIXTE and the instrument data as presented in Sec. 3.1.2. Since a simulation of a slew survey is made, an attitude file describing the observation strategy, i.e., how *eROSITA* will scan the sky, has to be provided. In this thesis, I used the file `eRASS_Pc87M55_3dobi_att.fits` provided by J. Robrade (priv. comm.). The eRASS will last four years, scanning the sky eight times, taking half a year for each scan. This way all regions on the sky will accumulate more exposure time with each scan.

Since the developed detection algorithm is based on an lightcurve analysis, an additional scan of a source half a year later does not change the lightcurve at the time of the first scan. Hence an additional scan of the sky would not immediately improve the detection process. I therefore restricted the exposure time of the simulation runs to half a year, scanning the entire sky only once.

The exposure time was cut into 185 shorter chunks, each lasting 85232 s. On the one hand, this speeds up the simulations vastly due to the possibility of parallelization, on the other hand, this reflects the reality better, since *eROSITA* will send its data in time intervals of one day.

The results and analysis of these simulation runs will be discussed in Sec. 5.3. At first, however, I will present the detection algorithm employed.



## Chapter 4

# Pile up

Pile up is called the phenomenon where two or more photons are interpreted as a single one during pattern recombination. If bright sources are observed, the number of incident photons per second is very high compared to the time needed to perform a detector readout. It is then likely that two or more photons hit the same or adjacent pixel on the detector during one frame. If the created pattern is invalid, the event is discarded. However, if the triggered pixels form a valid pattern, the readout process thinks that all energy stored in the affected pixels was deposited by a single photon. Therefore instead of several photons with low energies, a single event with a photon with a high energy is detected. These misinterpretations distort the measured spectrum and count rate, for examples see Fig. 4.1. A problem of pile up is that piled up events can not be distinguished of non piled up events in the instrument. **SIXTE** however can distinguish between piled up and regular patterns, since a detailed list of every incident photon is available. Therefore a good knowledge of the pile up behavior of the instrument is important to know when to expect pile up.

The following chapter about pile up is taken in verbatim, with small adaptations, from an internal document I prepared for the *eROSITA* collaboration.

### 4.1 Simulation setup

In this section, I describe the results of simulations performed in order to investigate pile up behavior of *eROSITA* for different fluxes and off axis angles,  $\theta$ , using the **SIXTE**. Real instrumental parameters and characteristics such as the point spread function (PSF) and the theoretical effective area (ARF) were used to keep the simulated data as realistic as possible. All seven detectors of *eROSITA* and a background model are taken into account.

All simulations are done for a point source with a spectrum described by a simple absorbed power law spectrum with photon index  $\Gamma = 2$  and a low foreground absorption of with  $N_{\text{H}} = 1 \times 10^{20} \text{ cm}^{-2}$ . I perform simulations corresponding to slews for eleven different off axis angles,  $\theta$  in  $0^\circ \leq \theta \leq 0.5^\circ$ . The slew speed is taken from the official attitude file of *eROSITA*. For each  $\theta$  we sampled 50 fluxes between  $1 \times 10^{-5}$  and 1 Crab, where  $1 \text{ Crab} = 2.4 \times 10^{-8} \text{ erg cm}^{-2} \text{ s}^{-1}$  in the 2–10 keV band. In the following, results for each combination of source flux and off-axis angle were averaged over the seven telescopes and at least nine simulation runs, in order to minimize statistical fluctuations.

I simulated both, observations in survey mode and pointed observations. In survey mode the source moves across the field of view (FOV) and therefore the off-axis angle varies with time. For these observations, in the following  $\theta$  will designate the minimum distance between the source and the optical axis during the slew. The exposure time in survey mode is determined by the duration of the source in the FOV and therefore by the attitude file. With increasing off-axis

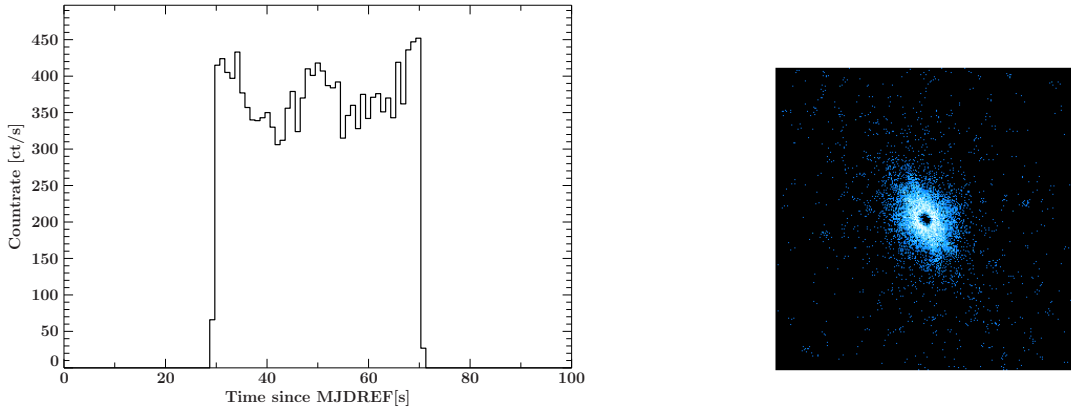


Figure 4.1: The left panel shows a lightcurve of the counts of a single telescope of an on axis slew over a source with a brightness of  $1.20 \times 10^{-8} \text{ erg cm}^{-2} \text{ s}^{-1}$  in 0.5–10 keV. Right panel shows an image of a source with a brightness of  $2.4 \times 10^{-8} \text{ erg cm}^{-2} \text{ s}^{-1}$  in 0.5–10 keV detected in a single on axis slew. Since the PSF is most narrow for on axis observations, all events are detected in a narrow region on the detector, causing a considerable amount of piled up events. The amount of discarded events is therefore highest, when the source is at the center of the FOV. At the border of the FOV, many photons are lost due to vignetting effects. The remaining events are distributed to a large area due to the broad PSF. The amount of pile up is therefore lower than in the center of the FOV, resulting in the shown lightcurve and image.

angle the exposure time decreases. Figure 4.2 shows the duration of the slew of a source across the FOV as a function of  $\theta$ .

## 4.2 Pile Up fraction

As mentioned, pile up in eROSITA is due to two effects:

1. Pattern pile up (or “grade migration”) means that two photons arrive in neighboring pixels during one read out cycle of the detector. In some cases, the resulting pattern will be recognized as a double event by the grade analysis, and therefore the event will be assigned an energy that is the sum of the energies of the individual photons.

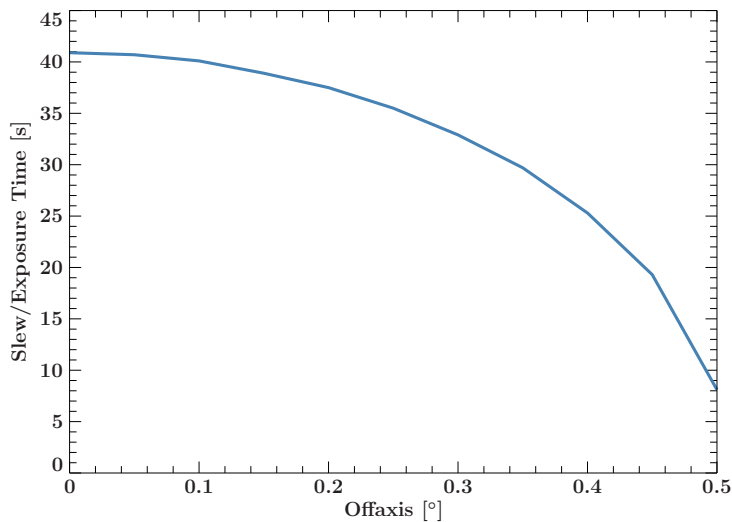


Figure 4.2: Duration of a slew of a source across the FOV for different off-axis angles in survey mode.

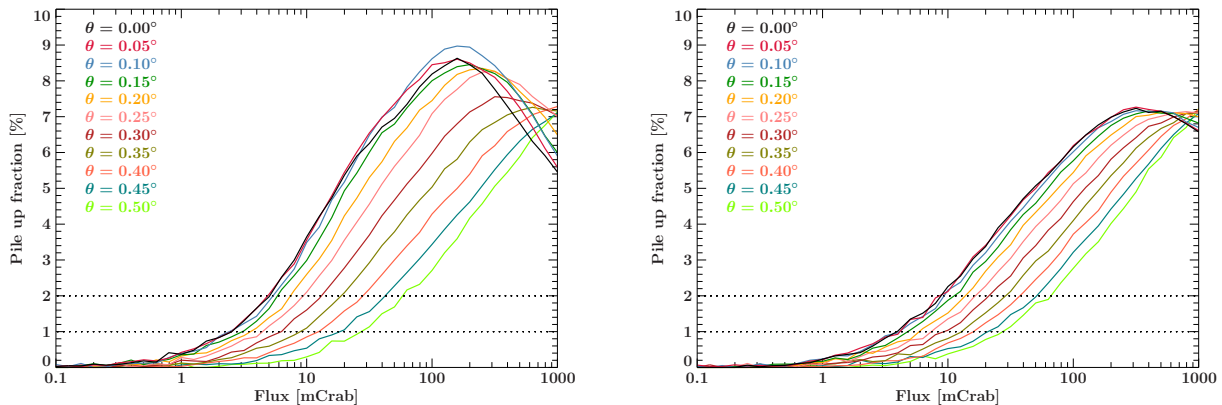


Figure 4.3: Pile Up fractions for pointed observation (left) and slews in survey mode (right). The 1% and 2% level of pile up fraction are marked by a dotted line. Note that for observation in survey mode, the given off-axis angle is the minimal distance of the the source to the optical telescope axis and the data therefore is averaged over all off-axis angles greater than the minimum. The data show significant amounts of pile up for fluxes between 1.5 mCrab and 20 mCrab for pointed observations and 3 mCrab and 20 mCrab in survey mode.

2. Photon pile up, on the other hand, is the case when two photons hit the same pixel during one read out cycle. Again, the energy assigned to the resulting event is that of a single photon of higher energy. Pile up therefore affects both the source count rate and therefore the flux assigned to the source, and the spectral shape.

As pile up will affect measured spectral shapes only if piled up events contaminate the measurable spectrum, we will characterize pile up in the following using the “pile up fraction”, that is the ratio events that are graded as “valid” but that are in reality piled up events, to the total number of valid events. The pile up fraction can be easily determined in our SIXTE simulations since we know which initial photons contributed to an event detected with eROSITA.

Figure 4.3 shows the pile up fraction as a function of the source brightness for both, pointed and slew observations. The dotted lines in the figure mark pile up fractions of 1% and 2%. Extensive simulations done in the course of the Athena-WFI work show that pile up fractions above 1% will lead to reconstructed spectral shapes that are wrong enough that scientific results are affected.

The behavior of the various lines in Fig. 4.3(right) needs further explanation. Shown is the pile up fraction for an observation in survey mode. This means that the off-axis angle of the detected photons change during the slew, since the position of the source relative to the optical axis changes. When the source first enters the FOV, its off-axis angle is at maximum of  $\theta = 0.51^\circ$ , then decreases to the minimal value as denoted in the diagram and then increases again until the source leaves the FOV. This means the shown data are averaged pile up fractions for different minimal off-axis angles.

This problem does not affect the pointed observation, since the source is at a fixed position and all photons are detected under the same off-axis angle.

The figures show that considerable amounts of pile up of above 1% are expected for pointed observations at fluxes between about  $1.5 \times 10^{-3}$  and  $2 \times 10^{-2}$  Crab, in survey mode between  $3 \times 10^{-3}$  and  $2 \times 10^{-2}$  Crab, depending on the observation mode and off-axis angle. Observations of sources with a high off-axis angle show less pile up than observations with a small off-axis angle. The reason for this effect is that the PSF widens with increasing off-axis angle, such that the photons are distributed over a larger detector area, which reduces piled-up patterns. Due to vignetting effects, however, the total number of detected counts can drop to values where

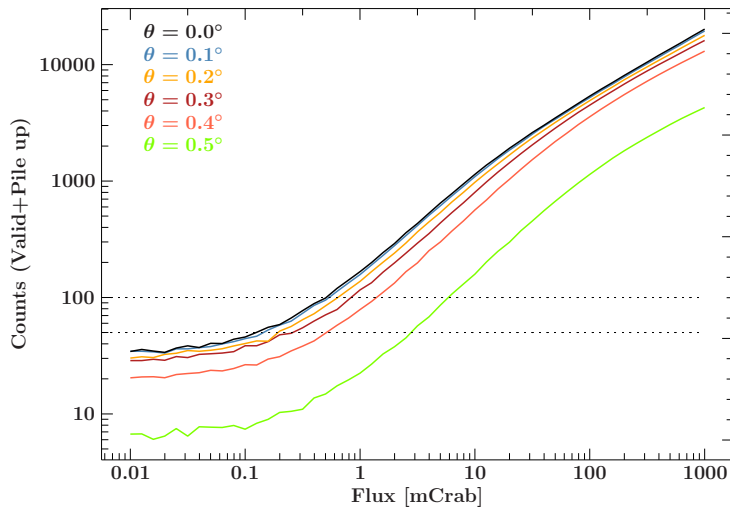


Figure 4.4: Total number of detected counts for one telescope during one slew as a function of off-axis angle. The horizontal dotted line marks when 50 and 100 counts are detected. Above these values, observations are considered to yield data that will yield more than mere positional information. Whereas an on-axis observation is useful at fluxes of 0.1 mCrab, for very high off-axis angles, sources need have fluxes of 20 mCrab. The number of counts for fluxes below 0.1 mCrab is dominated by background and does not reflect the number of source counts.

no statistically significant conclusion can be made. Figure 4.4 shows the number of detected counts in one slew in a single detector. The dotted lines mark the values of 50 and 100 counts, i.e., photon numbers where rough spectral shapes can be determined from simple spectral fits or X-ray colors. As expected, the count rate decreases significantly with increasing off-axis angles. An on-axis observation is useful for source with fluxes above 0.1 mCrab, for an off-axis angle of  $\theta = 0.5^\circ$  the flux required before astrophysical information apart from a source position can be obtained rises to 20 mCrab. This gives a flux limit to sources which can be observed at high off-axis angles.

I note a difference in the fluxes between pointed observations and survey mode at which the 1% pile up threshold is reached. This difference is caused by the fact that an observation in survey mode averages over all off-axis angles higher than the closest to the optical axis. As shown in Fig. 4.3, higher off-axis angles imply less pile up. Therefore a source slewing in and out the field of view causes less pile up at the borders of the FOV than in the center, decreasing the overall pile up fraction. This effect decreases for higher off-axis angles, since the interval of off-axis angles over which is integrated becomes smaller. A source with a minimum off-axis angle of  $\theta = 0^\circ$  passes through all off-axis angles in  $\theta \in [0^\circ, 0.51^\circ]$ , while a source with a minimum angle of  $\theta = 0.4^\circ$ , only averages over all angles in  $[0.4^\circ, 0.51^\circ]$ . As a result, at  $\theta = 0.5^\circ$  the 1% level is reached at the same flux for survey and pointed observations.

For really high fluxes above 100 mCrab a steep decrease in pile up fraction is seen. This effect is caused by the fact that a very large fraction of the detected events is discarded as they yield invalid patterns. This effect is addressed in the following section.

### 4.3 Count rates

In order to investigate the effects of pile up further, I calculated the mean count rates for the different fluxes and off-axis angles, taking the total number of valid events, including the events which suffer from pile up, and dividing them by the exposure time. These were averaged over all seven telescopes, so the count rates for a single detector will be shown.

Figure 4.6 shows how the count rate varies as a function of off-axis angle. The data show an almost linear rise of count rate with flux in the double logarithmic scale. All curves show a decrease of slope between 20 mCrab at  $\theta = 0^\circ$  and 100 mCrab at  $\theta = 0.5^\circ$ . This dip is caused

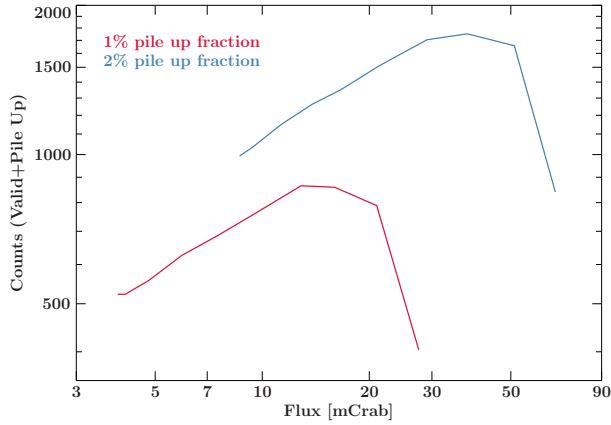


Figure 4.5: The number of accumulated counts on one detector during one slew over sources with fluxes resulting in 1% and 2% pile up fraction. The counts give a feel of the maximum number of counts which can be accumulated in a single slew before the spectrum is distorted by pile up.

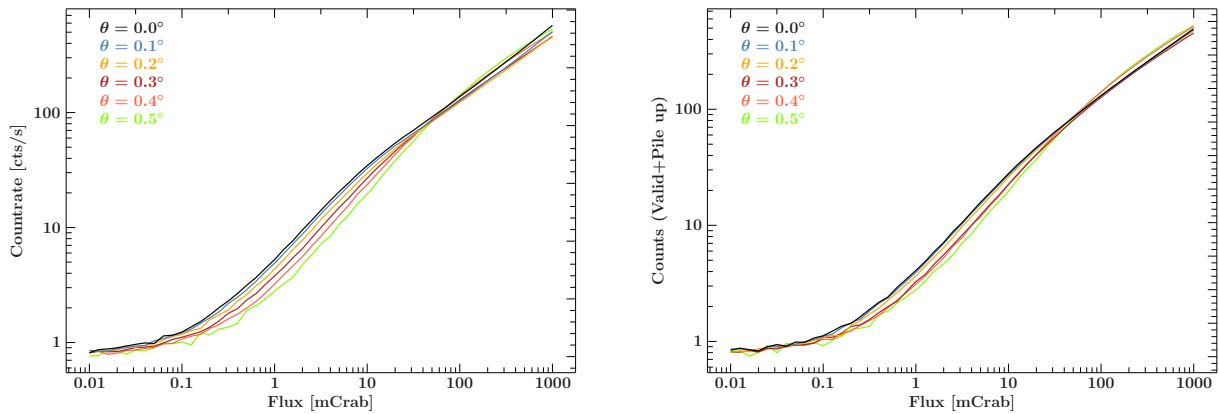


Figure 4.6: Average single telescope eROSITA count rates from sources of different fluxes during pointed observations (left) survey mode (right) for a single detector. Note the decrease in the slope between 20 mCrab and 100 mCrab caused by pile-up.

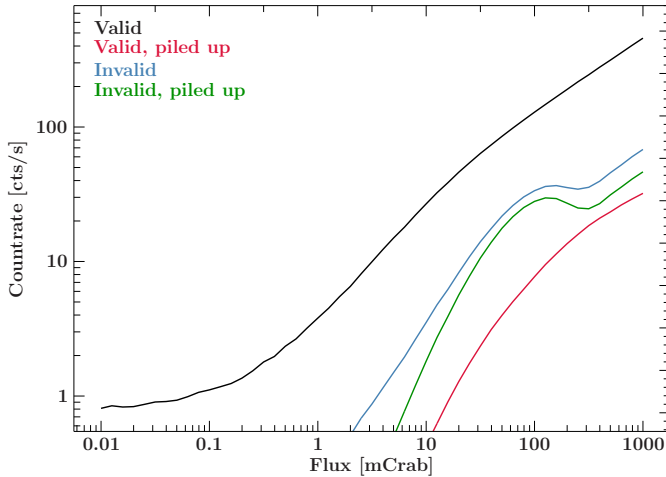


Figure 4.7: Count rates for valid, invalid, valid but piled up, and invalid and piled up events in pointed observations for a single telescope. A dip of the invalid count rate is prominent around 100 mCrab.

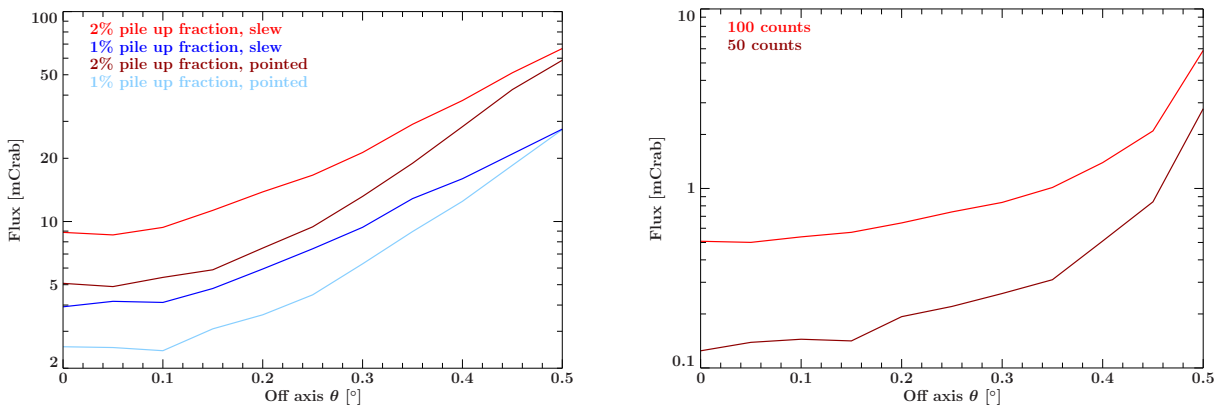


Figure 4.8: Critical fluxes as function of the off axis angle  $\theta$  for 1% and 2% pile up fraction (left) and for 50 and 100 counts (right). Fluctuations are due to numerical effects.

by pile up effects: Multiple photons arrive at the same time on the detector and are detected as a valid but piled up pattern or discarded because they generate a invalid pattern. In the first case, although several photons arrived, only one event is counted, in the second case no event is counted. This explains the decrease in the count rate even though more photons are reaching the detector (Fig. 4.7). This dip in the count rate causes the observed dip in the pile up fraction in the previous section.

For low fluxes below 0.1 mCrab we note a flattening of the curve to a constant. The contribution of the sources decrease with the flux, the overall count rate therefore fades out in the background count rate.

## 4.4 Conclusion

## 4.5 Conclusion

In this note we investigated the effects of pile up on observation and found critical fluxes starting at 1 mCrab for relevant pile up fractions for pointed and survey observations. Observing at increasing off-axis angles can reduce the pileup fraction due to ARF and PSF effects, however decreases the total number of detected counts.

For typical slew observations, a critical pile up limit of 1% is reached for source fluxes around 5 mCrab for sources passing centrally through the field of view, and for source fluxes around

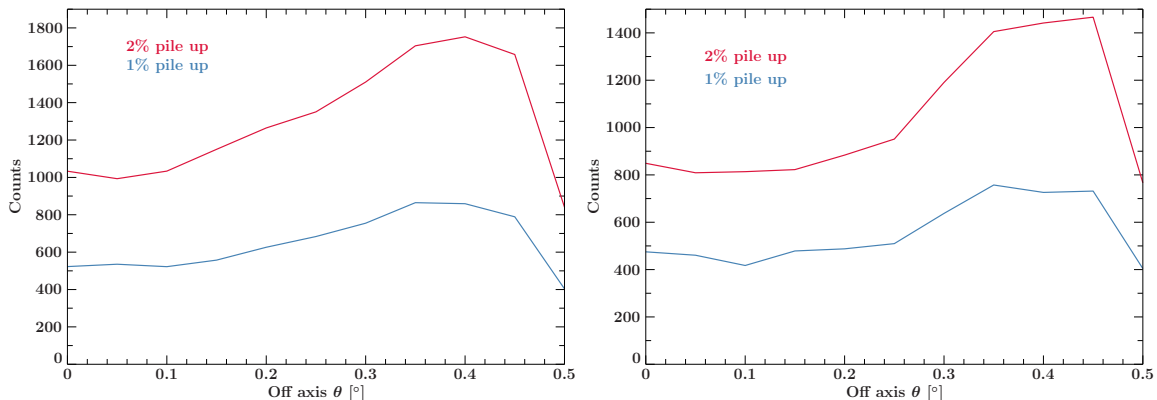


Figure 4.9: Accumulated counts in a single telescope after one slew as a function of off axis angle. To allow comparison, for the pointed observation we show the number of counts accumulated during the exposure time obtained at that off axis angle in slew observations. Due to the combined effects of vignetting and astigmatism, the maximum number of counts can be accumulated at an off axis angle at  $\theta \sim 0.4^\circ$  (survey mode) and  $0.35^\circ \leq \theta \leq 0.45^\circ$  (pointed mode). Fluctuations are due to numerical effects.

20 mCrab for sources passing at the edge of the field of view, as seen in Fig. 4.8 on the left.

Scientifically valuable single-slew data that allows to characterize the spectral shape of a source with the data from a single slew is expected to be obtainable for source fluxes above 0.1 mCrab if the source passes through the center of the field of view, and for fluxes above 20 mCrab for sources at the edge of the field of view, limiting the practical range of slew observations to about 10 mCrab, as shown in Fig. 4.8 on the right.

The number of counts which can be accumulated in one slew at the critical pile up fraction of 1% and 2% are between 400 and 800 counts at 1% pile up fraction and 800 and 1750 counts for 2% pile up fraction (Fig. 4.9). For sources with a pile up fraction of 2%, almost 1300 counts can be accumulated at an off axis angle of  $\theta = 0.45^\circ$ . For a more conservative pile up fraction of 1%, almost 800 counts can be accumulated at an off axis angle of  $\theta = 0.35^\circ$ .

For pointed observations, pile up will be significant for on-axis sources of a few mCrab. Here, pile up can be mitigated through off-axis observations which use the telescope's astigmatism. Such observations will allow pushing the high count rate limit of eROSITA to about 20 mCrab. Observations of brighter sources might be doable, however, by excising the core of the source.



## Chapter 5

# Source Detection

In this part of the thesis I will present the developed source detection process in detail. I will start by giving a short motivation and walk through of the general idea behind the pursued approach. The details on each step are presented in the following sections.

The **eSASS** (*eROSITA* Science Analysis Software System, I used version from Nov 8 15:17:32 2016) is the standard analysis tool for all *eROSITA* data. The **eSASS** is a software package which will process the raw data received from the instrument. One important task of this software is the source detection algorithm. Therefore it seems redundant to develop an alternative source detection algorithm. However, although the **eSASS** is a powerful analysis tool it has some disadvantages.

The **eSASS** is an elaborate pipeline, consisting of many different tasks. The processing of the data needs, besides the bare event list, housekeeping data as input. Furthermore running the complete pipeline is rather slow, compared to transient source phenomenons. Therefore the **eSASS** might not react quick enough to quickly detect the source and alert immediately follow-up observations of other instruments.

The concept of the presented algorithm is planed to pick up those disadvantages. The main purpose is, to provide a quick detection algorithm, which finds and locates bright transient sources very quickly, in order to provide the necessary information for follow up observations.

The only input data needed by the algorithm is the event list, which contains all detected photons with their time stamp and detector coordinates, and the attitude of the spacecraft. Saving time by passing on steps like image processing, the detection process is quick enough, to locate transient sources in time to trigger follow up observations.

The underlying principle of the detection process is that if sources enter or leave the FOV of the telescope the detector count rate changes. If the telescope is looking into an empty area of the sky, it only detects background. As soon as a source enters the FOV, the detector is exposed to additional photons originating from this source and the count rate rises. When the source leaves the FOV, the count rate drops back to the background radiation. Such points, where the count rate changes, are called change points. Given a specified survey strategy and source position, each source enters the FOV at a specified time  $t_s$  and also needs a certain amount of time  $\Delta t$  to move through the FOV. Each source which was seen by the telescope can be assigned a time interval of the exposure time. This means that all events caused by photons originating from this source have a time stamp in the interval  $[t_s, t_s + \Delta t]$ . If a source position is known, the time at which a source is seen can also be calculated with the attitude data of the spacecraft and vice versa. If the detection time is known, the source position can therefore be calculated.

The presented source detection makes use of this behavior. It searches change points, therefore times where sources enter or leave the FOV, in the event data. These intervals can then be assigned to sources. To facilitate this search, a more appropriate representation of the event

data is used, namely the lightcurve. A lightcurve is close to a histogram of the time tags of the photon events. This means the exposure time is segmented into time intervals, called bins, with start point  $t_j$  and end point  $t_j + \delta t$ . Then each photon with the time stamp  $t_i$  is put in the bin where  $t_j < t_i < t_j + \delta t$ . Each bin is divided by its width yielding the count rate of photons in each bin. Lightcurves therefore give the count rate as a function of the time. Example lightcurves from simulated observations are shown in Fig. 5.9 and Fig. 5.14.

Although lightcurves are probably the most popular visualization of event data, the binning of the time tags may cause lose of information (Scargle, 1998). If the bin width is chosen too large, short scaled features may be averaged out (Worpel & Schwöpe, 2015). The optimal choice of a bin width  $\delta t$  therefore is a difficult question. See (Worpel & Schwöpe, 2015) for further information. Since the loss of short time lightcurve features degrades the source detection, another approach called bayesian blocks is chosen. The bayesian block algorithm finds an optimal segmentation of the event data by trying to detect change points and place the bin edges there. This means instead of dividing the exposure time into equally spaced intervals, the bin widths are chosen variable to emphasize features of the lightcurve. In perfect condition, each detected source would get assigned its own bin, separated by bins containing only background. However, due to the high source density in the sky, often several sources are grouped together in a single bin. A detailed discussion of the optimal segmentation of lightcurves is found in Sec. 5.1.

This optimal lightcurve is then scanned for bins representing sources. The set of detected sources has to be filtered, since the detection method finds permanent sources as well as transients on the other hand. However for our purpose, only transient sources are of interest. I therefore present two different approaches to this problem, both based on using existing catalogs to match known sources. Therefore a catalog of all known sources is provided. The detection scripts then compares this reference catalog with detected sources to find formerly unknown ones.

The first method iterates through all photons contained in the bin and checks, if it originates from a known source. Only if the photon could be assigned to no source, it is kept for further processing, all other photons are discarded. Therefore only photons from new sources are processed and the contribution of known sources is omitted. Detailed information about this process can be found in Sec. 5.3.3

The second approach uses the traditional lightcurve with constant width bins. Each source detected leaves a characteristic feature on the lightcurve. For each bin the expected lightcurve can be constructed, since the shape of the features can be determined. The constructed lightcurve is compared to the measured one. On the basis of strong variations new sources can be found. This method is presented in detail in Sec. 5.3.3.

Finally, the temporal location of the source on the lightcurve needs to be converted in sky coordinates. To achieve this, either the attitude data of the spacecraft is used or the original coordinates of the detected photons, calculated by the sky projection of the detector coordinates.

The source detection can be summed up in the following steps:

1. Find an optimal segmentation of event data
2. Determine background count rate
3. Check for bins with significant count rates
4. Filter transient sources from background sources
5. Determine sky coordinates of sources

In the following section, we will present the source detection algorithm in detail, by discussing each step of the pipeline in detail.

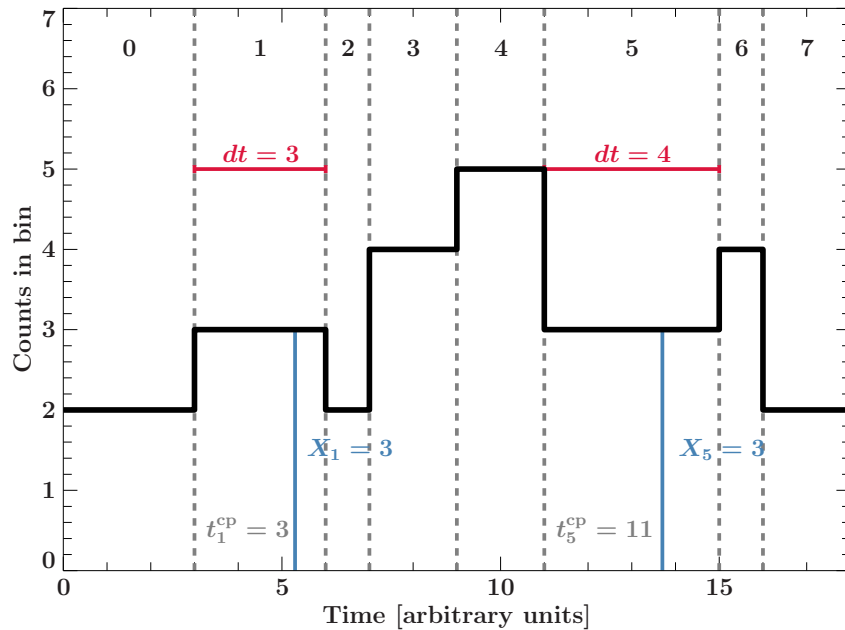


Figure 5.1: An example of a piecewise constant model consisting of  $N_{\text{cp}} = 8$  blocks. The parameters of two blocks are marked and given by  $t_1^{\text{cp}} = 3$ ,  $X_1 = 3$  and  $t_5^{\text{cp}} = 11$ ,  $X_5 = 3$ . The width or length of the blocks is given by the position of the adjacent change points:  $dt_1 = 6 - 3 = 3$ ,  $dt_5 = 15 - 11 = 4$  and therefore not a free parameter of the model.

## 5.1 Bayesian block analysis

The bayesian block algorithm (Scargle, 1998; Scargle et al., 2013) was originally developed to circumvent aforementioned problems analyzing small scale time features in lightcurves with equally sized bins. It is a method to detect localized features and separate them from the observational errors in the lightcurve. It is a non parametric analysis meaning that no prior information about how the searched features look like is needed and therefore biases by wrong priors are avoided.

### 5.1.1 The piecewise constant model

The following sections are all based on (Scargle et al., 2013). A generalized version of a histogram, also called piecewise constant model, is employed to describe the event data. An example model is shown in Fig. 5.1. The main differences to a regular histogram are that the bins are not equally sized, nor is the number of bins predefined. In fact, the bins are chosen to reveal and emphasize features of the lightcurve. Therefore the bin edges are positioned at points, at which the rate of event data changes, namely the change points. Finding the optimal piecewise constant model is therefore closely related to finding an optimal segmentation of the data, with optimal meaning that no information is lost due to wrong binning. The segments found by this partition will be called herein blocks. The piecewise constant model therefore is a continuous sequence of blocks, describing a step function.

In theory, there is an infinite number of such step functions, since the number of change points, and therefore blocks, is variable and every point of the time axis can be used as a change point. The challenge is to find the model which fits the data best and therefore maximizes a goodness-of-fit function. A quantitative description of all possible models is needed to evaluate such a function. Hence, the following parameters are introduced:

- $N_{\text{cp}}$  denotes the number of change points of the model
- $t_k^{\text{cp}}$  denotes the temporal location of the  $k$ -th change point
- $X_k$  is the signal amplitude in the  $k$ -th block, therefore how many counts are contained in each block

Each step function is uniquely defined through these parameters. Note that the locations of the change points  $t_k^{\text{cp}}$  give the optimal segmentation of the event data and determines the number of blocks. Since the first point is always considered a change point, the  $i$ -th segment, or block, spans the time interval  $[t_i^{\text{cp}}, t_{i+1}^{\text{cp}}]$ , its length is therefore  $t_{i+1} - t_i$ . Since the signal height in each block is the number of events contained, it is not a free parameter, but determined by the location and width of each block. A key property of the piecewise constant model is that the fitness, a measurement describing how well the block with the present parameters describe the data, of a single block only depends on the contained data and does not affect the fitness of other blocks. The goodness-of-fit function for the entire segmentation is then only the sum of the goodness-of-fitness functions of each block.

### 5.1.2 Finding the optimal segmentation

The main difficulty is to find the optimal segmentation of the data, therefore finding the change points. In our case the real event data will have change points at times, where a source enters or leaves the FOV, since the count rate will change significantly. Therefore finding those correct places of the change points is a very important step of our source detection algorithm. The following description of the algorithm follows closely Scargle et al. (2013).

The first step to find the optimal segmentation is to divide the continuous time space into cells in a way that each photon arriving time is assigned into one cell. Therefore each cell contains only one photon. Exceptions where two photons arrive at the same time are possible, the cell then contains two photons, but does not compromise the algorithm. The cell is defined as a Voroni Tessellation (Okabe et al., 2009) of the time axis, the cell containing the  $i$ -th photon is defined as the interval  $[\frac{t_i - t_{i-1}}{2}, \frac{t_{i+1} - t_i}{2}]$ . It spans from the midpoint between the arrival time of the  $(i-1)$ -th and the  $i$ -th photon to the midpoint between the  $i$ -th and  $(i+1)$ -th photon. A block then consists of one or more cells, which results in a total number of possible partitions of  $2^N$ , where  $N$  is the number of cells. Although this is a very big number for typical observations, it is not infinite. A partition of the entire observation is a set of defined blocks, and an optimal partition is a set of blocks, which maximizes the goodness-of-fit function.

A goodness-of-fit function is a measure of how well a model describes data. The function takes as input the model and its parameters and returns a value, the so called fitness of the model. The higher this value is, the better the model fits the data. With such a function, the best model between a set can be chosen, by picking the one with the highest fitness. A goodness-of-fit function can be chosen arbitrarily.

As mentioned, the goodness-of-fit function for the piecewise constant model has to be additive for multiple blocks. The fitness of a single block has to depend on only the data contained in the own block. Since the function is additive, it suffices to define a block fitness function, rather than a model fitness function. There are multiple valid fitness functions that fulfill the required properties. We employed the one used by Scargle et al. (2013):

$$\log L_{\text{max}}^{(K)} = N^{(k)} \left( \log N^{(k)} - \log T^{(k)} \right) \quad (5.1)$$

This specific function has the useful property to be invariant to time scaling and is only a function of the length and the number of photons in a block, as demanded. With this fitness function, the bayesian block analysis is complete.

The most trivial solution to the problem of finding the optimal partition of  $N$  cells is of course the one, where each block consists of only one cell respectively photon. This would, however, result in a complicated model with  $2N$  parameters, which is not desirable due to the expensive evaluation of the model. The bayesian approach to model selection comes with a built in penalty for complex models with a large number of parameters, if the data do not justify this model. Since the bayesian Block algorithm is based on the bayesian approach of model selection, the trivial solution receives a high penalty for model complexity, which prevents the trivial to be chosen. For more information on this topic, see (Gregory, 2005).

To understand the algorithm, the following property of partitions is needed: If the last block of an optimal partition is removed, the remaining partition is still optimal. This property results from the additive nature of the step function model, where each block maximizes the goodness-of-fit function on its interval. Removing the last block therefore leaves a partition of blocks, which each maximizes the goodness-of-fit function, therefore the entire partition is still optimal.

The algorithm makes use of dynamic programming<sup>1</sup> and uses the principle of mathematical induction, adding one more cell at each step using the results received in the previous step. After each step, the values of the fitness of the optimal partition, as well as the position of the last change point found are stored.

The first step only contains one cell, the optimal partition therefore is trivial. Assuming, the optimal partition of the first  $R$  cells is already found, the optimal partition of the first  $R + 1$  cells needs to be found. The last block ends at cell  $R + 1$  and can begin at any cell  $r \leq R + 1$ . The remaining subpartition of the first  $r - 1$  cells needs to be optimal for the entire partition to be optimal, which leaves only one optimal subpartition. The fitness value of each of these optimal subpartitions is already known from previous steps. The total fitness value therefore is the sum of of the fitness value of the optimal partition of the first  $r - 1$  blocks and the fitness value of the last block.

For each step,  $r$  runs from 1 to  $R + 1$ , therefore the size of the last block is varied from containing all cells to only containing the last one. The fitness value of each of the resulting partitions is calculated. This value is simply the sum of the fitness value of the optimal subpartition of the first  $r - 1$  cells and the fitness value of the last block from  $[r, R + 1]$ . Therefore a set of  $R + 1$  fitness values is calculated. The optimal partitioning of the first  $R + 1$  cells is the maximum of this set of fitness values. The corresponding value of  $r$  marks the position of the latest change point.

Since this step is performed for each data cell, the overall complexity of this algorithm lies in  $\mathcal{O}(N^2)$ . At last, the positions of the change points have to be reconstructed. All relevant information is directly available, since the last change point for each optimal subpartition has been stored. The first change point is simply the last one detected at the cell  $r$ . Omitting the last block leaves us with the optimal subpartition of the first  $r$  cells. The next change point is the last one detected in the step, where  $R + 1 = r$ , therefore the value of last change points which were stored in this step. In this way, all change points can be determined.

### 5.1.3 Sensitivity of the algorithm

The basic functionality of the algorithm has been presented. In this section, I want to elaborate on an important parameter of the algorithm, the prior guess on how many change points will be found in the data. It is called `ncp_prior`. This parameter controls the sensitivity of the algorithm, therefore how much the event rate has to change to trigger a change point. How this parameter works in the algorithm is described in (Scargle et al., 2013).

---

<sup>1</sup>Dynamic programming is a concept to store calculated values which will be needed again and reuse those, instead of calculating them again.

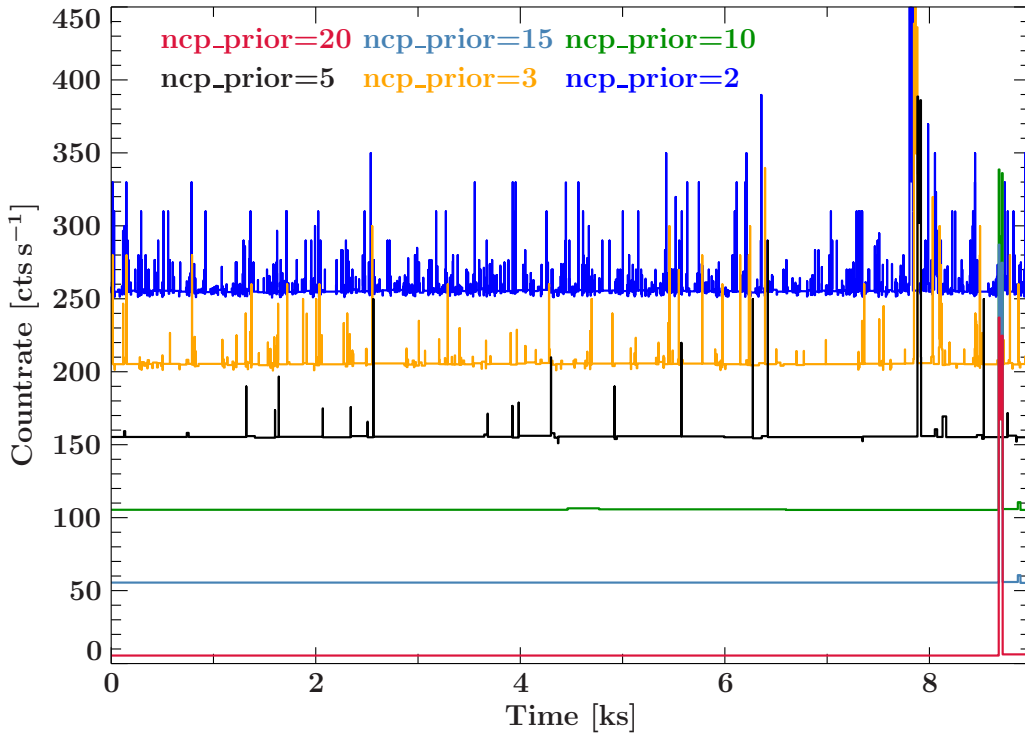


Figure 5.2: An extract of lightcurves of an all-sky survey. The bayesian blocks are shown for different values of `ncp_prior`, meaning different sensitivities of the algorithm. Lower values cause higher sensitivities. An offset is added to each lightcurve for better presentation. As can be seen, the sensitivity has a huge impact on the number of blocks and the visible features in the lightcurve.

Choosing the sensitivity of the algorithm is always a trade off. For high sensitivities, fluctuations in the background of the signal may suffice to trigger a change point, reducing the signal to noise ratio of the analysis. A low sensitivity is more likely to ignore all background, but will probably miss some change points.

To investigate the actual effects of `ncp_prior` on the resulting lightcurves, I applied the algorithm several times to the same set of data, varying `ncp_prior`. The data I used is an extract of a lightcurve from an simulation of an all-sky survey. As can be seen in Fig. 5.2, increasing the sensitivity of the bayesian block algorithm significantly increases the number of blocks and therefore features found in the lightcurve.

Finding the optimal value of `ncp_prior` is not a trivial problem. It depends on many factors, like the nature of the background, but also on the intended use of the resulting lightcurve. If for example only a few, very bright sources wants to be detected, a low sensitivity suppresses the background, while the bright source will still be detected. Throughout the thesis, if not mentioned differently, I employed the built-in automatic detection of `ncp_prior` proposed in (Scargle et al., 2013).

## 5.2 Source detection and lower detection limit

In this section, I will illustrate the bayesian block analysis, how it is used to detect sources and point out the most crucial problems.

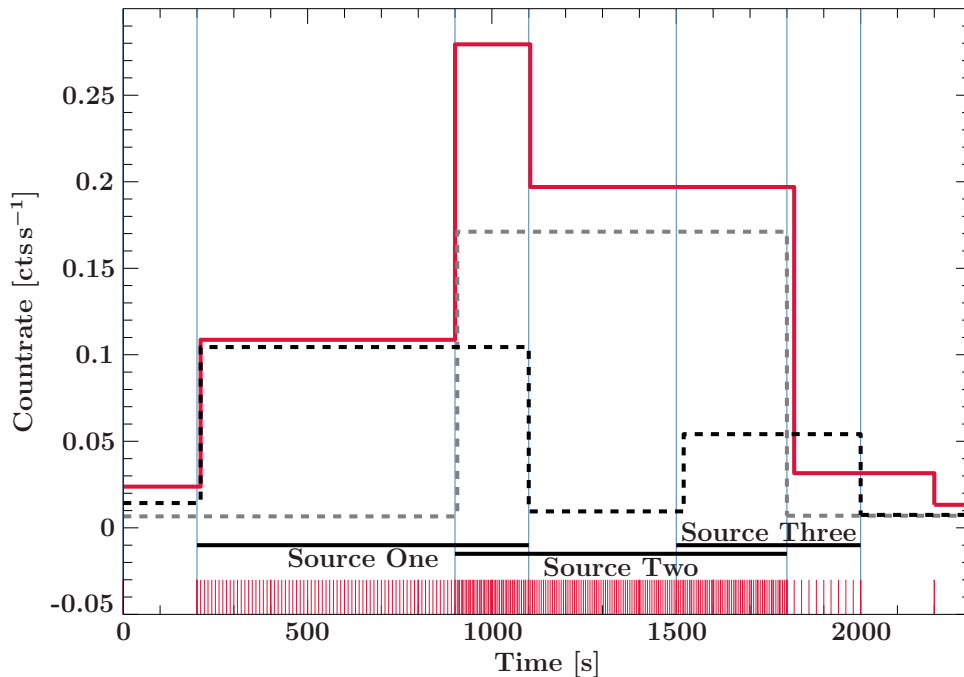


Figure 5.3: An example of a bayesian analysis of artificial event data, emitted by three sources. Turning sources on and of may be interpreted as a slew observation over those sources, the marked interval indicate the time during which the sources are seen. Each red line at the bottom indicates a detected photon, the blue lines mark the correct positions of the change points in the event data. The dashed lines is a bayesian analysis, if each source is detected isolated in an extra slew. As can be seen, the bayesian block analysis reliably detects the change points and finds the optimal lightcurve. Each block can uniquely be identified with a detected source. The red line is the optimal lightcurve found in an observation including all three sources as indicated in the figure. Nor all change points are detected correctly, neither is clear identification of blocks created by single sources possible due to the overlap.

### 5.2.1 Basic source detection principle

The basic principle of the source detection will be discussed with an example. An artificial event list was created, based on the following count rates during the intervals:

- $200 \leq t \leq 1100$ : an event every 10 s, source one
- $900 \leq t \leq 1800$ : an event every 6 s, source two
- $1500 \leq t \leq 2000$ : an event every 20 s, source three

Figure 5.3 illustrates this example. The given intervals are drawn as black lines at the bottom. Each thin red line at the bottom indicates an event. The situation can be seen as a slew observation of three sources. During the denoted time interval the source is in the FOV and therefore contributes to the total count rate: in  $[200 \text{ s}, 1100 \text{ s}]$  only source one is visible, in the interval  $[900 \text{ s}, 1100 \text{ s}]$  source one and two are in the FOV at the same time, in  $[1100 \text{ s}, 1500 \text{ s}]$  only source two is visible, in  $[1500 \text{ s}, 1800 \text{ s}]$  source two and three are in the FOV and in  $[1800 \text{ s}, 2000 \text{ s}]$  only source three remains in the FOV. Since the exact event data are known, the correct change points can be determined exactly at either edge of each given source interval, which is equivalent to a source entering or leaving the FOV. These change points are marked by blue lines in Fig. 5.3.

First we start of with a simplified setup. Source two is omitted, therefore at any time at maximum one source is in the FOV. This means there is no overlap of contributions of the single sources to the total count rate. The expected optimal lightcurve would therefore have a rising flank at  $t = 200$  and a falling flank at  $t = 1100$  when the first source enters and leaves the FOV. The same happens for the second source at  $t = 1500$  and  $t = 2000$ . The lightcurve calculated by the bayesian block algorithm is drawn as a black, dashed line. As can be seen each expected change point at  $t_{cp} = 200, 1100, 1500, 2000$  is detected correctly.

Looking at this lightcurve, we see that at the first edge the count rate rises, therefore a source has entered the FOV. When the count rate drops, it has left the FOV. Therefore seeing this block, we know that the telescope has seen a source and we can assign this first block source one. Analogue, the second block was caused by slewing over source three. This procedure is the basic source detection process and works well for single sources. During the thesis, I will call sources resolvable if both change points caused by the source are detected properly.

Problems arise if there is an overlap of sources, meaning that two sources appear in the FOV at the same time. In this case, the detected change points can not be associated uniquely with the events of sources entering or leaving the FOV. Consider the case including all three sources as listed above. We would expect the following lightcurve: a rising flank at  $t = 200$  when source one enters the FOV, another rising flank at  $t = 900$ , when source two appears, since both count rates add up, then a falling edge at  $t = 1100$  since source one leaves the FOV. At  $t = 1500$  source three enters the FOV, therefore a rising edge should appear, before it falls at  $t = 1800$  again, when source two leaves. At  $t = 2000$  the lightcurve should drop back to zero. The described lightcurve should therefore just be the sum of all optimal lightcurves of the single source slews, marked with dashed lines in Fig. 5.3.

The lightcurve found by the bayesian block algorithm differs from the theoretical expectations. The first three change points are detected correctly, however, no new bin was started when source three enters the FOV and the change point when source three leaves is detected at the wrong position. While all blocks were correctly detected when observed individually (dashed lines), this example shows that the algorithm has difficulties to detect change points within overlapping features, like multiple sources simultaneously in the FOV.

However, even if all change points would have been detected correctly, no unique assignment of blocks to sources could have been made. Consider the red curve in Fig. 5.3. It is clear that the first rising edge is a new source entering the FOV. Already at the next edge, however, there are multiple possibilities: (1) the source presently in the FOV leaves, while a new, brighter source enters (2) an additional source enters the FOV (3) two or more sources entering the FOV shortly after each other. Emerging from these possibilities there are even more possible interpretations of the next falling edge.

Another problem are vignetting effects. If a source enters the FOV, the vignetting function at the borders of the optics are lower, reducing the measured count rate. The count rate therefore rises, as the source slews into the center of the FOV. As a result, bright sources can create more than one change point while entering and leaving the FOV, an example is shown in Fig. 5.12.

At last, not only sources can trigger change points but fluctuations in the background. The average background count rate is constant, the number of events in a time interval, however, follows the Poisson statistic. Therefore a bunching of background events can create a block in the lightcurve.

To summarize, the following problems needs to be solved:

1. Overlapping sources: single blocks contains contributions of more than one source
2. Sources spread over multiple blocks: a single source triggers more than two change points
3. Background: fluctuations in the background can trigger false source detection

Points (1) and (2) are closely related to filter new transient sources from already known ones. Therefore I will address these points in the specific section. How to filter sources from background radiation will be the topic of the next section.

### 5.2.2 Filter sources from background radiation

The number of photons emitted by a source in a time interval  $\delta t$  is primarily determined by its brightness, which corresponds to a certain photon emission rate  $\lambda$ . Based on this emission rate, the theoretical photon count in the interval  $\delta t$  is fixed at  $\delta t\lambda$ . However, the emission of photons is a statistical process which follows the Poisson statistics. The number of photons is then distributed around the mean value  $\delta t\lambda$  according to

$$P(N) = (\delta t\lambda)^N \frac{e^{-\delta t\lambda}}{N!} \quad (5.2)$$

The standard deviation of this distribution is given by  $\sigma = \sqrt{N}$ .

Since the number of background counts is also Poisson distributed, an excess above the expected background for a period of time is possible. The bayesian block algorithm will detect change points at the start and end of such an excess interval, since it seems that the count rate changed. This block, although being caused by background fluctuations, is then spuriously detected as a source. Since such false detections are not desirable, they has to be identified and discarded.

A block caused by background fluctuations is not definitely distinguishable from a block caused by a real source. However the probabilities for the block to contain a source can be calculated. A block is then assumed to be a source, if a threshold probability is exceeded.

Since all measurements are contaminated by background events, the real number of counts  $S$  from a source can never be measured directly, but needs to be calculated with the number of total counts  $C$  and the background counts  $B$ :

$$(S \pm \Delta S) = (C \pm \Delta C) - (B \pm \Delta B) \quad (5.3)$$

All of these values are Poisson distributed and therefore subject to statistical fluctuations. The standard deviation  $\sigma S$  of the source counts can be calculated from the uncertainties of  $C$  and  $B$ :

$$(\sigma_S)^2 = \left( \frac{\partial S}{\partial C} \sigma_C \right)^2 + \left( \frac{\partial S}{\partial B} \sigma_B \right)^2 = (\sigma_C)^2 + (\sigma_B)^2 = C + B \quad (5.4)$$

To calculate the probability of a measurement of a photon count  $S$  related to the expected value  $\bar{S}$ , the signal to noise ration (SNR) is introduced

$$\text{SNR} = \frac{S}{\sigma_S} = \frac{C - B}{\sqrt{C + B}} > 5 \quad (5.5)$$

A SNR = 5 means that the probability to measure a photon count outside the Interval  $\bar{S} - 5\sigma < S < \bar{S} + 5\sigma$  is  $5.7 \times 10^{-3} \%$ . Related to the source detection, this value therefore indicates the probability that a block caused by background fluctuations is assumed a source.

Therefore we can filter all blocks caused by background by calculating its SNR. Only blocks with an SNR exceeding 5 are accepted as sources, since they are very likely to be triggered by a source, while all other blocks are discarded.

### 5.2.3 Background analysis

The background analysis is an important step in every observation. Since all observations are contaminated with background, only a good knowledge of the background allows a precise analysis of the data.

Background in X-ray observations can be split into two contributions: the cosmic ray particle background and the X-ray background (Bradt, 2004):

**Particle background** The particle background is caused by cosmic particles, which deposit charges by interacting with the detector material. These can be for example protons emitted from the sun or high energy particles from other galaxies (Read & Ponman, 2003). SIXTE provides built in support to include particle background, based on simulations by Tenzer et al. (2010).

**X-ray background** The X-ray background consists of photons which are emitted from sources, which are too faint to be resolved, e.g., distant AGNs. Furthermore, photons from sources outside the FOV can be reflected onto the detector (Read & Ponman, 2003). Although uncommon, I will include bright foreground sources in the X-ray background, since for our purposes, these are sources I am not interested in. The X-ray background is not an included feature of SIXTE, therefore the RASS catalog was included to provide a realistic X-ray background, see Sec. 3.2.3.

In this thesis, the background has direct impact on the measured count rates and therefore the detection sensitivity. Therefore determining the background rate is an important step in the presented detection process.

In a pointed observation the background can be determined by pointing the telescope into an empty region of the sky and measuring the count rate. In survey observations this method is not possible, therefore another method to determine the background count rate has to be found.

I present two different approaches to determine the background count rate for survey mode observations. The first one uses the optimal lightcurve segmentation obtained by the bayesian block analysis, the second approach utilizes the classical lightcurve with equally spaced bins. To adjust for changing conditions during the survey the background determination is performed for each day-length chunk of the survey. At first I will explain the two approaches, then the results and a short discussion will be presented.

#### Background determination with bayesian blocks

The first approach works with the optimal binning of the lightcurve by bayesian blocks. The time a source needs to slew through the FOV of the telescope can be calculated from the off axis angle of the source and the slew speed of the telescope. A plot of the slew times is shown in Fig. 4.2. As can be seen, the maximum length of a slew is about 41 s. A source bright enough to be resolvable therefore can generate a block with a maximum width of 41 s. Hence, a change point is expected after at least every 41 s.

No change point after a period of time longer than 41 s therefore implies that no bright source has entered or left the FOV and the FOV has to be empty. Therefore all blocks lasting longer than 41 s can only contain background counts. Note that sources not bright enough to be resolved in the lightcurve are considered as background in this approach. There is the chance that if a source leaves the FOV an equally bright source enters the FOV at the same time. The probability of this situation to happen is very low, therefore this case will be neglected.

The background count rate can be calculated by averaging the count rates over all blocks lasting longer than a threshold. The background rate determined by this approach is therefore a

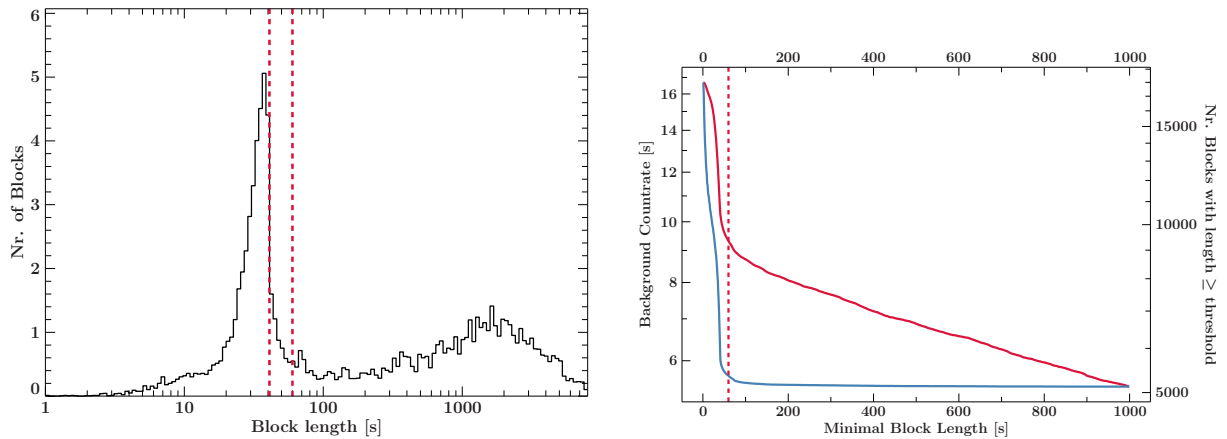


Figure 5.4: *Left:* Histogram of block length of a bayesian block lightcurve of a day length chunk of an all-sky survey, averaged over 185 days. Dashed lines indicate max source slew time at 41s and background cutoff at 60s. A clear cut off after the maximum block length is visible. *Right:* Determined background count rate (blue) and the number of blocks (red) as function of the cutoff length of blocks. Dashed line marks the cutoff length of 60s used in this thesis.

function of the cutoff value of block length. For example a cutoff length below 41 s would surely include source counts, therefore overestimate the real background count rate. The distribution of block length in a bayesian block lightcurve of a day-length chunk of the simulated all-sky survey containing both transient and the RASS sources is shown in Fig. 5.4 on the left. On the right the background count rate is drawn as a function of the cutoff length.

The distribution of block lengths in Fig.5.4 (left) shows a peak around the maximum slew time of 41 s, which extends up to 60s due to the statistical nature of the bayes in blocks, where a local minimum is found in the distribution. The right plot in the figure shows the background rate and the number of blocks with lengths above the cutoff as a function of the threshold length. At a cutoff length of 60s, the slope of the background significantly decreases and fades into an almost constant value. Furthermore, the number of blocks longer than the cutoff shows a kink around 60s transforming to a linear behavior. Since both plots show significant changes around a threshold length of 60s, and a homogeneous behavior afterwards indicating background contribution, I chose a threshold time of 60s. The resulting background rate for different simulation setups is listed in Tab. 5.1.

Although strong indicators hint to chose the cutoff length at 60 s, there is not a unique choice for the parameter. However, a lower limit can be set to 41 s. Increasing the threshold length causes only small changes on the background rate, as shown in the right hand panel of Fig. 5.4. Varying the cutoff length between the valid interval of  $[41 \text{ s}, \infty)$ , the background rate for the survey including RASS and transient sources shows variations of  $\approx \pm 0.4 \text{ ctss}^{-1}$ . Such variations however will not have significant impact on the detection process.

### Background determination on lightcurves with constant binning

The second method to determine the background count rate in a survey observation is based on a lightcurve with equally spaced bins. The underlying principle is the assumption that the majority of time, the telescope will look at empty regions of the sky. Since most bright sources of the RASS catalog are concentrated in the galactic plane, this is a reasonable assumption. The majority of bins in the lightcurve will therefore contain only background radiation. The count rate of these blocks and thus the background rate is calculated by creating a histogram of the values of all lightcurve bins. This histogram holds information about the occurrences of

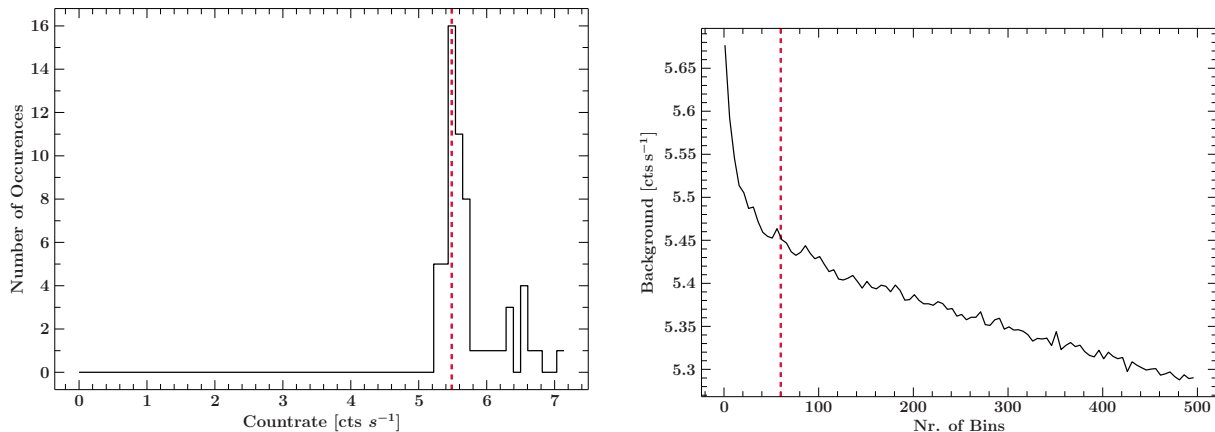


Figure 5.5: *Left*: A histogram of the distribution of count rates in the bins of an equally spaced lightcurve for a day length chunk of an all-sky survey. The determined background count rate is the count rate with the highest frequency, marked with a dashed red line. *Right*: The background count rate as a function of the number of bins in the lightcurve. Long bins increase the probability that a source is seen in this bin, short bins do not provide a sufficient statistic. The red line marks 60 bins, the value chosen throughout this thesis.

different count rates. The background radiation is then the maximum of the histogram, i.e. the count rate with the highest frequency. Such a histogram is shown for a day length chunk of data in Fig. 5.5 of the left.

The background rate determined by this approach is of course a function of the chosen bin width of the lightcurve. If the bins are chosen too long, the chance of averaging over background and a source rises. If it is chosen too short, the statistics are not good enough to produce reliable results. Fig. 5.5 on the right shows the determined background rate as a function of the number of bins in the lightcurve. A small number of bins in the lightcurve of course results in longer bins. The count rate is high for long bins, since they are likely to contain source counts and decreases with increasing number of bins. The curve shows a change of slope around 60 bins, where it changes into a linear decay. I assumed that the linear function of the curve after 60 bins indicates a homogeneous observation, therefore only background is seen. I therefore chose the value of 60 bins for the background determination, however a unique value is hard to be found.

## Results and discussion

Tab. 5.1 lists the background rates for an observation without any sources and two all-sky surveys, one with transient sources only, the other additionally includes the RASS sources. The count rates are calculated for each day-length chunk of the survey separately and then averaged over all 185 blocks of an half-year survey. The given errors indicate the fluctuations of the background rate between the different chunks of data. The count rates are determined with each of the presented methods, which show good agreement. Since the method based on the equally spaced lightcurve has lower errors I chose this method for background determination throughout the thesis.

The count rate of the particle background, was determined by running a half year all-sky survey simulation without any sources. Therefore only particle background is detected. The count rate is obtained, by calculating the average count rate for each day length chunk of the survey and averaging these rates for all 185 days.

The transient only run shows a lower count rate than the particle background rate, although

Table 5.1: Background count rates of particle background only and different simulation settings for both determination methods. All values are determined in a day length chunk of data and then averaged over 185 chunks, which equals to half a year. All values contain background counts for all seven telescopes. Both approaches are in good agreement within their uncertainties. The lightcurve histogram approach however has lower errors. The highest contribution is the particle background however adding X-ray sources, like the RASS catalog, increases the overall background rate.

	Bayesian [ctss <sup>-1</sup> ]	Histogram [ctss <sup>-1</sup> ]
Particle Background	5.131 ± 0.006	–
Only GRBs	5.114 ± 0.274	5.101 ± 0.023
GRBs and RASS	5.679 ± 1.116	5.445 ± 0.106

additional X-ray sources are included. However, the values are equal within their uncertainties. The transient run background rate, however, shows higher statistical fluctuations than the particle background, which means a X-ray background contribution was detected, however it was too low, to rise above statistical fluctuations.

Although the particle background is equal for all observations, the background rates changes for different simulation settings, since the X-ray contribution to the background changes. The simulation including RASS sources therefore has a higher X-ray background than the run with transients only, since it includes far more sources contributing to the background.

This difference in background rates can be easily explained by looking at the included sources. The source densities in the two **SIMPUL** files differ: while the GRB file contained about  $4.8 \times 10^{-4}$  sources in the FOV, the RASS catalog provided on average 2.4 sources in the FOV. Most of these sources are too faint to be identified, therefore are not resolved in the lightcurve. In both presented methods, these counts are then assumed as diffuse X-ray background. Since there are permanently sources in the FOV during simulations with the RASS catalog, the background count rate is of course higher than in the transients only run. These effects can be seen in a  $\log N$ - $\log S$  plot. The  $y$ -axis gives the fractional amount of time during which the detector count rate is higher than the corresponding value on the  $x$ -axis. Fig 5.6 shows a  $\log N$ - $\log S$  plot for several representative day-length chunks of the all-sky surveys.

The red lines represent data from two chunks from the transients only run, the blue ones from the runs with the RASS catalog. The dotted lines indicates the background level for each simulation setup. As seen in the figure, the GRB+RASS run shows higher count rates almost the entire survey, which is in good agreement to the expectations. Note that in both simulation runs, only about 50% of the simulation time is brighter than the background, justifying the assumption earlier that most of the exposure time only background is observed.

Two out of the three chunks in the GRB only run are almost identical, while the remaining curve is significantly brighter. The reason is that the runaway curve contains a detected transient while the remaining two only observe background. Since the GRBs are homogeneously distributed, the emerging X-ray background is too. Therefore all chunks will look the same, except if a transient is detected. This fact is reflected in the much lower uncertainties of the background measurement of the GRB run in comparison to the GRB+RASS run. The latter, however, is not as homogeneously as the GRB run, which can be seen in the high uncertainties of the background and the fluctuations of the line of the different chunks.

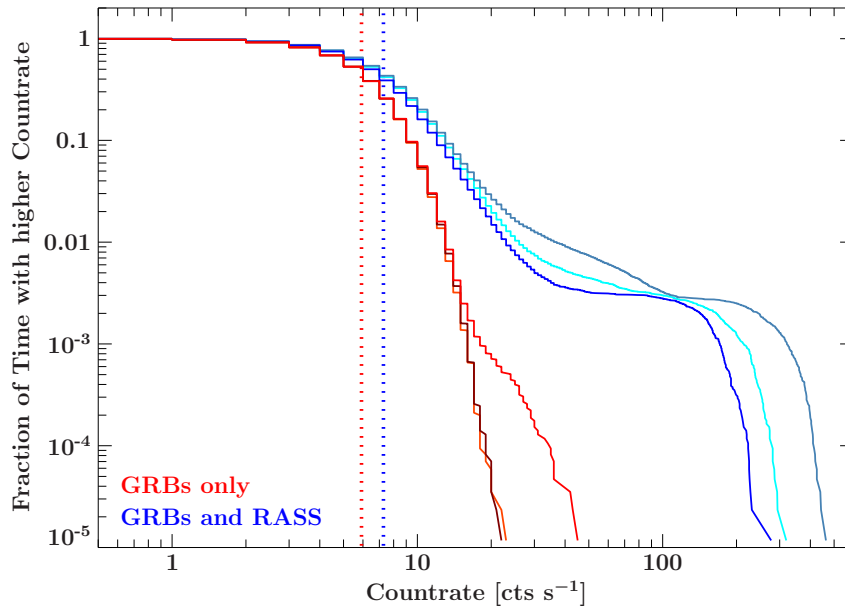


Figure 5.6: A  $\log N$ - $\log S$  plot for the all-sky surveys. The  $x$ -axis shows the count rate, on the  $y$ -axis the corresponding value is the fraction of time during which the count rate is higher than value on the  $x$ -axis. Each curve is generated from a one-day length chunk of the all-sky survey. The red curves are from simulation runs with only the transient source catalog included, the blue ones are from runs with transient sources as well as the transients. The dotted lines show the background rates for each simulation run. Both simulation runs are brighter than the background for about 40%

#### 5.2.4 Detection Limit

Having presented and discussed the single components of the source detection algorithm, the first application was to quantify its sensitivity. For this purpose I set up simulations of observations of a slew over a single source. No X-ray background, but the cosmic ray particle background was included. This setup is rather simple and concerning the source detection algorithm a very optimal situation, since no source overlap is possible. Vignetting effects still occur, but due to the known situation they can be accounted for. This analysis will therefore yield a lower flux limit in optimal conditions. Although these conditions will most probably never be met in a real all-sky survey, these simulations give a feeling of the abilities of this source detection approach.

As mentioned the simulation setup consisted of a single source and no X-ray background. The official *eROSITA* attitude file was used for the correct slew speed. The exposure time was set to 120 s., the simulation therefore starts looking at the empty sky, then the source enters the FOV and leaves it again. To investigate the influence of vignetting effects on the sensitivity, I ran all simulations for sources at different off-axis angles for  $0^\circ$  to  $0.5^\circ$ . To find the lower flux limit, I performed runs for 50 fluxes in the interval  $[7 \times 10^{-13}, 3 \times 10^{-10}]$   $\text{erg cm}^{-2} \text{s}^{-1}$ . Each combination of flux and off-axis angle were run at least 60 times.

On each output event list the source detection algorithm was applied: at first the bayesian blocks are detected. Since these short simulation runs do not provide sufficient statistics to obtain the background count rate, I used the background count rate caused by cosmic ray particles determined in Sec. 5.2.3 in Tab. 5.1. With this count rate the SNR of each block is calculated. The source in a simulation run is assumed to be detected, if the lightcurve has at least one block with  $\text{SNR} \geq 5$ . Since the source detection process is suspected to statistical fluctuations, a source with a flux close to the detection limit can be detected in one simulation

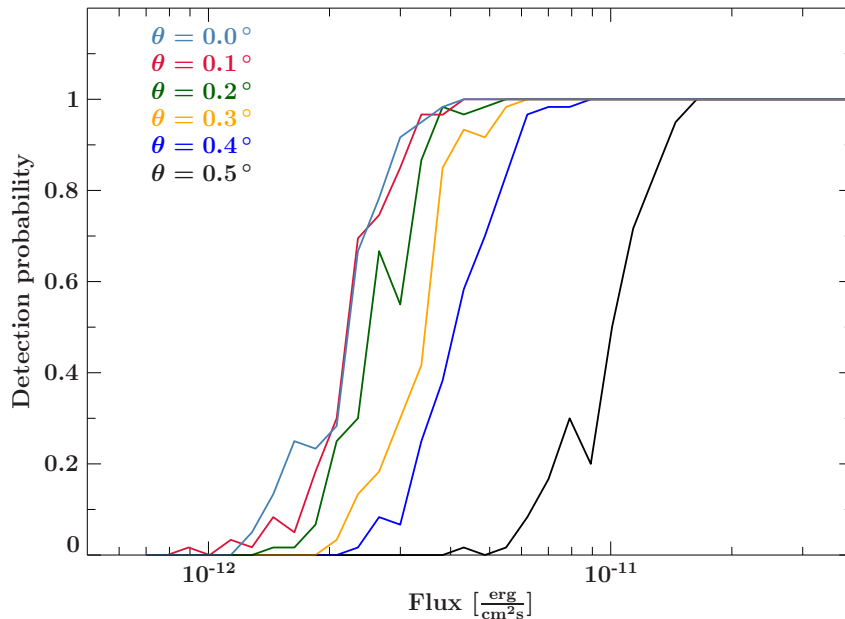


Figure 5.7: Probability to detect a source at a given off-axis angle as function of the flux. For the optimal case of an on-axis observation, the detection limit is at a flux of  $4 \times 10^{-12} \text{ erg cm}^{-2} \text{ s}^{-1}$ . For higher off-axis angle this decreases to  $1.7 \times 10^{-11} \text{ erg cm}^{-2} \text{ s}^{-1}$ . A rapid decrease of the detection probability is observed, sources with fluxes below  $2 \times 10^{-12}$  are unlikely to be detected.

run but may not be in another run with identical setup. I therefore calculated a detection probability for each combination of flux and off-axis angle by dividing the number of runs in which a source was detected by the total number of runs. The results are shown in Fig. 5.7.

Sources with fluxes below  $1 \times 10^{-12} \text{ erg cm}^{-2} \text{ s}^{-1}$  can not be resolved at all. Beginning with  $3 \times 10^{-12} \text{ erg cm}^{-2} \text{ s}^{-1}$ , which corresponds roughly to a combined count rate of about 7–8  $\text{cts s}^{-1}$  in all telescopes with an absorbed power law (see Fig. 4.6), there is a high probability to detect sources for on axis observations. Off-axis observations at high angles  $\theta = 0.4^\circ$  can be made with fluxes above  $6 \times 10^{-12} \text{ erg cm}^{-2} \text{ s}^{-1}$ . All curves show a very steep incline above the flux limit. If a source can be detected or not is dependent of the bayesian block algorithm finding the correct change points or not. Therefore the minimum count rate of 7–8  $\text{cts s}^{-1}$  at a background of 5.28  $\text{cts s}^{-1}$  is needed to trigger a change point.

If a slew time of 41 s and a background count rate of 5.13  $\text{cts s}^{-1}$  are assumed, the count rate needed to reach  $\text{SNR} = 5$  is 2.82  $\text{cts s}^{-1}$ . Therefore the sensitivity of finding change points is the limiting factor in the detection process. Hence a higher sensitivity may be achieved by lowering the `nbp_prior` parameter in the bayesian block algorithm. However, due to lack of time, I was not able to test this.

Note that the lower flux limit of  $3 \times 10^{-12} \text{ erg cm}^{-2} \text{ s}^{-1}$  is only valid at optimal circumstances, in most cases a higher background and several sources in the FOV at the same time are expected. Therefore sources close to the limit may not be detected in the all-sky survey. However, even at perfect conditions, sources below the limit will not be detected by this method.

Given the flux limit, about 1000 sources in the RASS catalog are bright enough to be resolved by the presented detection process. Since all transients are brighter than the flux limit at the beginning, the detection of transients is limited by the low probability to have a GRB afterglow in the FOV while it is bright enough.

Note that the given flux limit only refers to the presented detection algorithm based on the bayesian block analysis of the lightcurve. Other detection approaches may reach higher sensi-

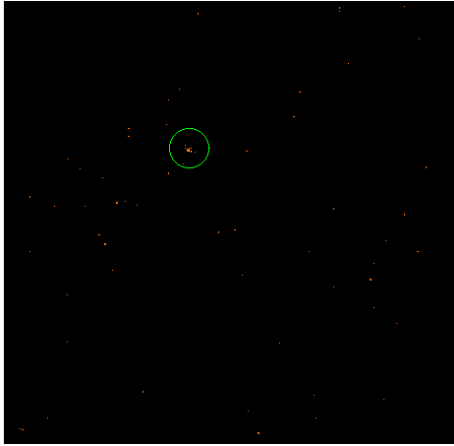


Figure 5.8: A source with a flux of  $8.92 \times 10^{-13} \text{ erg cm}^{-2} \text{ s}^{-1}$  in 0.5–10 keV. It is too faint to be detected by the bayesian block algorithm, however, a cluster of bright pixels is visible. Image based detection algorithm may detect this source.

tivities. A main disadvantage of the lightcurve based detection is that background counts from the entire detector are measured. Image based approaches can extract events from the source region, therefore reducing the background, which increases the SNR. Figure 5.8 for example shows an image of a faint source with flux of  $8.92 \times 10^{-13} \text{ erg cm}^{-2} \text{ s}^{-1}$  in 0.5–10 keV. No change point is detected in the corresponding detector lightcurve, however, a cluster of bright pixel is visible in the image, which may be detected with a appropriate detection algorithm.

However, this is only a outlook, I will not go into further detail.

### 5.3 Detection of transient sources in all-sky survey

To adapt the developed detection approach to the all-sky survey data, I performed two simulations of all-sky surveys. The first one included only the transient source catalog. The data obtained from this simulation run were used, to test the source detection on all-sky surveys. In the second simulation run I added the RASS catalog. These data represent a realistic observation and were used to adapt and test the detection process to realistic situations.

In this section I will present how the detection algorithm is applied to the data of the all-sky surveys. Figures 5.10 and 5.13 show images of the sky as seen by *eROSITA* during the simulated all-sky surveys. These are two dimensional histograms: the events are binned to two dimensional pixels and then projected to a plane using the Aitoff projection. The color encodes the number of events in each pixel.

At the beginning of each section I will present the most important results from the simulations and what difficulties could result for the source detection. Based on these result I will discuss, how the basic source detection process is adapted and improved.

#### 5.3.1 Transients only

For a first proof of concept of the detection process, I set up an all-sky run with only transient sources and particle background, since due to the low source density and the lack of X-ray background, the faced conditions are close to optimal. This should enable an easy adaption of the detection process to the all-sky survey mode.

#### Simulation results

At first I will present the obtained data from the all-sky survey. The left panel of Fig. 5.9 on the left shows a typical lightcurve (black) and the bayesian blocks (red) of a day of data of the survey. The lightcurve is fluctuating around the background count rate, showing now

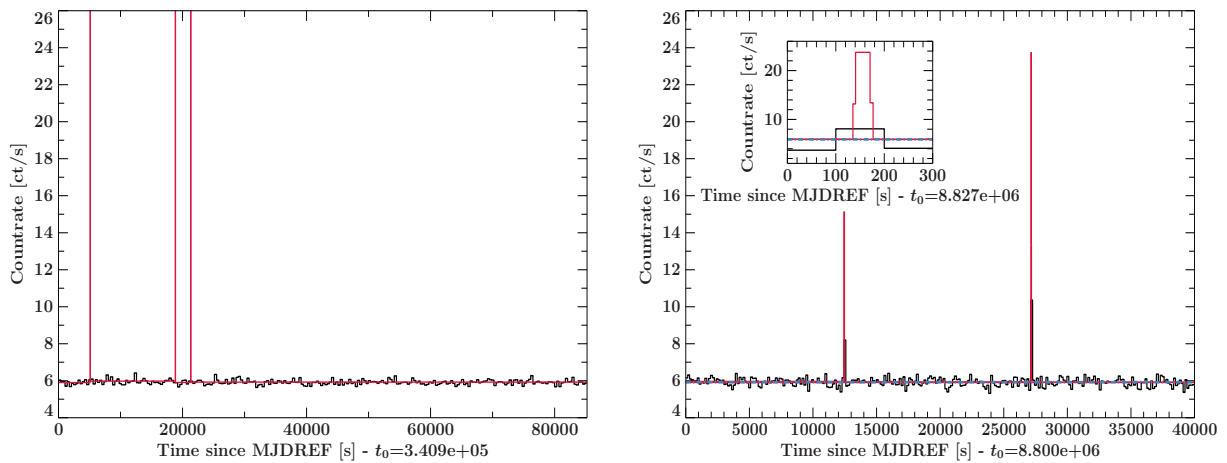


Figure 5.9: Equally spaced lightcurve (black) and bayesian block lightcurve (red) of a day length chunk from the all-sky survey with transients only. The blue line marks the background count rate. *Left*: bayesian block algorithm detected change points and blocks caused by background fluctuations, this feature is not visible in the traditional lightcurve *Right*: Lightcurve and bayesian blocks shows high peaks caused by a transient source. *Inset*: Enlargement of right peak. Optimal binning of bayesian blocks compared to regular lightcurve can be seen.

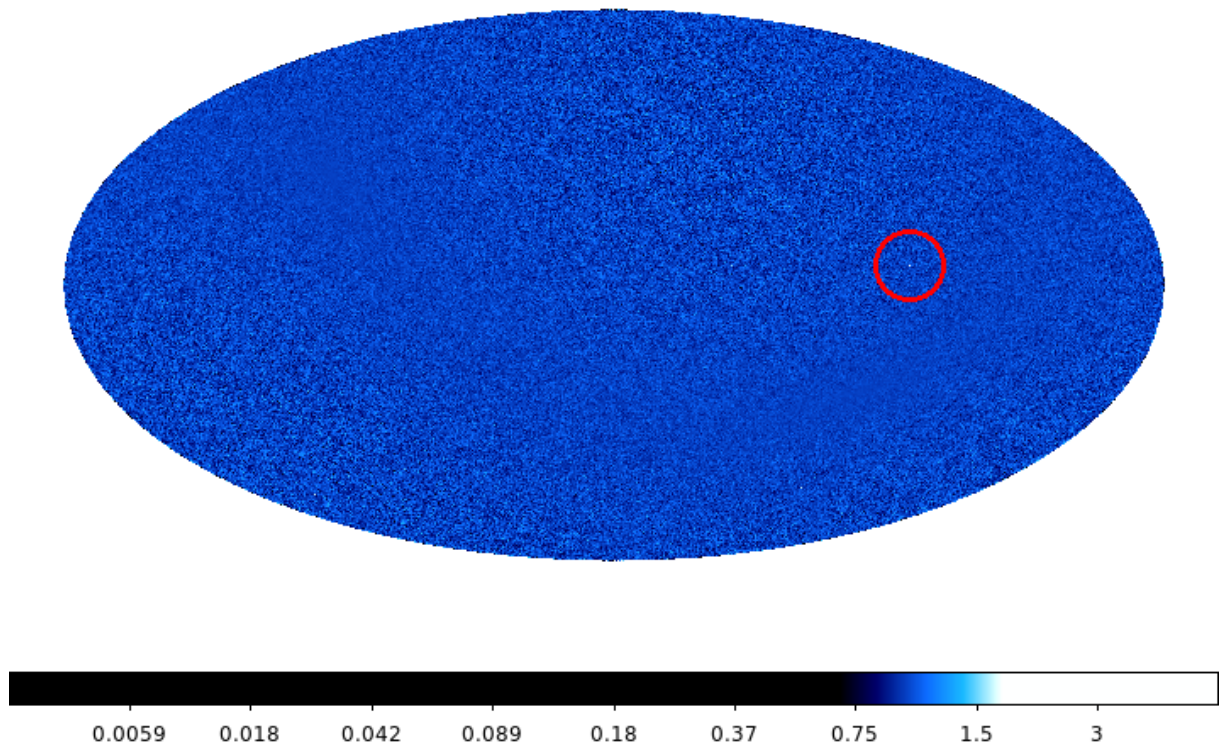


Figure 5.10: An Aitoff projection of the all-sky simulation with transient sources only. The image shows the entire sky as seen by *eROSITA*, the color codes the number of events at each pixel. Due to the exposure correction the absolute values of the counts are not valid any more. A single bright spot (marked with a red circle) is visible above a homogeneous background. This spot is the only transient source detected in this all-sky survey.

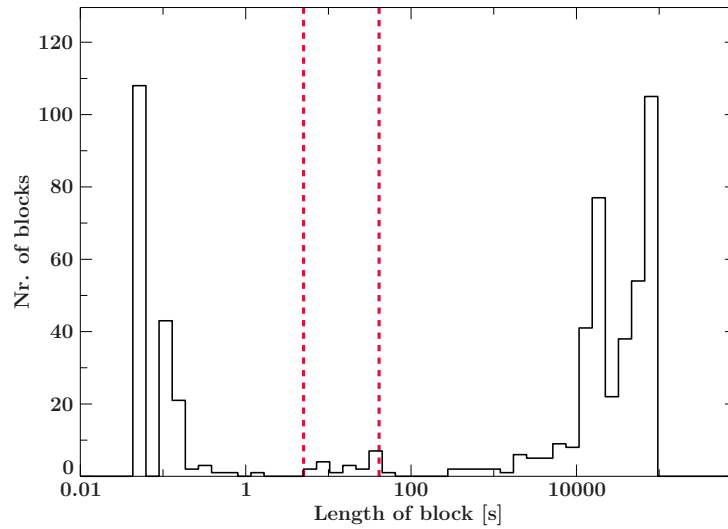


Figure 5.11: Histogram showing the distribution of block lengths in the bayesian block lightcurve. The gross of blocks are longer than the maximum slew time of 41 s therefore only background radiation. Blocks with a length shorter than 5 s are supposed background fluctuations and are omitted in the source detection. Therefore only the blocks between the dashed red lines may be detected sources

additional features. Only seven blocks are detected for the entire day. Three of them are high, narrow peaks, possibly triggered by sources, however, their length is below 1 s. Due to the short duration, the equally spaced lightcurve does not show this feature. Although theoretically a source can pass through the FOV in 1 s at very high off axis angles, further simulations showed that no relevant number of photons are measured in this time, especially not enough to trigger a change point. These blocks therefore can only be caused by background fluctuations. Experience showed that a lower limit of the length of blocks caused by sources is around 5 s.

The majority of the day however consists of the remaining, long blocks with count rates matching the background. In this particular run, 183 of 185 days in the all-sky survey showed the presented behavior, therefore measuring nothing but background. As a result, only a few but rather long blocks are found by the bayesian block analysis, as can be seen in Fig. 5.11. Most blocks are longer than 100s or shorter than 1 s, therefore they are caused by background fluctuations and contain only background counts. The two red lines mark the interval [5 s, 41 s], which is the interval that contains blocks which could have been caused by sources. The number of blocks in this interval is however very small, reflecting the fact that very few sources were seen in this survey. Considering the low source density in the transient catalog an expected result.

The lightcurve on the right in Fig. 5.9 shows an extract of the lightcurve and the bayesian blocks with two blocks caused by a detected transient source. Opposed to the spikes caused by background fluctuations, the peaks are visible in the lightcurve, too. The inset shows an enlargement of the right peak and visualizes the advantage of the bayesian block analysis over the traditional lightcurve. While the classical lightcurve averages the high count rate of the source with surrounding background, the bayesian block fits the bin width to the source, resulting in a higher block and higher SNR ratio. Additionally, the timing of the source entering and leaving the FOV is more precise determined by the bayesian blocks than the traditional Lightcurve.

A zoom in of a slew of another bright source is shown in Fig. 5.12. At these small time scales, features of a single slew caused by the vignetting function are visible. Since the vignetting function decreases with the off axis angle, sources observed at the edge of the FOV appear fainter. Moving towards the center of the FOV they get brighter. For bright sources, like the

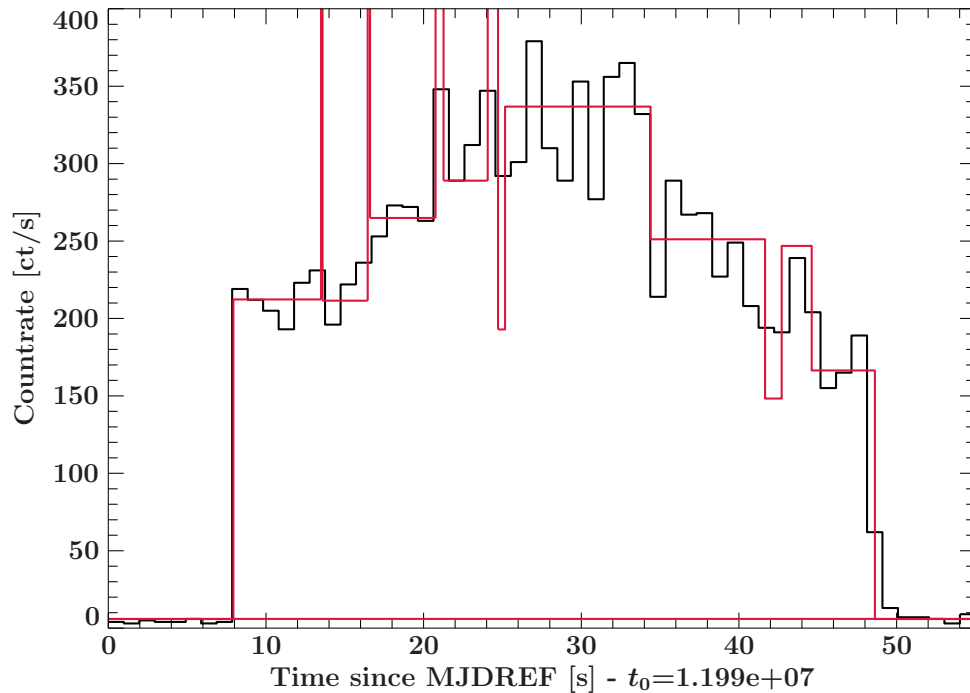


Figure 5.12: Vignetting effects on the bayesian block lightcurve of a slew over a single source. At the edges of the FOV less photons are detected than in the center. The count rate changes significantly as the source moves across the FOV, causing several change points and blocks

GRB afterglows, this effect can cause the bayesian block algorithm to trigger several change points. One source is then split into several blocks with increasing count rates. Additionally, the count rate is so high that the Poisson fluctuations are high enough, to cause very small but high spikes, as observed in the background radiation.

An important fact which can be seen on large time scales in Fig. 5.9 is the distance of the blocks. Due to the survey strategy, every spot on the sky will be visited six times with a distance of 4 h. The time between the two peaks in the lightcurve equals exactly this periodicity, the two peaks therefore are very likely to be caused by the same source revisited.

### Source Detection

The general process of source detection works as follows. At first the background count rate is determined, as described in Sec. 5.2.3. The next step is to perform the bayesian block analysis, which yields a list of blocks. From these blocks, all blocks with a  $\text{SNR} > 5$  are added to a list. This list contains all blocks which exhibit strong fluctuations in the count rate and are believed to contain real sources.

At this point, the vignetting effects have to be taken into account. A single source may have caused several blocks, of which every single one is thought of being caused by a different source. Although the vignetting effects are the strongest for bright sources, it can occur for every source. Additionally, I noticed that the very short but high pikes, as seen in Fig. 5.12, often are below the SNR threshold, although obviously containing source counts. The solution for these effects is to merge all blocks of a single source into one block, taking short blocks which failed to pass the SNR threshold into account.

The merging process iterates through the list of source candidates. If one of the following conditions is met for a block, the two, respectively three, blocks are merged.

1. The direct neighbor following the present block is also in the list
2. The block after the direct neighbor is in `relevant.blocks` and the intermediate block's length is shorter than 1 s

Then the merged block is regarded and iteratively checked again, if any transient condition is met. This process continues until none of the conditions is met or the total length of the merged block is larger than 41 s plus a margin of 9 s. This process only works if the source density is low enough that only one source at a time is expected to be in the FOV. The blocks as seen in Fig. 5.3 would have been merged, although they were caused by three different sources. With the low source density in this survey, however, these situations can be neglected

The properties of the merged blocks are adapted from the single block it consists of: the length and the photon count number is just the sum of the single blocks, the start time is the start time of the first block. All blocks in Fig. 5.12 will be merged into a single block. Since the merging equals to averaging over all single blocks, the exact shape of the source lightcurve is lost, however, this information is irrelevant for the detection process.

Merging the blocks yields a list of blocks, where each block represents one source. To account for the spikes caused by background fluctuations, all blocks with a length outside the interval  $[5\text{ s}, 50\text{ s}]$  are discarded, since a source can only cause block lengths inside the mentioned interval.

Finally, the remaining list of blocks is checked, if one source created multiple blocks, by the recurring observation of the source position. If the distance between two blocks is a multiple of 14400 s, but at most  $6 \cdot 14400\text{ s}$  since a source can only recur 6 times in the FOV, the second block is discarded.

These were all steps in the detection process. They sum up in the following list:

1. Determine background rate
2. Perform bayesian block analysis of the event data
3. Merge all blocks from the same source to account for vignetting effects
4. Discard all blocks with lengths above 50 s and below 5 s
5. Discard all blocks, which are caused by the same source

At the end of the process is a list of blocks, each representing one source. Each block however contains only the information, at which time the source was detected how long it lasted in the FOV. Therefore the sky coordinates of the sources have to be determined.

I found two possibilities to calculate the sky coordinates of the source in the block. The first is based on the sky projected coordinates of the detected photons. Neglecting background counts in the block, all events originate from the detected source. Therefore the source coordinates of the photons are the coordinates of the source plus a deviation caused by the PSF. Assuming the PSF is symmetric around the source center, the deviations can be averaged out by calculating the mean of the right ascension  $\alpha$  and the declination  $\delta$  of all photons which are detected in the time span of the block. These mean values are the coordinates of the detected source. The maximum uncertainties on the source position made by this approach lie in the order about  $0.3^\circ$ , in most cases however below.

This approach requires that only one source is contained in the block. If two or more sources are present, the average of the photon coordinates yields the average of the source coordinates of all sources.

The second approach is based on the attitude file. Since the temporal location of the block is known, the pointing of the telescope at the center of the block can be calculated from the

attitude file. These coordinates determine the point at which the source is at its most central position in the FOV during the slew. The length of the block yields the minimal off axis angle of the slew. The coordinate of the source can therefore be constrained to a circle line with the radius of the off axis angle around the calculated coordinates.

Comparing these two methods, the first approach should be preferred whenever possible, since it can locate sources more exactly than the attitude approach. However, if no sky projection or single event data are available, the second approach yields positions precise enough for, e.g., performing follow up observations.

The first simulations with 300 GRB afterglows showed that two transient sources could be detected with this method in half a year. This proves that the presented detection methods is suitable to detect transient sources and can be pursued further.

### 5.3.2 Transient sources with RASS catalog

After having a working source detection algorithm for a basic all-sky survey, I did now include the RASS catalog sources for a more realistic setup. I will proceed as in the previous section, at first point out the most important features of data obtained in the all-sky survey that would cause difficulties in the source detection, then present a solution to solve the encountered difficulties.

It is important to keep in mind that all RASS sources are modeled with no time variability. Although this model does not reflect the reality it is sufficient for our purposes.

#### Simulation results

The expectations of the RASS sources are that they create a constant diffusive X-ray background and about 1000 sources are bright enough to be resolved. Fig. 5.13 supports these expectations. The image shows a constant, diffuse background and many resolved point sources.

A long scale lightcurve of an extract of the survey is shown in Fig. 5.14 on the left, on the right a section has been magnified. The classic lightcurve still fluctuates around the background level, however, shows multiple bins rising above the background level. Most prominent is the number of bayesian blocks, which increased significantly, compared to the transients only survey. While there are some isolated blocks, many clusters of two or more adjacent blocks, as shown in Fig. 5.14 on the right, can be seen. As discussed in Sec. 5.1 the bayesian block analysis does not account for overlapping features on the lightcurve. Although change points are detected, the contributions of the sources to a block can not be separated. As a result a block represents several sources.

The presented detection algorithm can directly applied to the isolated blocks in the lightcurve, but will detect transients as well as constant sources from the RASS catalog. Since only transient sources are of interest here, those needs to be filtered from the RASS sources.

The clusters of blocks need to be treated separately. Since for our purpose only transients, are of interest the contributions of all permanent sources to a single block needs to be separated from the transient's contribution.

To sum up, two major issues are to be solved:

1. Split contribution of several sources to a single block
2. Filter transient sources from permanent sources.

#### Source detection

Since the general situation did not change compared to the transients only all-sky survey, the source detection did not change essentially to the one presented in Sec. 5.3.1. To account for

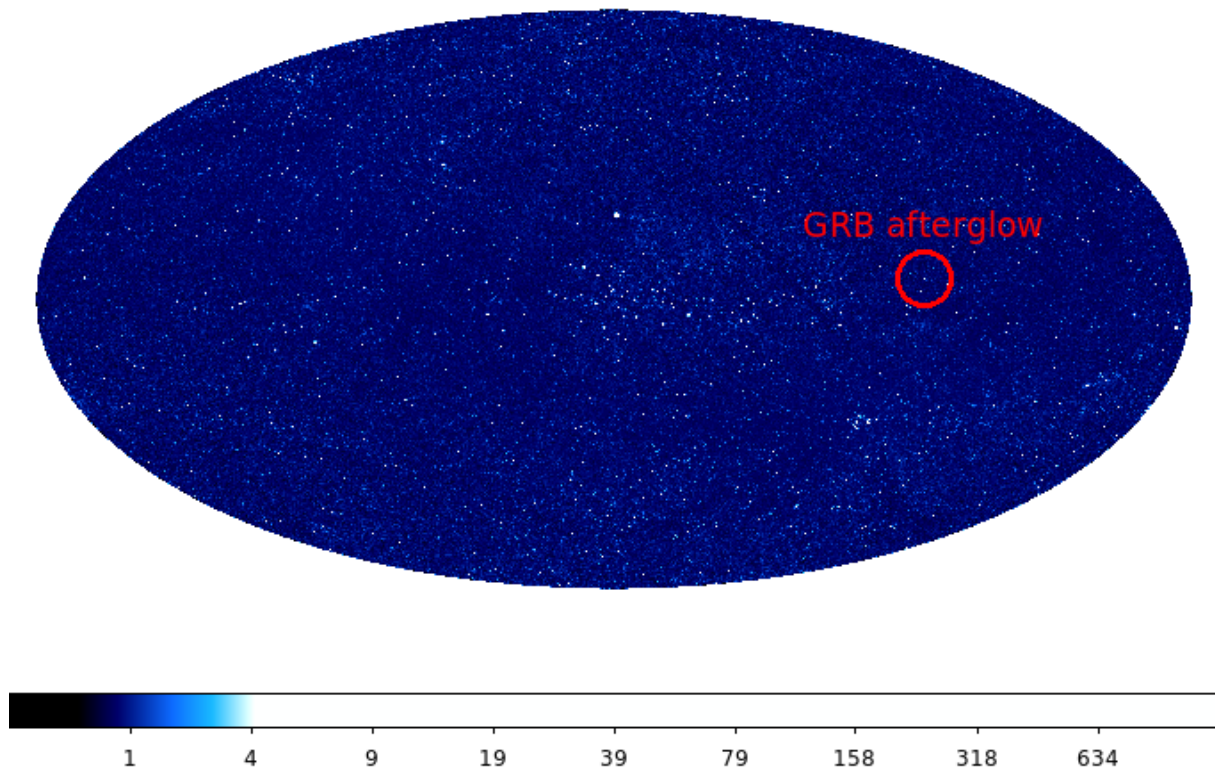


Figure 5.13: An Aitoff projection of the all-sky simulation with transient sources and the RASS catalog. The image shows the entire sky as seen by *eROSITA*, the color codes the number of events at each pixel. Due to the exposure correction, the absolute values of the counts are not correct. The scale was chosen for an optimal contrast. The image shows many resolved sources from the bright RASS catalog. However, most sources contribute to a rather diffusive background. The red circle marks the transient source the presented source detection algorithm was able to detect and filter beneath the RASS sources.

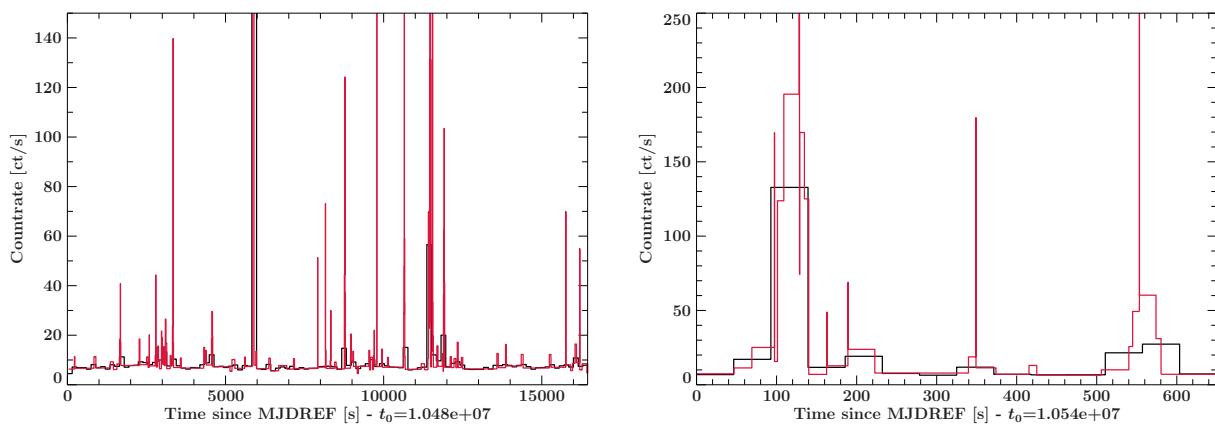


Figure 5.14: Extracts from lightcurves (black) and the bayesian block analysis (red) of a all-sky survey including transient sources and the RASS catalog

the aforementioned issues, however, an additional step is included in the detection process. Essentially, this step splits every block which contains sources into contributions from transient and known sources. The latter needs to be provided by a reference catalog. Then the SNR of the block is calculated again, however omitting all contributions from known sources. All blocks with  $\text{SNR} > 5$  therefore are caused only by transient sources. All blocks which SNR dropped below 5 represented permanent, known sources or only had faint contributions from transients.

This approach does not split contributions of two or more transient sources in one block, however I neglect this case. As seen in the simulations with only transient sources, the source density and detection rate is so low that the probability of two transients detected in block can be ignored.

After filtering all contributions from permanent sources, the situation is the same as in Sec. 5.3.1, which means, the described detection process can be applied on all blocks with SNR still above 5. The complete detection process then consists of the following steps:

1. Determine background rate
2. Run bayesian block analysis
3. Find all blocks with  $\text{SNR} > 5$
4. Find and discard contributions of permanent sources
5. Run SNR calculations again
6. Merge all blocks from the same source to account for vignetting effects
7. Discard all blocks with lengths above 50 s and below 5 s
8. Omit blocks, caused by the revisiting of a already detected source

A main ingredient to this approach is a complete list of all permanent X-ray sources in the sky. Such a catalog seems impossible to obtain, however, the sensitivity of the detection process puts a lower brightness value to sources which needs to be included. Since only sources above the detection limit of  $1 - 3 \times 10^{-12} \text{ erg cm}^{-2} \text{ s}^{-1}$  can be detected with our method, only those needs to be included. All of these sources were scanned in the RASS, therefore the 1RXS can be assumed as a *complete* catalog for our purpose.

A more general approach would be to run the source detection without step (4). The detection pipeline would therefore yield a list of all sources and their positions. This list can be used to perform a catalog match with all major catalogs, using for example VizieR<sup>2</sup>. These matches searches all known reference catalogs and returns a list of sources which were already detected by other observations. The detection algorithm is then run again including the filtering mechanism using the obtained reference catalog. A major advantage of the catalog matching approach is that it adapts to varying sensitivities and works for different wavelength, too.

The most important step in the pipeline is of course step (4). To achieve the desired task, I implemented two different approaches how to filter known sources.

### 5.3.3 Source filtering

I will now present in detail the two approaches to filter contributions from known sources. The first approach discards all photons which originate from known sources. This method requires

<sup>2</sup><http://vizier.cfa.harvard.edu/viz-bin/VizieR>

however the sky projected coordinates of the photons. Although obtaining these is no problem, the idea behind this detection method was to use as less information as possible.

Therefore I present a second approach, which works directly with the lightcurve and hence only needs the count rate. This filtering method tries to subtract all lightcurve features caused by permanent sources.

### Discarding photons from known sources

The general idea of this approach is to filter all photons in a block above  $\text{SNR} = 5$  which originate from permanent sources. For this step the sky projected coordinates of the photons are needed. They give the direction of the origin of the photons and therefore the position of the source they were emitted from. Each photon coordinate is matched with the reference source catalog, if a source is found at the given position, the photon is discarded. This way only background photons and photons from new, unknown sources remain in this block.

Since the sky projection (see Sec. 3.1.3) does not account for the random scattering of the PSF, the calculated sky coordinates of the photons are scattered around the source. A point like source therefore appears like an extended source with the shape determined by the PSF (see Fig. 3.8). Therefore all photons originating in a circle around the point source coordinates need to be discarded to account for the virtual PSF scattering. Utilizing a circle as cutting region causes systematic errors, since the PSF is asymmetric. However, more elaborate shapes would be more complicated, since the orientation needs to be taken into account. For a first proof of concept I therefore use circles.

Finding the correct radius for this circle is an important task. If a transient and permanent source are spatially close together, a radius too big may discard photons from the transient source, too. If the radius is chosen too small, too few photons are cut and the block does still exceed the SNR threshold. The optimum radius therefore cuts only as many photons as needed to decrease the SNR below the threshold of 5.

Figure 5.15 shows the image of sources as they appear in the sky seen by *eROSITA*. When in survey mode, the telescope will slew over source. This means, when the source first enters the FOV, the source is observed at the maximum off axis angle. With continuing slewing of the telescope, the source moves closer to the center up to a minimum off axis angle and then moves to the edge again and leaves the FOV.

Since the PSF is a function of the off axis angle, different PSFs are employed during the slew. As a result, the source changes its apparent shape during the slew. However, since all counts are integrated during the slew, the resulting image is a superposition of all PSFs used during the slew. The final image of the source is then called survey PSF.

Although these survey PSFs are asymmetric (see Fig. 5.15, especially for high off axis angles, I treated them as radial symmetric, since only this shape allows a simple definition of a source radius. Other shapes would require complex image subtraction methods. Implementing those would not satisfy the aim of this detection approach.

On the basis of the survey PSFs a source radius has to be determined. Since the PSF is a function of the off axis angle and the energy, and therefore the flux, the resulting source radius is a function of these quantities.

To find this radius, the radial distribution function of the photons around the source center needs to be calculated. This function  $f(r)dr$  gives the fractional amount of photons which are found in the interval  $[r, r + dr]$ , therefore is the normalized integral over the survey PSF. Hence, the survey PSF needs to be determined first.

For this purpose I ran a set of simulations of a single slew over a source. I sampled 60 fluxes between  $1 \times 10^{-7} \text{ erg cm}^{-2} \text{ s}^{-1}$  and  $1 \times 10^{-15} \text{ erg cm}^{-2} \text{ s}^{-1}$  in 0.5–10 keV to find the survey PSF as a function of the flux. Only on axis observations were performed. The asymmetric shape

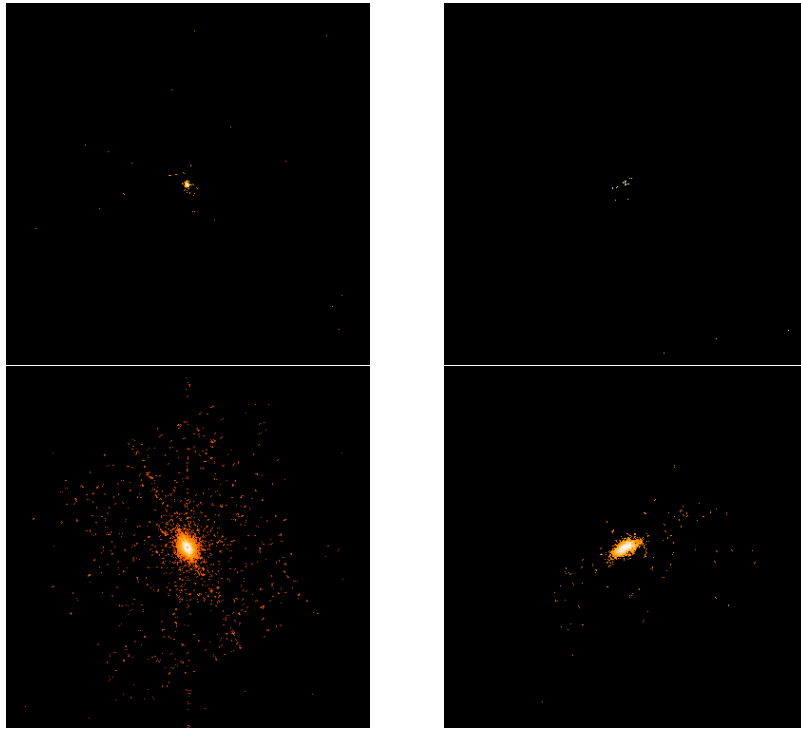


Figure 5.15: Image of a source in the sky as seen by *eROSITA* in survey mode. Sources with a flux of  $3.8 \times 10^{-11} \text{ erg cm}^{-2} \text{ s}^{-1}$  (top) and  $9.55 \times 10^{-9} \text{ erg cm}^{-2} \text{ s}^{-1}$  (bottom) in 2–10 keV, at off axis angles  $\theta = 0$  (left) and  $\theta = 0.5$  (right)

was averaged out by varying the slew direction. Therefore the source appears to be rotated for each slew and the average over all runs yields a radial symmetric source. For each flux value 20 different slew orientations with 50 runs each were simulated. The radial distribution for each flux was determined by calculating the distances between each detected photon and the position of the point source and creating a histogram of these distances. The normalized histogram is then the radial source distribution.

Figure 5.16 shows the radial distribution for different fluxes. With increasing brightness, the distribution gets more extended. Faint sources show a high peak close to the source center, however, for fluxes lower than  $2 \times 10^{-10} \text{ erg cm}^{-2} \text{ s}^{-1}$ , the distribution does not change significantly. Note, that bright sources show no counts very close to the source center due to pile up. The count rate is very high in this region, therefore the probability for invalid patterns due to pile up is very high.

With this set of distribution functions  $f(r)$ , a source radius  $R$  can now be determined. I chose the radius, which contains the amount of counts which needs to be discarded to decrease the block containing the source below 5. The source radius  $R$  after this definition is determined from

$$\text{SNR} = \frac{S \cdot \left(1 - \int_0^R f(r) dr\right)}{\sqrt{S \cdot \left(1 - \int_0^R f(r) dr\right) + 2B}} = 5 \quad (5.6)$$

Since all affected quantities like  $S$ ,  $B$ ,  $f(r)dr$  are subject to statistical fluctuations, the exact radius changes from block to block. However, applying eq. (5.6) at each block is complex, since the radial distribution function has to be determined first. Therefore an average source radius

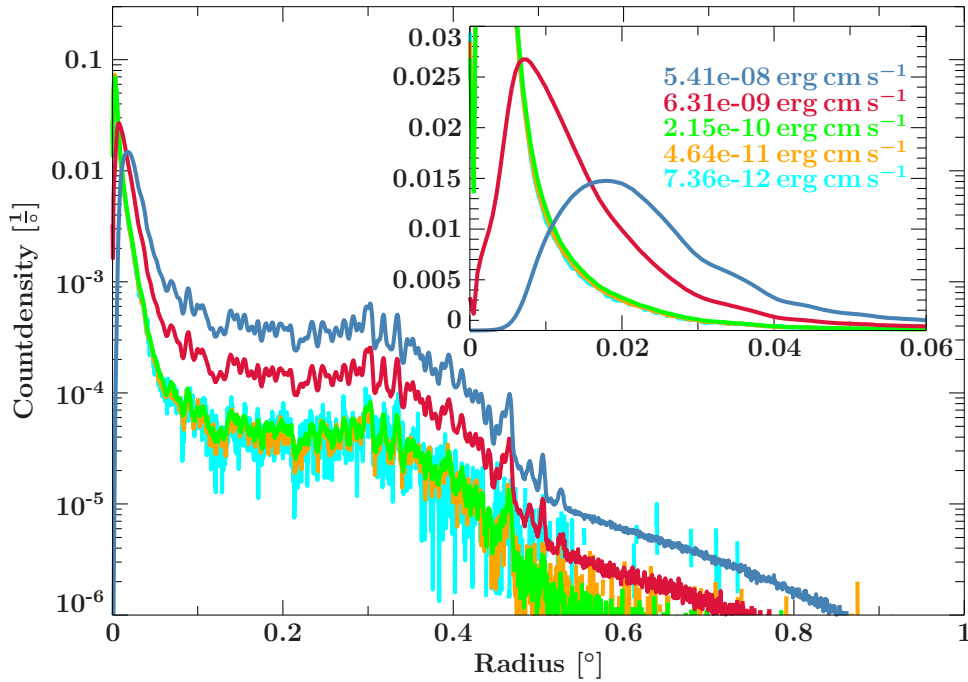


Figure 5.16: Radial distribution functions of photons virtually scattered around a source during sky projection due to the PSF for three fluxes. Brighter sources show broader distributions, since more high energetic photons are emitted. Due to pile up, the innermost regions of bright sources show a very low count rate, since most events are discarded as invalid. The fluctuations are due to numerical effects and deficient statistics

as a function of the flux was calculated. For this purpose I used the the background count rate from Tab. 5.1 and the average counts from Fig. 4.4. The resulting function is shown in Fig. 5.18.

Although  $R$  from eq. (5.6) is in theory the optimum choice, first tests showed that problems arise. As can be seen by comparing Fig. 5.16 and Fig. 5.18, the source radius changes significantly between  $7 \times 10^{-12} \text{ erg cm}^{-2} \text{ s}^{-1}$  and  $2 \times 10^{-10} \text{ erg cm}^{-2} \text{ s}^{-1}$  in 0.5–10 keV, while the radial distribution shows only a small change. Therefore the number of photons has the greatest impact on the source radius. Faint sources are detected with SNR only marginally above 5, as a result only a small fraction of photons need to be discarded. Therefore the statistical fluctuations of the count rates and discretization errors have strong impact on the source radius, which makes this not a reliable quantity in this flux regime below  $1 \times 10^{-10} \text{ erg cm}^{-2} \text{ s}^{-1}$ . First tests showed that the resulting radius is too small and not enough photons are discarded to pull the SNR of the block below 5, as can be seen in Fig. 5.17.

A more appropriate source radius definition is therefore needed for fluxes below  $1 \times 10^{-10} \text{ erg cm}^{-2} \text{ s}^{-1}$ . I employed a source radius which cuts 99% of all photons, therefore  $R$  is defined by

$$\int_0^R f(r) dr = 0.99 \quad (5.7)$$

This definition is less dependent on local factors than eq. (5.6) and as a result more robust. The function is shown in Fig. 5.18. The rather constant course of the curve reflects the minimal changes in the radial distributions better. However, tests showed that the radius is too small for higher fluxes.

As overall solution I defined the source radius from eq. (5.6) for fluxes smaller than  $1 \times 10^{-10} \text{ erg cm}^{-2} \text{ s}^{-1}$  and definition eq. (5.7) for fluxes above  $1 \times 10^{-10} \text{ erg cm}^{-2} \text{ s}^{-1}$ .

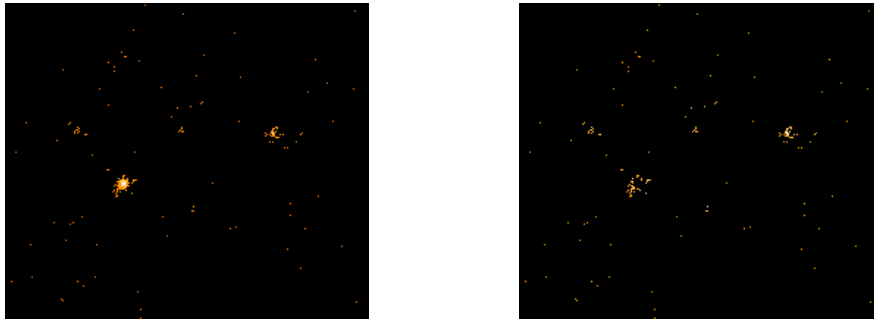


Figure 5.17: Two images of faint source in the sky as seen by *eROSITA*. Left picture shows unfiltered data with four sources, where as on the right all photons within the source radius after (5.6) are omitted. The chosen radius is too small to discard all photons, all sources are still visible in the filtered image.

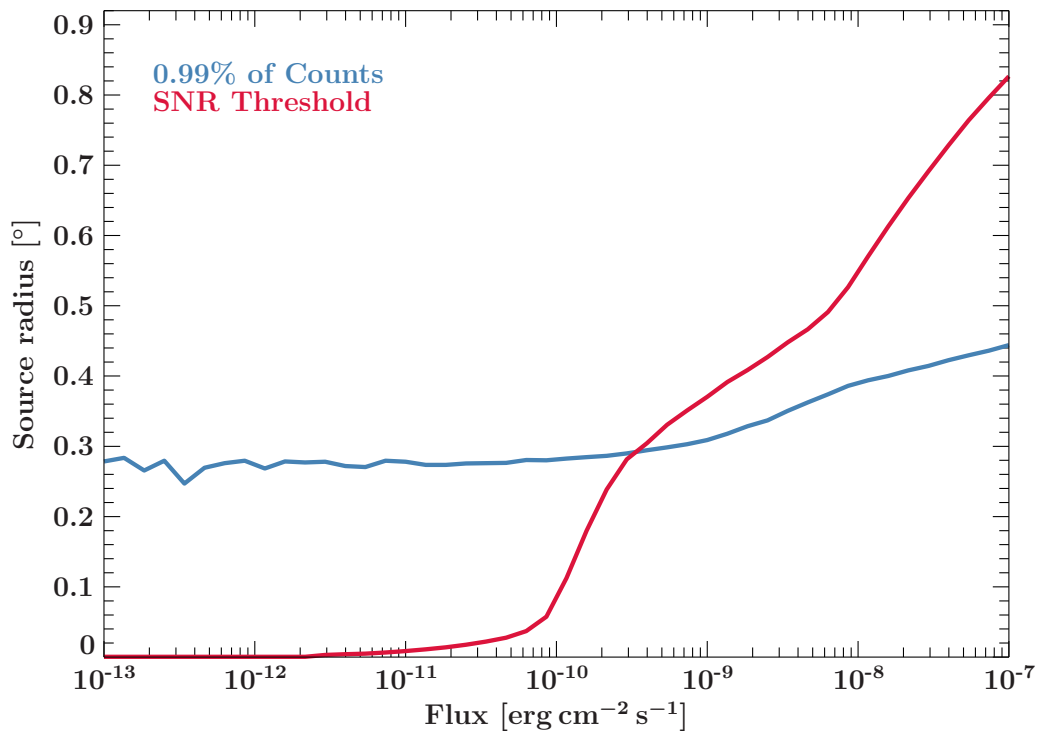


Figure 5.18: Two definitions of source radii. The red line shows the size of a circle, which needs to be cut out around a source, to discard the amount of photons needed to push the SNR of the block below 5. The blue line is the size of the circle to discard 99% of all counts emitted by the source



Figure 5.19: Image of the sky of a GRB afterglow and a faint permanent source. Left shows the original data, in the right picture all photons from permanent source are discarded

With a source radius defined, the filtering process works as follows. At first the pointing of the telescope is determined from the attitude file and the mid time of the relevant block. Then a list of all sources is generated from the reference catalog by selecting all sources within the radius of the FOV around the pointing of the telescope. A margin is added the FOV radius to account for the movement during the slew. Each of this source is then assigned a source radius according to its flux, for fluxes between the grid are interpolated. Then all photons which were detected within the time span of the block are extracted from the event file. Each photon is then checked, if its source coordinates is within a radius of any of the sources in the extracted list. If no such source is found, the photon is assigned to block.

At the end, each block is assigned a list of all photons which originate from regions in the sky, where no source is known to the reference catalog. An example is shown in Fig. 5.19. The left panel shows an image form all photons detected during the time span of the block, the right panel only shows photons passed the filtering process. The left source is a transient source not contained in the RASS catalog, whereas the faint source on the right is. After the filter process only the transient source remains, while the counts on the right were filtered.

Since only counts of a single source remain in the block, the source position of the source in this block can be found by just averaging the sky coordinates of all photons as described in Sec. 5.3.1.

This approach was created as a proof of concept, therefore many systematic errors were made for simplicity. The simplification with the greatest impact is probably that only radial distribution functions for on axis observation were used, although the off axis angles of all source can be determined. The source radius can therefore be determined more exactly, if different density distributions for different off axis angles would be employed.

### Template fitting

A disadvantage of the above mentioned filtering method is the need for the sky projected coordinates of the photons. If these are not available the method can not be applied. I therefore developed another approach which is independent of the coordinates of the photons. This method works only with the lightcurve, i.e., the count rate, properties of individual events are not required, although the attitude of the telescope is needed.

The idea behind this filtering approach is that each source leaves a feature in the lightcurve. An example of such a feature is shown in Fig. 5.12. Neglecting non-linear effects like pile up, the count rate of all sources just sum up, as a result, the detector lightcurve is just the sum of the contributions of all single sources. Given the reference catalog, the survey strategy and that the shape of the features on the lightcurve caused by the sources is known, the expected lightcurve

of the observation can be modeled. This lightcurve represents all contributions from known sources to the observation. Therefore subtracting this modeled lightcurve from the measured data leaves only contributions from transient sources. The SNR is recalculated based on the residual counts, if it is still above 5, a transient source is detected.

Although the bayesian blocks are not essential in this approach, I used them anyway as an indicator where sources were detected. Therefore the filter process can be restricted to relevant blocks, which saves computational time, since creating the predicted lightcurve of a whole day of data with hundreds of sources and fitting it to the measured one is an extremely costly task.

At first, the exact shape of source features on the lightcurve has to be determined. The quantities determining this shape are the off axis angle and the flux of the source. Since the slew time is a function of the off axis angle, the latter determines the width of the shape. The flux sets the height of the feature. Although the vignetting function has great impact on the shape, as seen in Fig. 5.12, it does not change for different observations and is therefore omitted as a parameter controlling the shape.

The aim is, to model these source features. Therefore creating a function, which takes the following parameters as input and returns the expected lightcurve. I will call this model source template in the further course. The parameters of this model are:

**Count Rate** The count rate sets the height of the template. The count rate is used instead of the flux, since it fits the units of a lightcurve better.

**Offaxis** The off axis parameter sets the width of the model

**centerPos** The centerPos parameter sets the position of the template on the time axis. It determines the time, at which the source is at the center of the FOV.

**Background** The background parameter adds a constant offset count rate to the template to model background radiation.

The complete lightcurve of an observation can be created from these models, by adding the templates of each source.

To create the source templates, I ran simulations of slews over a single source without any background radiation. To account for the statistical fluctuations, I slowed the slew speed by a factor of 500, this way the amount of detected photons is significantly increased and the observation yields better statistics while also avoiding pile up.

I ran several simulations for different off axis angles  $\theta$  in the interval  $[0^\circ, 0.51^\circ]$  with a step size of  $\Delta\theta = 0.01^\circ$ . Different fluxes were not varied, since these only scale the template by a simple factor.

The events from the simulations are binned to a lightcurve with a bin width of 1 s. I used these lightcurves to create an ISIS (Houck & Denicola, 2000; Houck et al., 2013) model for a source template using the mentioned parameters.

The model includes features for off axis angle interpolation and arbitrary binning, enabling model evaluation on arbitrary lightcurves. Fig. 5.20 shows the model for different off axis angles and count rates.

With this model, source templates can be easily obtained by just setting up the fit function in ISIS and evaluating the model on the desired lightcurve grid. The temporal position and off axis angle of the observed source can be calculated from the attitude data and the source position, the expected count rate is determined with the source flux and Fig. 4.6. The model is initialized with the calculated values then a fit to the measured data is performed. Fig. 5.21 shows an example of a template fitted to data. The figure shows the measured count rates (blue

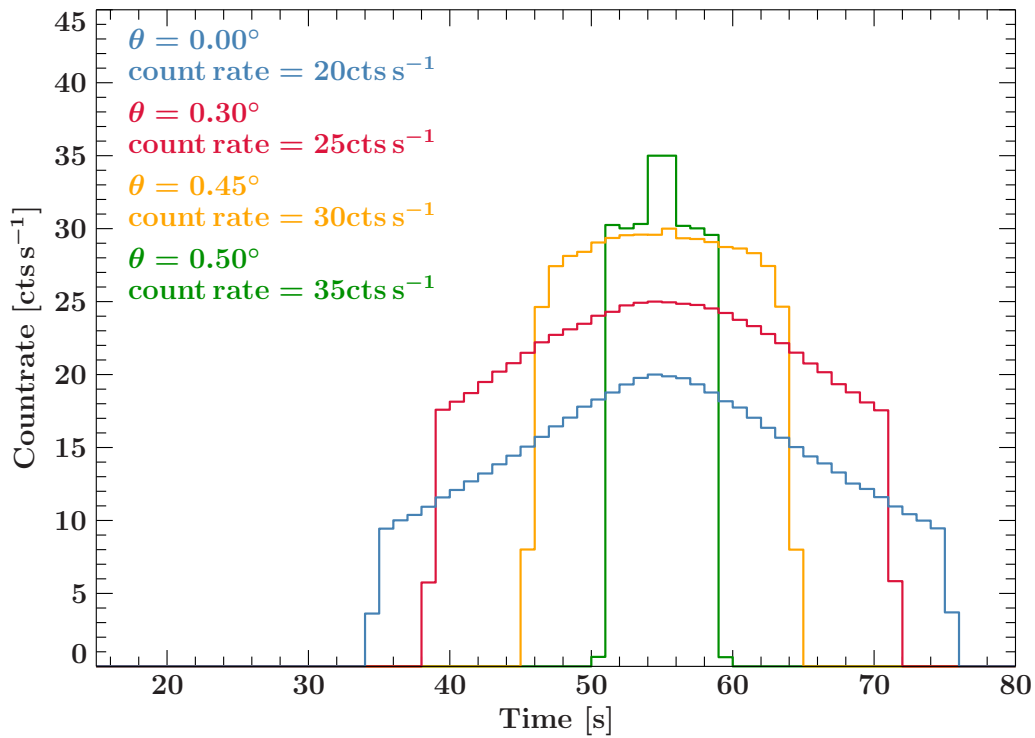


Figure 5.20: The source template model for different parameters, all evaluated on a grid with bin width of 1 s. It is interpolated from lightcurve samples of simulated slews over a single source at different off axis angles. Automatic rebinning and interpolation between off axis angles is performed.

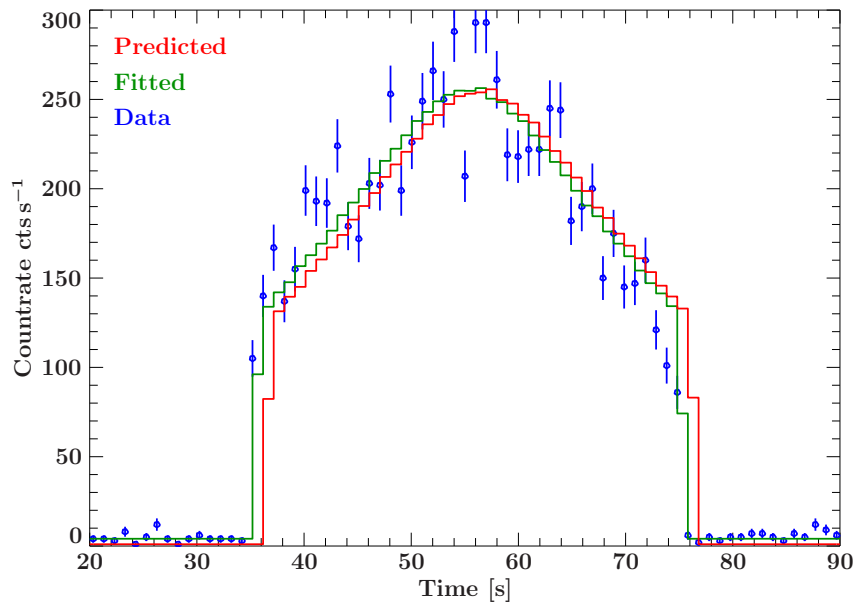


Figure 5.21: Measured count rates during a slew over a source (blue points), the predicted lightcurve calculated from survey and source parameters (red) and the fitted source template (green). The calculated model already shows good agreement with the data. The fitted model only differs slightly from the theoretical prediction.

points), the template with calculated parameters (red curve) and the final fit (green curve). The calculated parameters yield a good agreement of the model with the data.

The filtering process in a block from the all-sky survey works as follows: At first, all events in the time span of the block plus a margin of 10s in front and after the block is extracted. Then, the predicted lightcurve is modeled: at first a list of sources visible in the FOV during the time span of the block is extracted from the reference catalog. An ISIS model is created, consisting of the sum of as many source template models as sources in the block were found in the reference catalog. The model parameters are each set to the calculated values of the off axis angle, temporal position on the lightcurve and the count rate. Evaluating this model yields the predicted lightcurve for the present block.

Now the predicted lightcurve is fitted to the extracted data. Since the temporal position and off axis angle can be determined exactly, those parameters are kept constant during the fit. The count rate is kept variable to account for fluctuations and conversion uncertainties, but upper and lower limits for these values are defined for the following reason. Since the source density of the RASS catalog is very high, each detected block contains multiple sources. It is therefore very likely that a faint RASS source is found close to a transient source. If the count rate of this faint RASS source can take arbitrary value, the fit algorithm will assign the RASS source the count rate of the transient source, which means the contribution of the RASS source will be discarded. The flux limits prevents this error.

The plots at the top in Fig. 5.22 shows two lightcurve examples. The green lines indicate the start and end of the block, the black points are the measured data and the red line shows the fitted lightcurve. The left plot shows a block caused only by a RASS sources, whereas the right block was caused by a transient. The left plot shows good agreement to the data, after subtraction, very few counts remain, as can be seen in the plot below. The model in the right plot underestimates the count rate significantly, the subtraction leaves many counts. Note that the subtracted lightcurves are only shown for visualization, they are not used by the detection process!

Since the fitted lightcurve represent the contribution to the block from all known sources, all counts contained in this lightcurve are assumed to originate from known sources. The difference of the total number of counts measured and the number of counts in the model yields therefore the number of transient source counts.

With these residual counts, the SNR of the block is recalculated. If it is still above 5, the block is assumed as caused by a transient source and stored for further processing in the pipeline described in Sec.5.3.2.

The last step is to find the coordinates of the detected source. Since this approach should work with count rates only, the source position is calculated by employing the second source position approach using the attitude and temporal information of the block.

#### 5.3.4 Results and GRB detection rate

To test the the presented detection algorithm and filtering methods, I created two transients source catalogs with 400 GRB afterglows each. A half year survey of each catalog was performed with and without RASS sources, resulting in a total number of 4 runs.

I used the transients only runs, to test if the filtering methods spuriously discarded transients sources. At first I applied the detection process described in Sec. 5.3.1 on the transients only runs.

The filtering method described in Sec. 5.3.3 (discarding known photons) was applied to the entire data set. Due to lack of time, the filtering method described in Sec. 5.3.3 (template fitting) was only applied on the strips of data, known to contain a GRB from the transient only run. The results are listed in Tab. 5.2.

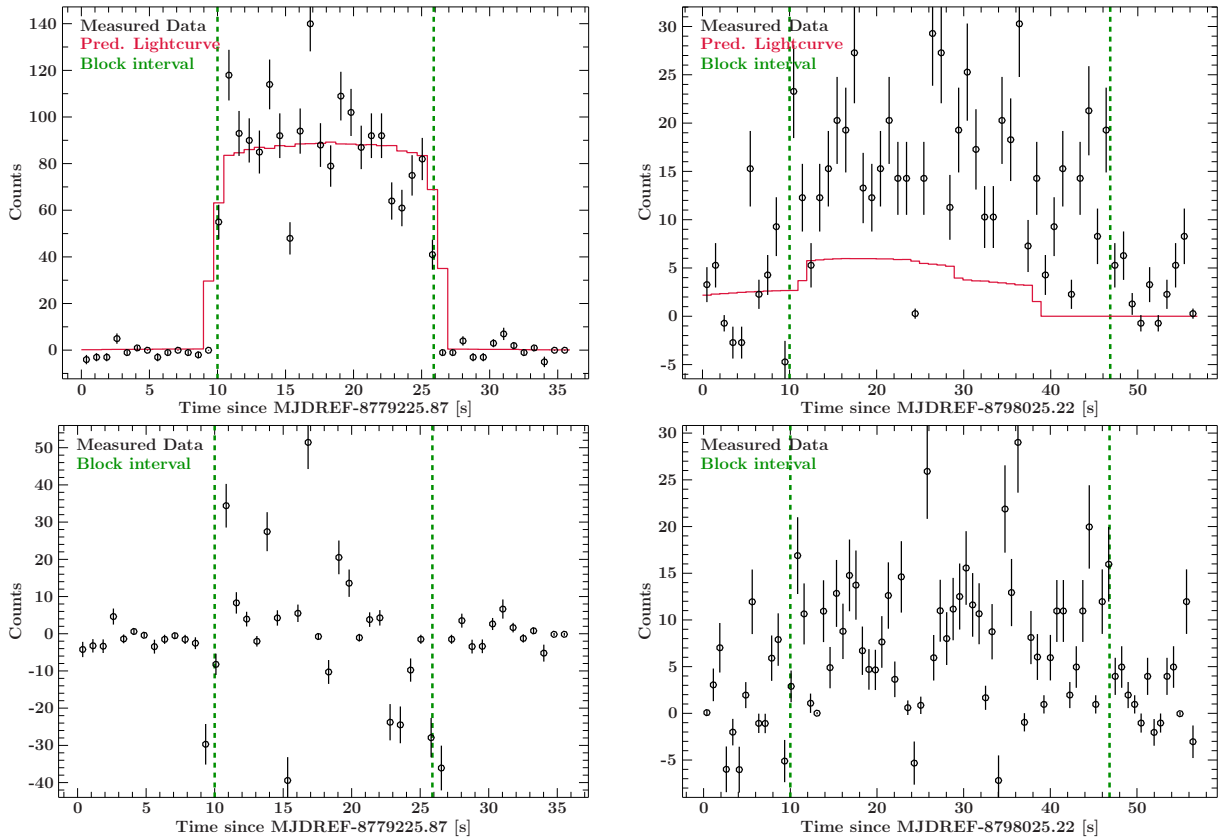


Figure 5.22: Extracts of measured lightcurves during the all-sky survey (black points). The green, dashed lines indicates the start and end of the bayesian block containing a source. The modeled and fitted lightcurve is drawn as red line. Top left plot only contains known sources, the measured data is therefore described in good agreement by the model. The block in the figure top right is triggered by a transient source, the model underestimates the lightcurve. Bottom figures: Data after subtracting the lightcurve model. The RASS source shows only few counts left, the transient source lightcurve shows no visible change.

Table 5.2: Number of detected GRB afterglows in two sets of all-sky surveys. The filtering methods work and detects all GRBs among the RASS background sources.

Simulation run	Nr. of detected Transients	
	GRBs only	GRBs + RASS
1	2	2
2	1	1

As can be seen, the filtering methods work well and are able to detect all transient sources among the RASS background. A visual representation can be seen in Fig. 5.13. The image shows an Aitoff projection of the sky seen by *eROSITA* of simulation run 2. The red circle marks the detected GRB afterglow. Based on the presented detection algorithm and all-sky surveys a prediction of how many GRB afterglows *eROSITA* will detect can be made.

Former work by Khabibullin et al. (2012) carried out analytic estimates as well as Monte Carlo simulations on the detection rate of GRB afterglows with *eROSITA*. These authors based their calculations on a minimal afterglow flux of  $3 \times 10^{-13} \text{ erg cm}^{-2} \text{ s}^{-1}$  in order to be detected. The identification of an afterglow for untriggered detections needs a minimum of three consecutive scans to identify a power law based lightcurve typical for GRB afterglows. Triggered afterglows, therefore sources which are known to be GRB afterglows, do not require three scans, since no lightcurve analysis needs to be done. As a result, 4–8 GRB afterglows are expected to be detected by *eROSITA* in one year.

During this thesis, I ran three half year all-sky surveys. One of the surveys detected one GRB afterglow, one run revealed two afterglows, while the last did not detect any. On average, a detection rate of two GRB afterglows per year can be found.

My results therefore show lower rates than those found by Khabibullin et al. (2012). An explanation for the difference may lie in the different flux limit. While the detection algorithm I used is at maximum only sensitive down to  $3 \times 10^{-12} \text{ erg cm}^{-2} \text{ s}^{-1}$ , Khabibullin used a lower detection limit of  $3 \times 10^{-13} \text{ erg cm}^{-2} \text{ s}^{-1}$ . Hence, the afterglows in his approach are detectable longer, which can explain the higher detection rate.

A disadvantage of the lightcurve based source detection is that the background on the entire detector is measured. Image based detection algorithms only suffer background in the region around the source. As indicated briefly in Sec. 5.2.4 more sensitive detection algorithm seems possible, therefore a detection limit of  $3 \times 10^{-13} \text{ erg cm}^{-2} \text{ s}^{-1}$  as used by Khabibullin et al. (2012) seems realistic.



## Chapter 6

# Conclusion and Outlook

The aim of this thesis was to find a source detection algorithm to find transient sources during the four year survey phase of *eROSITA*. The pursued principle was, to detect sources using only the detector lightcurve and being independent from further housekeeping data.

A special focus was set on a lightweight and quick implementation to enable fast follow up observations of transients. *eROSITA*'s performance and perspective of detecting transient sources were investigated using simulated data.

The presented algorithm works on a specially binned lightcurve, created from the event data with the bayesian block algorithm. This algorithm finds an optimal segmentation, with optimal meaning that the lightcurve emphasize features caused by sources. Source are found by searching bins which count rate exceeds the background with a  $5\sigma$  certainty.

If provided by a reference catalog, the algorithm automatically filters all contributions of persistent sources. This way, only transient sources are detected. The filtering is achieved in two different ways. The first method checks for every detected event, if a persistent source from the reference catalog is found at the photons origin position. If such a source exists, the photon is omitted in the further detection process. Only transient sources are detected this way. The second method is based on subtracting all contributions from the detected lightcurve, which are caused by known, persistent sources. All excesses left on the lightcurve are therefore caused by transient sources.

To test the developed detection algorithm, simulations of half a year of *eROSITA*'S survey phase was simulated using the simulator *SIXTE*. A source catalog of  $\sim 400$  GRB afterglows, modeled using *Swift* lightcurves, were used as transient sources among the RASS catalog as background sources.

*eROSITA*'S performance during the survey employing the presented algorithm was investigated. The detection algorithm has a lower flux detection limit of  $3 \times 10^{-12} \text{ erg cm}^{-2} \text{ s}^{-1}$ , which resulted in an average GRB afterglow detection rate of  $2 \text{ year}^{-1}$ . Earlier work suggested a detection rate of  $4\text{--}8 \text{ year}^{-1}$  with a lower flux limit of  $3 \times 10^{-13} \text{ erg cm}^{-2} \text{ s}^{-1}$ .

Additionally, an analysis of *eROSITA*'s pile up behavior during survey and pointed observations was made. Critical amounts of pile up can be expected at source fluxes of 1.5 to 20 mCrab depending on the off axis angle.

In general, I could show that a source detection based on a bayesian block lightcurve works well. With the help of two filtering methods, transient sources could be filtered of a background of persistent source, however being a transient is not a requirement to be detected. Basically every unknown source will be detected and pass the filtering.

The detection rate roughly agrees with earlier work, although a bit lower than expected.

I expect the main contribution to this difference the minimal flux to be detected. While Khabibullin et al. (2012) assumed fluxes in the order of  $1 \times 10^{-13} \text{ erg cm}^{-2} \text{ s}^{-1}$ , I determined  $3 \times$

$10^{-12}$  erg cm $^{-2}$  s $^{-1}$  to be the minimal flux detectable. A possible improvement of the algorithm would be, to lower the minimal flux.

I see three possibilities to achieve this aim in future work:

- At present, only the counts of a single slew is used to detect the source feature on the lightcurve, although there are up to six consecutive slews with a known periodicity available. Furthermore, if the transient source is visible long enough, eight further slews are available with a half year periodicity. A possible way would be, to cut out all counts in a consecutive slew, which are located around a source detected in the first slew, and add them to the counts of the source. The framework developed in Sec. 5.3.3 can be used for this purpose. However, a source needs to be found first, for this idea to work. Therefore the detection limit is not lowered but rather the SNR improved and the spurious detection rate decreased.
- The second idea of improvement picks up the issue of the previous idea, that the detection limit is not lowered but the SNR increased. This can be fixed by finding an optimal value of the `nbp_prior` parameter controlling the sensitivity of the Bayesian Block algorithm. Although a lower value of `nbp_prior` lowers the SNR ratio, this problem could be made up with the aforementioned idea.
- Scargle et al. (2013) presented an addition to the Bayesian Block algorithm, where no piecewise constant model, but a piecewise linear or exponential model was fitted to the data. Since the exact shape of the features we want to find is known (Sec. 5.3.3), the Bayesian Block algorithm can be modified to fit a model comprising those source templates, which could lead to a better change points detection.

All these features could lead to a more sensitive detection, resulting in a increased detection rate, matching the results obtained by Khabibullin et al. (2012)

Since the presented transient filtering methods were implemented as a proof of concept, many systematic errors were made:

Discarding photons of known sources (Sec. 5.3.3):

- Only radial distribution functions for on axis observations were calculated. Determining those for off axis angles would improve the source extract radius.
- The asymmetry of the PSF was not taken into account. Perhaps an easy way to include this issue can be found.

Template fitting (Sec. 5.3.3):

- The effects of pile up on the shape of the source template was not taken into account, which could cause the fit of the constructed lightcurve to fail and spuriously detect a transient source. The effects of pile up and critical fluxes were well investigated in Sec. 4. Since the count rates of all persistent sources are known, the expected amount of pile up is predictable well. New source templates to account for pile up effects can therefore be prepared.

## References

- Aschenbach B., 1985, *Reports on Progress in Physics* 48, 579
- Barthelmy S.D., 2000, *Burst Alert Telescope (BAT) on the Swift MIDEX mission*
- Bradt H., 2004, *Astronomy Methods*, Cambridge University Press
- Brand T., Wilms J., Dauser T., et al., 2016, In: *Society of Photo-Optical Instrumentation Engineers (SPIE) Conference Series*, Vol. 9905., p. 99055F
- Burwitz V., Predehl P., Friedrich P., et al., 2014, In: *Space Telescopes and Instrumentation 2014: Ultraviolet to Gamma Ray*, Vol. 9144., p. 91441X
- Cavallo G., Rees M.J., 1978, *MNRAS* 183, 359
- Costa E., Frontera F., Heise J., et al., 1997, *Nat* 387, 783
- Fishman G.J., Meegan C.A., Parnell T.A., et al., 1985, *International Cosmic Ray Conference 3*
- Friedrich P., Bräuninger H., Budau B., et al., 2012, In: *Space Telescopes and Instrumentation 2012: Ultraviolet to Gamma Ray*, Vol. 8443., p. 84431S
- Friedrich P., Bräuninger H., Budau B., et al., 2008, In: *Space Telescopes and Instrumentation 2008: Ultraviolet to Gamma Ray*, Vol. 7011., p. 70112T
- Gehrels N., Chincarini G., Giommi P., et al., 2004, *ApJ* 611, 1005
- Gehrels N., Ramirez-Ruiz E., Fox D.B., 2009, *ARA&A* 47, 567
- George I.M., Arnaud K.A., Pence B., et al., 2007, *The Calibration Requirements for Spectral Analysis*, Technical report, NASA/GSFC
- Giacconi R., Gursky H., Paolini F.R., Rossi B.B., 1962, *Phys. Rev. Lett.* 9, 439
- Gould H., Tobochnik J., Christian W., 2006, *An introduction to computer simulation methods: Applications to Physical Systems*, Addison-Wesley, 3 edition
- Gregory P., 2005, *Bayesian Logical Data Analysis for the Physical Sciences: A Comparative Approach with Mathematica® Support*, Cambridge University Press
- Hanisch R.J., Farris A., Greisen E.W., et al., 2001 376, 359
- Horack J.M., 1993, *Ph.D. thesis*, Alabama Univ., Huntsville, AL.
- Houck J.C., Davis J.E., Huenemoerder D., et al., 2013, *ISIS: Interactive Spectral Interpretation System for High Resolution X-Ray Spectroscopy*, Astrophysics Source Code Library
- Houck J.C., Denicola L.A., 2000, In: Manset N., Veillet C., Crabtree D. (eds.) *Astronomical Data Analysis Software and Systems IX*, Vol. 216. *Astronomical Society of the Pacific Conference Series*, p. 591
- Khabibullin I., Sazonov S., Sunyaev R., 2012, *MNRAS* 426, 1819
- Klebesadel R.W., Strong I.B., Olson R.A., 1973, *Astrophys. J., Lett.* 182, L85
- Klein R.W., Roberts S.D., 1984, *SIMULATION* 43, 193
- Longair M., 2011, *High Energy Astrophysics*, Cambridge University Press
- Margutti R., Zaninoni E., Bernardini M.G., et al., 2013, *MNRAS* 428, 729
- Meegan C.A., Fishman G.J., Wilson R.B., et al., 1992, *Nat* 355, 143
- Meidinger N., Andritschke R., Aschauer F., et al., 2013, In: *UV, X-Ray, and Gamma-Ray Space Instrumentation for Astronomy XVIII*, Vol. 8859., p. 88590B
- Meidinger N., Andritschke R., Ebermayer S., et al., 2009, In: *UV, X-Ray, and Gamma-Ray Space Instrumentation for Astronomy XVI*, Vol. 7435., p. 743502
- Meidinger N., Andritschke R., Elbs J., et al., 2011, In: *Society of Photo-Optical Instrumentation Engineers (SPIE) Conference Series*, Vol. 8145., p. 814502
- Meidinger N., Andritschke R., Hälker O., et al., 2007, In: *UV, X-Ray, and Gamma-Ray Space Instrumentation for Astronomy XV*, Vol. 6686., p. 66860H
- Merloni A., Predehl P., Becker W., et al., 2012, *ArXiv e-prints*
- Mészáros P., 1995, In: Böhringer H., Morfill G.E., Trümper J.E. (eds.) *Seventeenth Texas Symposium on Relativistic Astrophysics and Cosmology*, Vol. 759. *Annals of the New York Academy of Sciences*, p. 440
- Meszáros P., Laguna P., Rees M.J., 1993, *ApJ* 415, 181
- Okabe A., Boots B., Sugihara K., Chiu S., 2009, *Spatial Tesselations: Concepts and Applications of Voronoi Diagrams*, Wiley Series in Probability and Statistics, Wiley
- Pavlinisky M., Sunyaev R., Churazov E., et al., 2008, In: *Space Telescopes and Instrumentation 2008: Ultraviolet to Gamma Ray*, Vol. 7011., p. 70110H
- Pence W.D., Chiappetti L., Page C.G., et al., 2010 524, A42
- Percy J., 2007, *Understanding Variable Stars*, Cambridge University Press
- Piro L., 1997, In: Dermer C.D., Strickman M.S., Kurfess J.D. (eds.) *Proceedings of the Fourth Compton Symposium*, Vol. 410. *American Institute of Physics Conference Series*, p.1485
- Predehl P., 1999, In: Siegmund O.H., Flanagan

- K.A. (eds.) EUV, X-Ray, and Gamma-Ray Instrumentation for Astronomy X, Vol. 3765., p.172
- Predehl P., 2016, eROSITA – Status & Near Future, eROSITA.DE Consortium Meeting, Tübingen
- Predehl P., Andritschke R., Babyshkin V., et al., 2016, eROSITA on SRG
- Predehl P., Andritschke R., Böhringer H., et al., 2010, In: Space Telescopes and Instrumentation 2010: Ultraviolet to Gamma Ray, Vol. 7732., p. 77320U
- Predehl P., Andritschke R., Bornemann W., et al., 2007, In: UV, X-Ray, and Gamma-Ray Space Instrumentation for Astronomy XV, Vol. 6686., p. 668617
- Predehl P., Friedrich P., Hasinger G., et al., 2003, *Astronomische Nachrichten* 324, 128
- Predehl P., Hasinger G., Böhringer H., et al., 2006, In: Society of Photo-Optical Instrumentation Engineers (SPIE) Conference Series, Vol. 6266., p. 62660P
- Press W., et al., 2007, *Numerical Recipes 3rd Edition: The Art of Scientific Computing*, Cambridge University Press
- Read A.M., Ponman T.J., 2003, *A&A* 409, 395
- Scargle J.D., 1998, *ApJ* 504, 405
- Scargle J.D., Norris J.P., Jackson B., Chiang J., 2013, *ApJ* 764, 167
- Schmid C., 2012, Ph.D. thesis, Friedrich-Alexander-Universität Erlangen-Nürnberg
- Schmid C., Smith R., Wilms J., 2013, SIMPUT A File Format for SIMulation inPUT, Technical report, ECAP and SAO
- Schneider P., 2006, *Einführung in die Extragalaktische Astronomie und Kosmologie*, Springer
- Swift Science Center 2016
- Tenzer C., Warth G., Kendziorra E., Santangelo A., 2010, Geant4 simulation studies of the eROSITA detector background
- Trümper J., 1985, *ROSAT*, p. 243
- Trümper J., 1990, In: Gorenstein P., Zombeck M. (eds.) *IAU Colloq. 115: High Resolution X-ray Spectroscopy of Cosmic Plasmas.*, p.291
- Trümper J., Hasinger G., 2008, *The Universe in X-Rays*, Astronomy and Astrophysics Library, Springer Berlin Heidelberg
- Voges W., B. Aschenbach T.B., et al., 1999, *Astron. Astrophys.* 349, 389
- Wells A.A., Gehrels N.A., White N.E., et al., 2004, In: Hasinger G., Turner M.J.L. (eds.) *UV and Gamma-Ray Space Telescope Systems*, Vol. 5488. *procspie*, p.403
- Wolter H., 1952a, *Annalen der Physik* 445, 94
- Wolter H., 1952b, *Annalen der Physik* 445, 286
- Worpel H., Schwöpe A.D., 2015 578, A80

## Acknowledgments

First of all, I want to thank my supervisor, Jörn Wilms, for giving me the opportunity to write my thesis in this interesting field, for the possibilities to travel to workshops and conferences and for the never ending support and help for small and big problems.

Special thanks to Thomas Dauser, Thorsten Brand and Christoph Grossberger who introduced me to the world of **SLANG**, **ISIS** and **SIXTE** and never got tired to help with insightful discussions if I got stuck.

I would like to thank my office mates Ralf Ballhausen, Florian Erbesdobler, Margarita Behm and Thorsten Brand (again) for the good time full of candy, inspiring discussions and fun.

Next I would like to thank the system admins at the observatory, Thomas Dauser, Ingo Kreykenbohm and Fritz Schwarm who kept the computers and torque up and running.

A special thanks goes to Tabea Rettelbach and my friends and family for their moral support throughout the thesis.

Last but not least I want to thank everybody at the Observatory for the great time I had during working on my thesis.

## Eigenständigkeitserklärung

Hiermit erkläre ich, diese Arbeit selbständig angefertigt und keine anderen, als die angegebenen, zugelassenen Hilfsmittel verwendet zu haben.

---

Ort, Datum

---

Tobias M. Hain